Title

Manipulation of Nanoparticle Electron Transfer Dynamics by Engineering of Metal-Ligand Interaction

Author

Chen, Limei

Publication Date

2017

UNIVERSITY OF CALIFORNIA
SANTA CRUZ

MANIPULATION OF NANOPARTICLE ELECTRON TRANSFER DYNAMICS BY ENGINEERING OF METAL-LIGAND INTERACTION

A dissertation submitted in partial satisfaction
of the requirements for the degree of

DOCTOR OF PHILOSOPHY

in

CHEMISTRY

by

Limei Chen

June 2017

The Dissertation of Limei Chen
is approved:

Professor Shaowei Chen, Chair

Professor Jin Z Zhang

Professor Ilan Benjamin

Tyrus Miller
Vice Provost and Dean of Graduate Studies

TABLE OF CONTENTS

LIST OF FIGURES

Chapter 2

Chapter 3

Chapter 4

Chapter 5

Chapter 6

Chapter 7

Chapter 8

LIST OF TABLES

Chapter 4

Chapter 8

MANIPULATION OF NANOPARTICLE ELECTRON TRANSFER DYNAMICS BY ENGINEERING OF METAL-LIGAND INTERACTION

Limei Chen

ABSTRACT

Nanoparticles represent a novel class of material consisting of hundreds to a few thousand atoms each, and their physical and chemical properties are significantly different than the bulk materials. The electronic structure, chemical and optical properties of nanoparticles can be tuned by the size, shape, surface modification and interaction with supporting materials, to fulfil the potential specific applications in catalysis, imaging and electronic devices. In the preparation of nanoparticles, protecting ligands play a crucial role in the dispersion, size control, and shape control of particles. Here in this thesis, ligand functionalization of metal nanoparticles and engineering of carbon nanomaterials were manipulated, and the influence of metal-organic interaction on the chemical, optical and electrochemical properties of nanoparticles and their applications in fuel cell electrocatalysis were studied.

Ruthenium nanoparticles protected by ferrocenecarboxylates (RuFCA) were synthesized. The carboxylate group were bound onto the nanoparticle surface via Ru–O bonds in a bidentate configuration which is highly polarized, leading to the diminishment of the electron density of the iron centers and the increase of formal potential of the ferrocenyl moieties by 120mV in electrochemical measurements. In addition, galvanic exchange reactions of the RuFCA nanoparticles with Pd(II) followed

by hydrothermal treatment at 200 °C led to (partial) decarboxylation of the ligands such that the ferrocenyl moieties were now directly bonded to the metal surface, as manifested in voltammetric measurements that suggested intervalence charge transfer between the nanoparticle-bound ferrocene groups.

In a further study, decarboxylation was also found happened at the metal-ligand interface in the hydrothermal treatment of 2-naphthalenecarboxylate protected ruthenium nanoparticles at higher temperature 250°C, and the naphthalenyl moieties became directly bonded to the metal cores, which was confirmed by infrared and X-ray photoelectron spectroscopic measurements. In comparison with the as-produced RuCOONA nanoparticles, the decarboxylated nanoparticles (RuNA) exhibited markedly different optical and electronic properties due to electronic coupling between the particle-bound naphthalene groups. The intraparticle charge delocalization led to spilling of nanoparticle core electrons to naphthalene moieties, resulting in the negative shift of the formal potential.

In addition, the electron-transfer properties of the ruthenium nanoparticles protected by 1-dodecyne, laurate and 1-dodecanethiol were examined by scanning tunneling spectroscopic (STS) measurements. Ruthenium-vinylidene (Ru=C=CH–), –oxygen (Ru-O), and –thiolate (Ru-S) interfacial bonds were formed when protected by alkyne, carboxylate and thiol ligands, respectively, and the polarization of the interfacial bonds was found to increase in the order of Ru=C=CH– < Ru-S < Ru-O. The relatively large nanoparticles (dia. ~ 3 nm) were found to show clearly-defined Coulomb staircase; and with diminishing particle core dimensions to below 1 nm, Coulomb blockade started to emerge. The nanoparticle molecular capacitance and effective nanoparticle dielectric constants were estimated and the dielectric constants increased inversely with the nanoparticle core dimensions; and at any given particle size, the dielectric constants varied with the specific metal-ligand interfacial bonds, increasing in the order of Ru-S < Ru=C=CH– < Ru-O.

Part of the dissertation research was devoted to carbon nanomaterials. In one of the study, nitrogen-doped graphene quantum dots (NGQDs) were prepared by a facile hydrothermal method and incorporated with ruthenium metal ions by exploiting the unique complexation of selected nitrogen dopants with ruthenium ions. Complexation of NGQDs with ruthenium ions likely occurred through the pyridinic nitrogen dopants, leading to the incorporation of multiple metal centers within the conjugated graphitic C sp2 scaffolds (Ru-NGQDs). Intervalence charge transfer between embedded Ru ions was studied electrochemically, the Ru-NGQD compounds exhibited two pairs of voltammetric waves, with a peak spacing of 150 mV, suggesting Class II delocalized system. Near-infrared spectroscopic measurements demonstrated an absorption band emerged at ca. 1450 nm at mixed-valence metal charge transfer, by using $Ce(SO_4)_2$ as the oxidizing reagent.

Covalently crosslinking of GQDs were accomplished by forming ensembles of a few hundred nanometers in size by McMurry deoxygenation coupling reactions of peripheral carbonyl functional moieties catalyzed by $TiCl_4$ and Zn powders in refluxing THF. Photoluminescence measurements showed that after chemical coupling, the excitation and emission peaks blue-shifted somewhat and the emission intensity increased markedly, likely due to the removal of oxygenated species where quinone-like species were known to be effective electron-acceptors and emission quenchers.

Metal nanoparticles were also prepared and tuned for the applications as high-performance catalysts. In one of the research, gold core@silver semishell Janus nanoparticles were prepared by interfacial chemical etching of Au@Ag core–shell nanoparticles at the air/water interface. The resulting Janus nanoparticles exhibited an asymmetrical distribution of silver on the surface of the gold cores. Interestingly, the Au@Ag semishell Janus nanoparticles exhibited enhanced electrocatalytic activity in oxygen reduction reactions, as compared to their Au@Ag and Ag@Au core–shell counterparts, likely due to a synergistic effect between the gold cores and silver semishells that optimized oxygen binding to the nanoparticle surface. In another research, cysteine-stabilized Ag–Cu hollow nanoshells are prepared by the co-reduction of silver nitrate and cupric nitrate with sodium borohydride in the presence of sodium thiocyanate. When capped with 1-dodecanethiol, the hollow nanoshells become dispersible in apolar organic solvents and the cavity may be exploited for the effective phase-transfer of target molecules such as rhodamine 6G between water and organic media. The Ag–Cu nanoshells also show apparent catalytic activity toward the reduction of 4-nitroaniline by sodium borohydride, a performance that is markedly better than that of the solid counterparts and comparable to leading results in recent literature based on relevant metal catalysts.

DEDICATION

Dedicated

To

My Family

ACKNOWLEDGEMENTS

I am most grateful to my advisor, Professor Shaowei Chen. He is so knowledgeable in chemistry. I learned a great many of experimental, characterization techniques, and data analysis. He offers valuable advice on my research projects and inspires me to think deeply and widely. I am benefited from his guidance, caring, patience, as well as the excellent atmosphere for doing research. Without his support, I would not finish my research projects on time. More importantly, Prof. Chen gave good suggestions to my future career.

I would also like to thank Professor Jin Zhang and Professor Ilan Benjamin to serve on my dissertation committee and offer guidance on my research. I also appreciate help and support from Professor Yat Li in the past 5 years. Special thanks to Prof. David P. Belanger as my committee member in my third-year oral exam.

I would like to thank:

Dr. Yang Song for his help in operation of Langmuir-Blodgett trough and preparation of Janus nanoparticles, and the X-ray photoelectron spectroscopy (XPS) and transmission electron microscopy (TEM) measurements.

Dr. Chris Deming for the XPS and TEM measurement and preparation of nitrogen doped graphene quantum dots.

Dr. Peiguang Hu for his help in the nanoparticle synthesis and electrochemistry.

Jia En Lu for her help in XPS and TEM characterization.

Yi Peng in the help of catalytic reduction reaction of 4-nitroanaline and core/shell structure preparation.

Mauricia D. Rojas-Andrade for his help in the silver-copper alloy nanoparticles preparation.

Prof. Ligui Li, Nan Wang, and Wei Li from South China University of Technology for the help of XPS measurement.

Prof. Yan Guo from Nanjing University of Information Science and Technology in the help of atomic force microscope (AFM) and scanning tunneling microscope (STM) measurement.

Undergraduate student Jake Stofan for the help of silver@gold nanostructures synthesis.

I also want to thank all my other labmates, Prof. Yinghui Ren, Prof. Fen Ran, Dr. Xiaoqin Niu, Prof. Fanli Lu, Prof. Weihua Yang, Prof. Junli Liu, Prof. Xiufang Wang, Prof. Yueming Tan, Dr. Chan Lin, Dr. Bruce Phebus, Dr. Ke Liu, Samantha Sweeney, John Diniz, Rene Mercado, Gustavo Chata, Bingzhang Lu, Lewis Bonny, and all the other undergraduate student researchers.

Many thanks to my friends Gongming Wang, Yichuan Ling, Hanyu Wang, Yi Yang, Tianyi Kou, Teng Zhai, Mingyang Li, Bin Yao and Binbin Luo in the neighbor labs.

Finally, I would like to thank my parents who were always supporting me and encouraging me, and husband Peiguang Hu, who has been accompanying and supporting me for the past few years as a friend, lab mate, and partner.

The text of this dissertation includes reprints of the following previously published material:

Chapter 2: Limei Chen, Yang Song, Peiguang Hu, Christopher P. Deming, Yan Guo, Shaowei Chen, "Interfacial reactivity of ruthenium nanoparticles protected by ferrocenecarboxylates", *Phys. Chem. Chem. Phys.*, 2014, *16*, 18736.

Chapter 3: Limei Chen, Peiguang Hu, Christopher P. Deming, Wei Li, Ligui Li, Shaowei Chen, "Chemical Reactivity of Naphthalenecarboxylate-Protected Ruthenium Nanoparticles: Intraparticle Charge Delocalization Derived from Interfacial Decarboxylation", *J. Phys. Chem. C*, 2015, *119*, 15449.

Chapter 4: Yan Guo†, Limei Chen†, Yang Song, Peiguang Hu, Shaowei Chen, "Ruthenium Nanoparticles Stabilized by the Self-Assembly of Acetylene, Carboxylate, and Thiol Derivatives", *Sci. Adv. Mater.*, 2014, *6*, 1060. († equal contributors)

Chapter 5: Limei Chen, Peiguang Hu, Christopher P. Deming, Nan Wang, Jia En Lu, and Shaowei Chen, "Intervalence Charge Transfer of Ruthenium-Nitrogen Moieties Embedded within Nitrogen-Doped Graphene Quantum Dots", *J. Phys. Chem. C*, 2016, *120*, 13303.

Chapter 6: Limei Chen, Peiguang Hu. Jia En Lu, Shaowei Chen, "Covalent Crosslinking of Graphene Quantum Dots by McMurry Deoxygenation Coupling", *Chem. Asian J.*, 2017, 12, 973.

Chapter 7: Limei Chen, Christopher P. Deming, Yi Peng, Peiguang Hu, Jake Stofan, and Shaowei Chen, "Gold core@silver semishell Janus nanoparticles prepared by interfacial etching", *Nanoscale*, 2016, *8*, 14565.

Chapter 8: Limei Chen, Peiguang Hu, Yi Peng, Jia En Lu, Mauricio D. Rojas-Andrade and Shaowei Chen, "Silver-Copper Hollow Nanoshells as Phase-Transfer Reagents and Catalysts in the Reduction of 4-Nitroaniline", *Part. Part. Syst. Char.*, 2017, 1600358.

Chapter 1

Introduction

1.1 Organically Capped Metal Nanoparticles

Metal nanomaterials represents a novel class of materials since the concept was first introduced by Paul Ehrlich in 1954, and in late 1960s, Professor Peter Paul Speiser developed the first nanoparticles for drug delivery purposes.[1] The convergence of experimental advances, such as the invention of scanning tunneling microscope and atomic force microscope in early 1980s, facilitated the fast growth of nanotechnology. On Oct. 18, 2011, the definition of nanomaterials "A natural, incidental or manufactured material containing particles, in an unbound state or as an aggregate or as an agglomerate and where, for 50% or more of the particles in the number size distribution, one or more external dimensions is in the size range 1 nm – 100 nm" was adopted by the European commission.[2] This field attracts growing public awareness, and it shows tremendous potential implications and feasibility of applications.[3-7] Up to now, nanoparticles can be found everywhere in daily life, such as energy generation and storage, medication, automobiles, UV protection and food supplements.

Due to the shrinking size of metal nanomaterials, the surface-to-volume ratio increases significantly, and the role of the surface increases from minimal in bulk materials to dominant in small nanoparticles. To saturate surface dangling bonds, protecting ligands are generally attached to the nanoparticle surface, forming a capping layer and screening the nanoparticles from the environment. This capping layer and the metal cores constitute the organically capped metal nanoparticles,[8] where both of the metal cores and the protecting organic ligands play an essential role in the determination of the nanoparticle chemical and physical properties.

The size, shape and composition of the metal cores largely dictate the optical, electronic and catalytic properties of metal nanoparticles.[9-13] For example, the UV-vis absorption spectra of spherical gold nanoparticles within the range of 5 to 100 nm show a direct relationship between the localized surface plasma resonance and the particle size.[14] Moreover, when the size of the metal cores diminishes to the (sub)nanometer regime, the nanoparticles act like quantum dots, with multiple absorption bands in UV-vis measurements and apparent photoluminescence emissions in the visible range.[15] In addition, the optical property of gold nanoparticles can be controlled by the core shapes, as nanoplates, nanocubes, nanostars and nanorods exhibit distinctly different UV-vis profiles.[16-20] The catalytic activity of metal nanoparticles is also related to particle shape, size and composition. In general, the catalytic reactions take place on the surface of the metal nanoparticles. Therefore, simply increasing the surface area or tuning the surface chemistry via particle size, shape or alloying can help to optimize the catalytic activity.[21-25] For instance, the oxygen reduction reaction (ORR) activity of Pt surfaces increases in the order of Pt(100) $\ll$ Pt(111) $\approx$ Pt(110), and by adjusting the shape of Pt nanoparticles, the ORR activity may be manipulated and optimized.[22] Moreover, Pt alloying with late/early transition metals may introduce strain or ligand effects to tune the d-band center of platinum for optimal oxygen absorption strength.[23] The plasmonic effects of bimetallic Ag-Pt nanocages with edgeless features have also been utilized to suppress the formation of undesired peroxide intermediates in ORR.[26] Formation of core/shell structures, for example, by coating Ag onto the even more inert Au surface, can also enhance the ORR catalytic activity by about half an order of magnitude in comparison to pure Ag surface.[25]

In addition to the different shapes of metal nanoparticles mentioned above, Janus nanoparticles emerge as a new class of unique materials with asymmetric structures.[27] In the quest for "smart" materials that can be further engineered and functionalized, Janus nanomaterials have been attracting increasing attention for directional functionalization.[28,29] Janus particles are named after the Roman god Janus, showing two hemispheres of distinctly different chemical and physical properties. The significance of Janus particles was addressed in a Nobel lecture entitled "Soft Matter" in 1991 by Nobel Laureate P. G. de Gennes.[30] Janus nanoparticles provide an approach to combine different properties from different materials such as optical, electronic, catalytic and magnetic properties. For example, the plasmonic properties of gold nanoparticles and magnetic properties of Fe_3O_4 nanocrystals can be combined in the formation of binary Janus nanoparticles.[31] Moreover, the asymmetric surface chemistry of Janus nanoparticles may be used as new engineering sites for more complicated surface modifications, such as the growth of Au-TiO_2 heterodimers.[32] Bimetallic Janus nanoparticles may also enhance the charge transfer of dimer-like metal composites, and improve the reactivity of metal catalysts.[33] For instance, the charge transfer from platinum to gold has been observed in asymmetric Pt-Au dumbbell-like nanocrystals, which leads to increased methanol oxidation reaction activity.[33]

The organic ligands bonded to the metal surface also play a significant role in the determination of nanoparticle properties. First, the organic molecules can help to prevent the aggregation of nanoparticles. In general, the ligands provide steric and/or electrostatic stabilization in maintaining the colloidal state by, for instance, bulky hydrocarbon tails in non-polar solvents or charged species in aqueous solutions.[34] Second, the metal core size and shape can be tuned by using different kinds of protecting ligands and manipulation of the concentration ratio with metal precursors.[35-38] For instance, gold nanoparticles with a precise size control between 3.5 and 10 nm have been synthesized by using tannic acid together with sodium citrate at controlled pH, temperature, sodium citrate concentration and gold precursor to seed ratio.[35] Moreover, gold nanorods, nanospheres and nanocubes mentioned above can be obtained with cetrimonium bromide, sodium citrate, and cetrimonium bromide-ascorbic acid as capping ligands in the preparation process.[17-20] Third, the polarity of the nanoparticles can be tuned by the organic ligands.[34,39] For instance, water-soluble Au/Ag nanoparticles have been prepared by an organic-aqueous phase transfer method with amphiphilic oligomers for good biocompatibility.[40] PVP-protected gold nanoparticles in water can also be transferred to organic solvents by ligand exchange with phenylacetylene for the modulation of the electronic properties.[41]

The third factor that will affect properties of organically capped metal nanoparticles is the metal-ligand interactions. Metal nanoparticles can be protected by a diverse range of metal−ligand interfacial bonds, such as metal-thiolate (M-S), metal-carboxylate (M-O), metal−carbon single bonds (M-C), metal−carbene bond (M=C), and metal−acetylide bonds (M−C≡C).[42-44] Among those, mercapto derivatives have been used extensively as the ligands of choice for nanoparticle surface functionalization because of the strong affinity of thiol moieties to metal surfaces. Nevertheless, the metal-carbon conjugated bonds reported in recent years have shown more exciting properties.[44-46] In particular, thanks to the formation of the metal−carbon interfacial conjugated bonds, charge delocalization occurs due to the dπ−pπ interactions between the metal cores and organic ligands, leading to reduced interfacial resistance. For example, the electrical conductivity of solid films of palladium nanoparticles protected by biphenyl through the formation of metal−carbon (sp^2) covalent bonds exhibit metallic temperature dependence in the temperature range of 80 to 320 K.[47] New optical, electronic and electrochemical properties may also be introduced by effective intraparticle charge delocalization between the particle-bound functional groups.[48-51] For example, ruthenium nanoparticles protected by 1-vinylpyrene (Ru=VPy) exhibit two emission bands that are similar to those of dimer counterpart of pyrene, (E)-1,2-di(pyren-1-yl)ethene, suggesting that the particle-bound pyrene moieties behave equivalently to pyrene dimers due to the intraparticle charge delocalization through the conjugated linker by virtue of the Ru=carbene π bonds, while ruthenium nanoparticles capped with 1-allylpyrene (Ru=APy) display only a single emission peak at 392 nm, consistent with monomeric pyrene derivatives of 1-allylpyrene.[50] In electrochemical study, ruthenium nanoparticles functionalized with ferrocenyl moieties through metal−carbene (M=C) π interfacial bonds exhibit two Fc/Fc^+ redox peaks with a potential separation (ΔE_{ox}) of 204 mV due to the intraparticle delocalization, while only one pair of redox peaks is observed for ruthenium nanoparticles functionalized with allylferrocene. In addition, in the study of intraparticle charge transfer, intervalence charge transfer (IVCT) transitions provides a probe of the activation barrier to electron transfer and the charge delocalization extent of the system.[52]

1.2 Intervalence Charge Transfer

IVCT is an electron transfer process (thermal or photoinduced) between donor and acceptor sites facilitated by the significant electronic coupling through a chemical bridge. In general, the metal centers in the mixed-valence system act as the donor and accepter, and a chemical linker acts as the bridge.[52] Mixed-valence systems have been attracting considerable attention since late 1960s. Ru(II)/Ru(III) metal center systems have played a significant role in the study of IVCT, since the report of the Creutz–Taube ion, $[\{Ru(NH_3)_5\}(\mu\text{-pyz})(Ru(NH_3)_5)]^{5+}$ (pyz = pyrazine), in 1973.[53] In complexes like this, the effective overlap of the d-electrons in d(π) orbitals of the metal center with the π-acceptor conjugated ligands allows delocalization of electrons to the other bridged metal centers. Thus, the change of electron density in the oxidation of one metal center can be communicated to the second metal ion through the bridging ligand.[54]

The mixed-valence state of a binuclear composite may be generated either electrochemically or chemically.[54] The magnitude of IVCT can be estimated by spectroscopic and/or electrochemical measurements. As stated in two-state classical and semi-classical theories, the IVCT transition in a dinuclear mixed-valence system can be measured by the vibrational transitional absorption band corresponding to the metal to metal charge transfer (MMCT), while the electronic coupling can be defined by parameter $H_{ab} = \langle \Psi_a | \hat{H} | \Psi_b \rangle$. If the two metal centers are far apart (class I), the electronic coupling is negligible, and no IVCT transition can be observed with $H_{ab} = 0$. In the class II regime, the predicted MMCT absorption band width $\Delta \nu_{1/2}{}^{0}$ is given by eq (1.1),[52,55]

$$\Delta \nu_{1/2}{}^{0} = [16RTln(2\nu_{max})]^{1/2} \tag{1.1}$$

where R is the gas constant, T is temperature (in K), and ν_{max} is the IVCT maximum of the absorption spectrum. The parameter Γ provides a criterion for describing the degree of electronic coupling by eq (1.2),[55]

$$\Gamma = 1 - \Delta \nu_{1/2(\text{experimental})}/[16RTln(2\nu_{max})]^{1/2} = 1 - \Delta \nu_{1/2(\text{experimental})}/\Delta \nu_{1/2}{}^{0} \tag{1.2}$$

where $0 < \Gamma < 0.5$ represents localized Class II systems, $\Gamma \approx 0.5$ at the Class II–III transition, and $\Gamma > 0.5$ for delocalized Class III systems. Moreover, in the class II region, the electronic coupling parameter $H_{ab} = 2.06e^{-2}(\nu_{max}\varepsilon_{max}\Delta\nu_{1/2(experimental)})^{1/2}/r_{ab}$, where ε is the molar extinction coefficient and r_{ab} is the effective electron transfer distance.[55] In electrochemical measurements, the comproportionation constant, K_c, can also help to identify the degree of the electronic delocalization. K_c describes the stability of the mixed-valence metal center $[M^{II}M^{III}]$, as shown in eq (1.3),

$$[M^{II}M^{II}] + [M^{III}M^{III}] \overset{K_c}{\leftrightarrow} 2[M^{II}M^{III}] \tag{1.3}$$

where K_c can be measured from the separation between the two redox potentials for the successive oxidation processes (ΔE), $\Delta G^0 = -RTlnK_c = -nF\Delta E$.[52,54] The higher the ΔE, the more stable the mixed valence metal center. In addition, ΔG^0 can be affected by the repulsion of the two similarly charged metal centers linked by the bridging ligand, the metal-ligand back-bonding interaction and the electronic delocalization.[52]

Depending on the extent of electronic coupling, the mixed valence complexes were categorized by Robin and Day into three classes, class I (uncoupled), class II (moderately coupled), and class III (strongly coupled), which refer to no interaction or little interaction between mixed valence systems, moderate delocalized mixed valence system, and strong delocalized system, respectively. Therefore, studies of the IVCT transitions help to resolve intraparticle charge transfer if the metal cores are protected by organic ligands with mixed-valence metal centers with delocalized connection.[52] In an early study of ethynylferrocene protected platinum nanoparticles (Pt-C≡C-Fc), the size of the platinum nanoparticles is found to significantly affect the electronic coupling.[46] For the 2 nm platinum cores, ΔE_{ox} is estimated to be 280 mV in the dark or under UV photoirradiation.[46] However, for the subnanometer-sized nanoparticles, which show semiconductor-like characteristics with a bandgap of about 1.0 eV, ΔE_{ox} diminishes to 180 mV in the dark and somewhat higher at 200 mV under UV photoirradiation.[46] Apparently, the former has stronger electronic coupling than the latter, and the electronic coupling of the latter may be enhanced by UV photoradiation most likely due to enhanced electrical conductivity of the metal cores as the photon energy is greater than the nanoparticle core bandgap.

1.3 Carbon Nanomaterials

In addition to metal nanoparticles, non-metal nanomaterials like carbon nanomaterials have also been attracting extensive attention due to their new optical, electrical, chemical and electrochemical properties, which lead to extensive applications in catalysis, electronics, biosensing, biomedicine and photonics.[56] Carbon nanomaterials are a class of low-dimensional materials typically in the range of 1 nm to 1 μm, including zero-dimensional carbon nanodots and fullerene, one dimensional carbon nanotube/fiber, two-dimensional graphene. Among these, fullerene as the first member of carbon nanomaterials was discovered about 30 years ago, followed by the discoveries of carbon nanotubes in 1991 and graphene in 2004.[57-59] Carbon nanomaterials are mainly composed of sp^2 carbon atoms forming a conjugated π-system, and further doping and functionalization may introduce defects like sp^3 carbons or heteroatoms (O, N, S, P). Among these carbon nanomaterials, graphene quantum dots (GQDs) represent a unique class of carbonaceous nanomaterials that exhibit a much smaller size (<10 nm) and higher concentration of defects. New optical and electronic properties have been observed for GQDs due to the quantum confinement effects of the nanoscale π-domains. Weak emissions have been observed with bare carbon nanomaterials, and strong emissions were found in functionalized carbon nanomaterials, which are ascribed to small confined conjugated π-domains and defects, respectively.[60] Moreover, in comparison with other fluorescent semiconductors, carbon materials is non-toxic and biocompatible, which is a great advantage for staining and imaging of live organisms.[61]

Carbon nanomaterials have also been attracting intensive interest in the applications as electrocatalysts due to their low costs, high electrical conductivity, high stability and environment friendliness.[62] The electronic properties such as conductivity of graphene nanomaterials depends strongly on their chemical and atomic structures, which can be altered by the manipulation of defect contents and degree of structural disorders.[63] For instance, heteroatom-doped carbon has been proved experimentally and theoretically as a promising metal-free electrocatalyst for ORR. In fact, N, P, B, S-doped or co-doped carbon nanomaterials exhibit improved catalytic reactivity due to the π-conjugation of electrons in the carbon honeycomb structure and the introduction of lone pair electrons from the heteroatom dopants.[64-66] Furthermore, graphene derivatives have high surface area that is essential for the dispersion of metal nanoparticles or metal ions, maximizing the accessible area for electron transfer or mass transport. In addition, graphene derivatives can be further chemically functionalized with carbonyl, epoxides or hydroxyl groups that help to immobilize metal nanoparticles and the stability of the catalysts can be enhanced through strong metal-support interaction.[67] More importantly, the catalytic reactivity of metal nanoparticles can be further manipulated by the electronic interactions between the carbon substrates and metal nanoparticles.[62] For instance, the ORR activity of platinum nanoparticles supported on GQDs can be tuned by the modification of defects concentrations in GQDs, by which the electron transfer from Pt to GQDs can be optimized for the best oxygen absorption strength.[68]

The preparation methods for carbon nanomaterials can be generally classified into “top-down” and “bottom-up” processes. The former involves exfoliation or breaking down of graphitic materials via chemical, electrochemical, or metal intercalation, while the latter is realized by pyrolysis or carbonization of small organic molecules.[69] By adjusting the preparation conditions, the size, optical and chemical properties of the carbon nanomaterials can be modified.[70] For instance, GQDs and its derivatives have been explored for potential applications in the fields of optoelectronics, catalysis, energy generation and storage.[71-73] Moreover, new applications can be explored by developing effective procedures for the controlled "bottom-up" assembly of graphene derivatives into large, complicated architectures.[74]

1.4 Dissertation Outline

The dissertation research described herein are to manipulate the ligand functionalization of metal nanoparticles, metal core structures and engineering of carbon nanomaterials to study the influence of metal-organic interactions and metal core structures on the chemical, optical and electrochemical properties of nanoparticles and their applications in (electro)catalysis. The structures of the nanoparticles are studied by AFM (atomic force microscopy) and TEM (transmission electron microscopy), XPS (X-ray photoelectron spectroscopy), UV-vis, photoluminescence, proton nuclear magnetic resonance (NMR), FTIR, near infra-red, Raman, and electrochemical measurements. The dissertation consists of the following chapters:

- Chapter 2, interfacial reactivity of ruthenium nanoparticles protected by ferrocenecarboxylates.
- Chapter 3, chemical reactivity of naphthalenecarboxylate-protected ruthenium nanoparticles: intraparticle charge delocalization derived from interfacial decarboxylation.
- Chapter 4, electron-transfer properties of the ruthenium nanoparticles capped

with 1-dodecyne, laurate and 1-dodecanethiol examined by scanning tunneling spectroscopic (STS) measurements.

- Chapter 5, studies of IVCT between embedded Ru ions bridged by the highly conductive GQD by near-infrared spectroscopy and cyclic voltammetry measurements.
- Chapter 6, covalent crosslinking of GQDs forming ensembles of a few hundred nanometers in size by McMurry deoxygenation coupling reactions.
- Chapter 7, gold core@silver semishell Janus nanoparticles prepared by interfacial etching for enhanced ORR electrocatalytic activity.
- Chapter 8, cysteine-stabilized Ag–Cu hollow nanoshells for the effective phase-transfer of target molecules such as rhodamine 6G between water and organic media and for the catalytic reduction of 4-nitroaniline by sodium borohydride.

1.5 References

(1) Kreuter, J. Nanoparticles - a historical perspective. *Int J Pharm* **2007**, *331*, 1-10.

(2) Nanomaterials. *European commission*.

(3) Qin, X.; Xu, A.; Liu, L.; Deng, W.; Chen, C.; Tan, Y.; Fu, Y.; Xie, Q.; Yao, S. Ultrasensitive electrochemical immunoassay of proteins based on in situ duple amplification of gold nanoparticle biolabel signals. *Chemical communications* **2015**, *51*, 8540-8543.

(4) Bodhisatwa, D.; Fernandez, F.; John, A.; Sharma, C. P. Synthesis, Characterization and Bio-Labeling Studies of Trypsin Stabilized Silver Quantum Clusters. *J Biomater Tiss Eng* **2012**, *2*, 299-306.

(5) Howes, P. D.; Chandrawati, R.; Stevens, M. M. Colloidal nanoparticles as advanced biological sensors. *Science* **2014**, *346,* 1247390.

(6) Guo, L. H.; Xu, Y.; Ferhan, A. R.; Chen, G. N.; Kim, D. H. Oriented Gold Nanoparticle Aggregation for Colorimetric Sensors with Surprisingly High Analytical Figures of Merit. *J Am Chem Soc* **2013**, *135*, 12338-12345.

(7) Guo, S. J.; Zhang, X.; Zhu, W. L.; He, K.; Su, D.; Mendoza-Garcia, A.; Ho, S. F.; Lu, G.; Sun, S. H. Nanocatalyst Superior to Pt for Oxygen Reduction Reactions: The Case of Core/Shell Ag(Au)/CuPd Nanoparticles. *J Am Chem Soc* **2014**, *136*, 15026-15033.

(8) Nuzzo, R. G.; Zegarski, B. R.; Dubois, L. H. Fundamental-Studies of the Chemisorption of Organosulfur Compounds on Au(111) - Implications for Molecular Self-Assembly on Gold Surfaces. *Journal of the American Chemical Society* **1987**, *109*, 733-740.

(9) Boles, M. A.; Ling, D. S.; Hyeon, T.; Talapin, D. V. The surface science of nanocrystals. *Nat Mater* **2016**, *15*, 364-364.

(10) Hu, P. G.; Song, Y.; Chen, L. M.; Chen, S. W. Electrocatalytic activity of alkyne-functionalized AgAu alloy nanoparticles for oxygen reduction in alkaline media. *Nanoscale* **2015**, *7*, 9627-9636.

(11) Haes, A. J.; Van Duyne, R. P. A nanoscale optical biosensor: sensitivity and selectivity of an approach based on the localized surface plasmon resonance spectroscopy of triangular silver nanoparticles. *J Am Chem Soc* **2002**, *124*, 10596-10604.

(12) Liong, M.; Lu, J.; Kovochich, M.; Xia, T.; Ruehm, S. G.; Nel, A. E.; Tamanoi, F.; Zink, J. I. Multifunctional inorganic nanoparticles for imaging, targeting, and drug delivery. *ACS Nano* **2008**, *2*, 889-896.

(13) Pumera, M. Graphene-based nanomaterials for energy storage. *Energ Environ Sci* **2011**, *4*, 668-674.

(14) Haiss, W.; Thanh, N. T. K.; Aveyard, J.; Fernig, D. G. Determination of size and concentration of gold nanoparticles from UV-Vis spectra. *Anal Chem* **2007**, *79*, 4215-4221.

(15) Farrag, M.; Tschurl, M.; Heiz, U. Chiral Gold and Silver Nanoclusters: Preparation, Size Selection, and Chiroptical Properties. *Chem Mater* **2013**, *25*, 862-870.

(16) Chen, Y.; Gu, X.; Nie, C. G.; Jiang, Z. Y.; Xie, Z. X.; Lin, C. J. Shape controlled growth of gold nanoparticles by a solution synthesis. *Chem Commun* **2005**, 4181-4183.

(17) Kozlovskaya, V.; Kharlampieva, E.; Khanal, B. P.; Manna, P.; Zubarev, E. R.; Tsukruk, V. V. Ultrathin Layer-by-Layer Hydrogels with Incorporated Gold Nanorods as pH-Sensitive Optical Materials. *Chem Mater* **2008**, *20*, 7474-7485.

(18) Li, C. F.; Li, D. X.; Wan, G. Q.; Xu, J.; Hou, W. G. Facile synthesis of concentrated gold nanoparticles with low size-distribution in water: temperature and pH controls. *Nanoscale Res Lett* **2011**, *6,* 440.

(19) Sau, T. K.; Murphy, C. J. Room temperature, high-yield synthesis of multiple shapes of gold nanoparticles in aqueous solution. *Journal of the American Chemical Society* **2004**, *126*, 8648-8649.

(20) Navarro, J. R. G.; Manchon, D.; Lerouge, F.; Blanchard, N. P.; Marotte, S.; Leverrier, Y.; Marvel, J.; Chaput, F.; Micouin, G.; Gabudean, A. M.; Mosset, A.; Cottancin, E.; Baldeck, P. L.; Kamada, K.; Parola, S. Synthesis of PEGylated gold nanostars and bipyramids for intracellular uptake. *Nanotechnology* **2012**, *23,* 465602.

(21) Park, J.; Wang, H. L.; Vara, M.; Xia, Y. N. Platinum Cubic Nanoframes with Enhanced Catalytic Activity and Durability Toward Oxygen Reduction. *Chemsuschem* **2016**, *9*, 2855-2861.

(22) Markovic, N. M.; Schmidt, T. J.; Stamenkovic, V.; Ross, P. N. Oxygen Reduction Reaction on Pt and Pt Bimetallic Surfaces: A Selective Review. *Fuel Cells* **2001**, *1*, 105-116.

(23) Toda, T.; Igarashi, H.; Uchida, H.; Watanabe, M. Enhancement of the electroreduction of oxygen on Pt alloys with Fe, Ni, and Co. *J Electrochem Soc* **1999**, *146*, 3750-3756.

(24) Back, S.; Yeom, M. S.; Jung, Y. Active Sites of Au and Ag Nanoparticle Catalysts for CO2 Electroreduction to CO. *Acs Catal* **2015**, *5*, 5089-5096.

(25) Yang, C. X.; Huang, B.; Xiao, L.; Ren, Z. D.; Liu, Z. L.; Lu, J. T.; Zhuang, L. Activating Ag by even more inert Au: a peculiar effect on electrocatalysis toward oxygen reduction in alkaline media. *Chem Commun* **2013**, *49*, 11023-11025.

(26) Lin, S. C.; Hsu, C. S.; Chiu, S. Y.; Liao, T. Y.; Chen, H. M. Edgeless Ag-Pt Bimetallic Nanocages: In Situ Monitor Plasmon-Induced Suppression of Hydrogen Peroxide Formation. *Journal of the American Chemical Society* **2017**, *139*, 2224-2233.

(27) Walther, A.; Muller, A. H. Janus particles: synthesis, self-assembly, physical properties, and applications. *Chemical reviews* **2013**, *113*, 5194-5261.

(28) Koo, J. H.; Kim, D.; Kim, J. G.; Jeong, H.; Kim, J.; Lee, I. S. Asymmetric silica encapsulation toward colloidal Janus nanoparticles: a concave nanoreactor for template-synthesis of an electocatalytic hollow Pt nanodendrite. *Nanoscale* **2016**, *8*, 14593-14599.

(29) Song, Y.; Chen, S. W. Janus Nanoparticles as Versatile Phase-Transfer Reagents. *Langmuir* **2014**, *30*, 6389-6397.

(30) Degennes, P. G. Soft Matter. *Science* **1992**, *256*, 495-497.

(31) Shi, W. L.; Zeng, H.; Sahoo, Y.; Ohulchanskyy, T. Y.; Ding, Y.; Wang, Z. L.; Swihart, M.; Prasad, P. N. A general approach to binary and ternary hybrid nanocrystals. *Nano Lett* **2006**, *6*, 875-881.

(32) Pradhan, S.; Ghosh, D.; Chen, S. W. Janus Nanostructures Based on Au-TiO2 Heterodimers and Their Photocatalytic Activity in the Oxidation of Methanol. *Acs Appl Mater Inter* **2009**, *1*, 2060-2065.

(33) Wang, C.; Tian, W. D.; Ding, Y.; Ma, Y. Q.; Wang, Z. L.; Markovic, N. M.; Stamenkovic, V. R.; Daimon, H.; Sun, S. H. Rational Synthesis of Heterostructured Nanoparticles with Morphology Control. *Journal of the American Chemical Society* **2010**, *132*, 6524-6529.

(34) Sperling, R. A.; Parak, W. J. Surface modification, functionalization and bioconjugation of colloidal inorganic nanoparticles. *Philos T R Soc A* **2010**, *368*, 1333-1383.

(35) Piella, J.; Bastus, N. G.; Puntes, V. Size-Controlled Synthesis of Sub-10-nanometer Citrate-Stabilized Gold Nanoparticles and Related Optical Properties. *Chem Mater* **2016**, *28*, 1066-1075.

(36) He, B. L.; Tan, J. J.; Kong, Y. L.; Liu, H. F. Synthesis of size controlled Ag nanoparticles. *J Mol Catal a-Chem* **2004**, *221*, 121-126.

(37) Park, H. H.; Zhang, X.; Choi, Y. J.; Kim, H.; Park, H. H.; Hill, R. H. Facile synthesis and size control of Ag nanoparticles by a photochemical reduction at room temperature. *J Ceram Soc Jpn* **2010**, *118*, 1002-1005.

(38) Chen, L. Y.; Xu, J. Q.; Choi, H.; Konishi, H.; Jin, S.; Li, X. C. Rapid control of phase growth by nanoparticles. *Nat Commun* **2014**, *5,* 3879.

(39) Chen, L. M.; Deming, C. P.; Peng, Y.; Hu, P. G.; Stofan, J.; Chen, S. W. Gold core@silver semishell Janus nanoparticles prepared by interfacial etching. *Nanoscale* **2016**, *8*, 14565-14572.

(40) Zhou, C. H.; Xu, W. W.; Lou, S. Y.; Zhang, Z. J.; Li, L. S.; Chen, J. M. Formation of water-soluble gold and silver nanocrystals using a phase transfer method based on surface-bound interactions. *Colloid Surface A* **2010**, *355*, 139-145.

(41) Maity, P.; Tsunoyama, H.; Yamauchi, M.; Xie, S. H.; Tsukuda, T. Organogold Clusters Protected by Phenylacetylene. *Journal of the American Chemical Society* **2011**, *133*, 20123-20125.

(42) Guo, Y.; Chen, L. M.; Song, Y.; Hu, P. G.; Chen, S. W. Ruthenium Nanoparticles Stabilized by the Self-Assembly of Acetylene, Carboxylate, and Thiol Derivatives. *Sci Adv Mater* **2014**, *6*, 1060-1067.

(43) Chen, W.; Davies, J. R.; Ghosh, D.; Tong, M. C.; Konopelski, J. P.; Chen, S. W. Carbene-functionalized ruthenium nanoparticles. *Chem Mater* **2006**, *18*, 5253-5259.

(44) Kang, X. W.; Zuckerman, N. B.; Konopelski, J. P.; Chen, S. W. Alkyne-Functionalized Ruthenium Nanoparticles: Ruthenium-Vinylidene Bonds at the Metal-Ligand Interface. *Journal of the American Chemical Society* **2012**, *134*, 1412-1415.

(45) Kang, X. W.; Chen, W.; Zuckerman, N. B.; Konopelski, J. P.; Chen, S. W. Intraparticle Charge Delocalization of Carbene-Functionalized Ruthenium Nanoparticles Manipulated by Selective Ion Binding. *Langmuir* **2011**, *27*, 12636-12641.

(46) Hu, P. G.; Chen, L. M.; Deming, C. P.; Kang, X. W.; Chen, S. W. Nanoparticle-Mediated Intervalence Charge Transfer: Core-Size Effects. *Angew Chem Int Edit* **2016**, *55*, 1455-1459.

(47) Ghosh, D.; Chen, S. W. Palladium nanoparticles passivated by metal-carbon covalent linkages (vol 18, pg 755, 2008). *J Mater Chem* **2009**, *19*, 9287-9287.

(48) Chen, W.; Chen, S. W.; Ding, F. Z.; Wang, H. B.; Brown, L. E.; Konopelski, J. P. Nanoparticle-mediated intervalence transfer. *Journal of the American Chemical Society* **2008**, *130*, 12156-12162.

(49) Chen, W.; Zuckerman, N. B.; Kang, X. W.; Ghosh, D.; Konopelski, J. P.; Chen, S. W. Alkyne-Protected Ruthenium Nanoparticles. *J Phys Chem C* **2010**, *114*, 18146-18152.

(50) Chen, W.; Zuckerman, N. B.; Lewis, J. W.; Konopelski, J. P.; Chen, S. W. Pyrene-Functionalized Ruthenium Nanoparticles: Novel Fluorescence Characteristics from Intraparticle Extended Conjugation. *J Phys Chem C* **2009**, *113*, 16988-16995.

(51) Chen, W.; Pradhan, S.; Chen, S. W. Photoluminescence and conductivity studies of anthracene-functionalized ruthenium nanoparticles. *Nanoscale* **2011**, *3*, 2294-2300.

(52) D'Alessandro, D. M.; Keene, F. R. Current trends and future challenges in the experimental, theoretical and computational analysis of intervalence charge transfer (IVCT) transitions. *Chem Soc Rev* **2006**, *35*, 424-440.

(53) Creutz, C.; Taube, H. Binuclear Complexes of Ruthenium Ammines. *Journal of the American Chemical Society* **1973**, *95*, 1086-1094.

(54) Ward, M. D. Metal-Metal Interactions in Binuclear Complexes Exhibiting Mixed-Valency - Molecular Wires and Switches. *Chem Soc Rev* **1995**, *24*, 121-134.

(55) D'Alessandro, D. M.; Keene, F. R. Intervalence charge transfer (IVCT) in ruthenium dinuclear and trinuclear assemblies containing the bridging ligand HAT {1,4,5,8,9,12-hexaazatriphenylene}. *Chem-Eur J* **2005**, *11*, 3679-3688.

(56) Hong, G. S.; Diao, S. O.; Antaris, A. L.; Dai, H. J. Carbon Nanomaterials for Biological Imaging and Nanomedicinal Therapy. *Chem Rev* **2015**, *115*, 10816-10906.

(57) Kroto, H. W.; Heath, J. R.; Obrien, S. C.; Curl, R. F.; Smalley, R. E. C-60 - Buckminsterfullerene. *Nature* **1985**, *318*, 162-163.

(58) Iijima, S. Helical Microtubules of Graphitic Carbon. *Nature* **1991**, *354*, 56-58.

(59) Novoselov, K. S.; Geim, A. K.; Morozov, S. V.; Jiang, D.; Zhang, Y.; Dubonos, S. V.; Grigorieva, I. V.; Firsov, A. A. Electric field effect in atomically thin carbon films. *Science* **2004**, *306*, 666-669.

(60) Cao, L.; Meziani, M. J.; Sahu, S.; Sun, Y. P. Photoluminescence Properties of Graphene versus Other Carbon Nanomaterials. *Accounts Chem Res* **2013**, *46*, 171-180.

(61) LeCroy, G. E.; Sonkar, S. K.; Yang, F.; Veca, L. M.; Wang, P.; Tackett, K. N.; Yu, J. J.; Vasile, E.; Qian, H. J.; Liu, Y. M.; Luo, P.; Sun, Y. P. Toward

Structurally Defined Carbon Dots as Ultracompact Fluorescent Probes. *Acs Nano* **2014**, *8*, 4522-4529.

(62) Peng, Y.; Lu, B.; Wang, N.; Li, L.; Chen, S. Impacts of interfacial charge transfer on nanoparticle electrocatalytic activity towards oxygen reduction. *Phys Chem Chem Phys* **2017**, *19*, 9336-9348.

(63) Chen, D.; Feng, H. B.; Li, J. H. Graphene Oxide: Preparation, Functionalization, and Electrochemical Applications. *Chem Rev* **2012**, *112*, 6027-6053.

(64) Gong, K. P.; Du, F.; Xia, Z. H.; Durstock, M.; Dai, L. M. Nitrogen-Doped Carbon Nanotube Arrays with High Electrocatalytic Activity for Oxygen Reduction. *Science* **2009**, *323*, 760-764.

(65) Wu, J. J.; Ma, L. L.; Yadav, R. M.; Yang, Y. C.; Zhang, X.; Vajtai, R.; Lou, J.; Ajayan, P. M. Nitrogen-Doped Graphene with Pyridinic Dominance as a Highly Active and Stable Electrocatalyst for Oxygen Reduction. *Acs Appl Mater Inter* **2015**, *7*, 14763-14769.

(66) Wang, L.; Dong, H. L.; Guo, Z. Y.; Zhang, L. L.; Hou, T. J.; Li, Y. Y. Potential Application of Novel Boron-Doped Graphene Nanoribbon as Oxygen Reduction Reaction Catalyst. *J Phys Chem C* **2016**, *120*, 17427-17434.

(67) Liu, M. M.; Zhang, R. Z.; Chen, W. Graphene-Supported Nanoelectrocatalysts for Fuel Cells: Synthesis, Properties, and Applications. *Chem Rev* **2014**, *114*, 5117-5160.

(68) Song, Y.; Chen, S. W. Graphene Quantum-Dot-Supported Platinum Nanoparticles: Defect-Mediated Electrocatalytic Activity in Oxygen Reduction. *Acs Appl Mater Inter* **2014**, *6*, 14050-14060.

(69) Zhu, S. J.; Song, Y. B.; Zhao, X. H.; Shao, J. R.; Zhang, J. H.; Yang, B. The photoluminescence mechanism in carbon dots (graphene quantum dots, carbon nanodots, and polymer dots): current state and future perspective. *Nano Res* **2015**, *8*, 355-381.

(70) Chen, A. B.; Zhao, C. C.; Yu, Y. F.; Yang, J. H. Graphene Quantum Dots Derived from Carbon Fibers for Oxidation of Dopamine. *J Wuhan Univ Technol* **2016**, *31*, 1294-1297.

(71) Dai, L. M.; Chang, D. W.; Baek, J. B.; Lu, W. Carbon Nanomaterials for Advanced Energy Conversion and Storage. *Small* **2012**, *8*, 1130-1166.

(72) Wen, J.; Xu, Y. Q.; Li, H. J.; Lu, A. P.; Sun, S. G. Recent applications of carbon nanomaterials in fluorescence biosensing and bioimaging. *Chemical communications* **2015**, *51*, 11346-11358.

(73) Li, X. M.; Rui, M. C.; Song, J. Z.; Shen, Z. H.; Zeng, H. B. Carbon and Graphene Quantum Dots for Optoelectronic and Energy Devices: A Review. *Adv Funct Mater* **2015**, *25*, 4929-4947.

(74) Li, X. L.; Zhang, G. Y.; Bai, X. D.; Sun, X. M.; Wang, X. R.; Wang, E.; Dai, H. J. Highly conducting graphene sheets and Langmuir-Blodgett films. *Nat Nanotechnol* **2008**, *3*, 538-542.

Chapter 2

Interfacial reactivity of ruthenium nanoparticles protected by ferrocenecarboxylates

Reproduced with permission from (Limei Chen, Yang Song, Peiguang Hu, Christopher P. Deming, Yan Guo, Shaowei Chen, "Interfacial reactivity of ruthenium nanoparticles protected by ferrocenecarboxylates", Phys. Chem. Chem. Phys., 2014, 16, 18736.)

2.1 Introduction

Monolayer-protected metal nanoparticles have attracted great interest in diverse research fields such as catalysis,[1] energy conversion and storage,[2] biological and chemical sensing.[3] In these studies, metal-ligand bonding interactions have been found to play a key role in the determination of the nanoparticle size, structure, stability, and reactivity.[4] Whereas mercapto derivatives have been used extensively as the ligands of choice for nanoparticle surface functionalization because of the strong affinity of the thiol moiety to metal surfaces, recently a number of studies have been carried out focusing on the synthesis of metal nanoparticles stabilized by other metal-ligand interfacial bonds. With the new interfacial chemistry, not only the growth dynamics of the nanoparticles changes accordingly, but more interestingly the nanoparticle optical and electronic properties can also be manipulated at an unprecedented level as a result of the unique bonding interactions between the metal cores and the organic capping ligands. For instance, alkylamines have been used as capping ligands in the control of the size and shape of ruthenium nanoparticles because of their strong coordination bonds. Experimentally it has been observed that the ruthenium particles tend to be elongated or form rod-like structures thanks to the fast exchange of amine ligands at the particle surface.[5] However, in the presence of ionic liquids (*e. g.*, imidazolium-derived ionic liquids), spherical nanoparticles are obtained as ligand exchange is inhibited.[6] Stable metal nanoparticles have also been prepared by taking advantage of the self-assembly of diazo and acetylene derivatives onto metal nanoparticle surfaces forming metal–carbene (M=C), –acetylide (M–C≡), or –vinylidene (M=C=C) bonds.[7-

[11] With the formation of these conjugated interfacial bonds, extensive intraparticle charge delocalization occurs between the particle-bound functional moieties, leading to the emergence of optical and electronic properties that are analogous to those of their dimeric derivatives.[12-15]

In these studies, ruthenium nanoparticles have been used rather extensively as the illustrating examples, possibly because of the rich chemistry manifested in relevant ruthenium complexes.[16] Among the methods for the synthesis of ruthenium nanoparticles, thermolysis is an effective route where Ru(III) precursors are reduced in alcohols in the presence of acetate salts.[17] The resulting ruthenium colloids are presumed to be stabilized by the acetate ligands, which may be replaced by ligand exchange with thiols or alkyne ligands.[9] However, other carboxylate derivatives have rarely been used,[2,18]and few studies have focused on the interfacial interactions between the metal cores and the carboxylate groups. This is the primary motivation of the present study.

Herein, we used sodium ferrocenecarboxylate as a new type of protecting ligands for the stabilization of ruthenium nanoparticles by the formation of Ru–O interfacial bonds, where the ferrocenyl groups were exploited as a molecular probe to examine the nanoparticle interfacial reactivity. Interestingly, sodium ferrocenecarboxylate was found to act as a better stabilizer than sodium acetate for ruthenium nanoparticles. The resulting nanoparticles were then subject to detailed characterizations by a wide array of spectroscopic and microscopic measurements, including transmission electron microscopy (TEM), ^{1}H nuclear magnetic resonance

(NMR) spectroscopy, ultraviolet-visible (UV-vis) absorption, as well as Fourier-transformed infrared (FTIR) spectroscopy. The ligands were found to form highly polarized Ru–O bonds at the metal-ligand interface in a bidentate configuration,[19] in consistence with *x*-ray photoelectron spectroscopic (XPS) measurements which exhibited a marked increase of the Fe2p binding energy and electrochemical measurements where the formal potential of the particle-bound ferrocenyl moieties increased by ca. 120 mV. Notably, the nanoparticles might undergo galvanic exchange reactions with Pd(II), and after hydrothermal reactions, the resulting nanoparticles exhibited voltammetric results that suggested intervalence charge transfer between the ferrocenyl groups on the nanoparticle surface, likely because of palladium-catalyzed decarboxylation of the surface ligands and the ferrocenyl groups were now directly bonded to the metal surfaces.

2.2 Experimental Section

Chemicals

Ruthenium chloride ($RuCl_3$, 35-40% Ru, ACROS), sodium hydroxide (NaOH, extra pure, ACROS), 1, 2-propanediol (ACROS), palladium(II) chloride ($PdCl_2$, 59% Pd, ACROS), hydrochloric acid (HCl, ACS Reagent, Sigma–Aldrich) and ferrocenecarboxylic acid (FCA, 98+%, Santa Cruz Biotechnology) were used as received. All solvents were obtained from typical commercial sources and used without further treatment. Water was supplied by a Barnstead Nanopure water system (18.3 MΩ cm).

Preparation of ferrocenecarboxylate-stabilized ruthenium nanoparticles

Ferrocenecarboxylate-stabilized Ru nanoparticles were synthesized by thermolytic reduction of $RuCl_3$ in 1,2-propanediol, similar to the preparation of acetate-stabilized Ru colloids described in previous studies.[7] Briefly, 0.1 mmol of $RuCl_3$, 0.6 mmol of FCA and 0.6 mmol of sodium hydroxide were dissolved in 100 mL of 1, 2-propanediol. The solution was then heated to 175 °C for 2 h under vigorous stirring. During the reaction, the color of the solution was found to change from dark orange to dark brown indicating the formation of Ru nanoparticles. The colloid solution was then cooled to room temperature and underwent dialysis for 3 d in nanopure water to remove excessive ligands of FCA and 1,2-propanediol. The solution was then collected and dried by rotary evaporation, and the solids were rinsed extensively with acetonitrile to remove residual free ligands. The resulting purified ruthenium nanoparticles were denoted as RuFCA.

Decarboxylation of RuFCA nanoparticles

The experimental procedure is depicted in Scheme 2.1. A H_2PdCl_4 solution was first prepared by dissolving $PdCl_2$ (0.1 mmol) in hydrochloric acid (1 mL) at 50 °C. When cooled down to room temperature, the solution was added to the RuFCA nanoparticle solution in 1,3-propanediol for galvanic exchange. After magnetic stirring for 24 h, the solution was purified by dialysis in nanopure water and rinsing by acetonitrile to remove excessive free ligands and reaction by-products. The solution was then added into a Teflon-lined autoclave, which was sealed and placed in an oven and heated at 200 °C for 4 h. The precipitates were collected and purified by rinsing extensively with acetonitrile; and the resulting nanoparticles were referred to as RuPdFCA.

Characterizations

The particles core diameters were determined by TEM measurements with a JEOL-F 200 KV field-emission analytical transmission electron microscope. The samples were prepared by casting a drop of the particle solution in *N,N*-dimethylformamide (DMF) onto a 200-mesh holey carbon-coated copper grid. ^{1}H NMR spectroscopic measurements were carried out by using concentrated solutions of the nanoparticles in deuterated DMF with a Varian UnityPlus 500 MHz NMR spectrometer and the absence of any sharp features indicated that the nanoparticles were free of excessive monomeric ligands. UV-vis spectroscopic studies were performed with an ATI Unicam UV4 spectrometer using a 10 mm quartz cuvette with a resolution of 2 nm. FTIR measurements were carried out with a Perkin-Elmer FTIR spectrometer (Spectrum One, spectral resolution 4 cm^{-1}), where the samples were prepared by casting the particle solutions onto a ZnSe disk. X-Ray photoelectron spectra (XPS) were recorded with a PHI 5400/XPS instrument equipped with an Al Kα source operated at 350W and at 10^{-9} Torr. Silicon wafers were sputtered by argon ions to remove carbon from the background and used as substrates. The spectra were charge-referenced to the Si2p peak (93.03 eV).

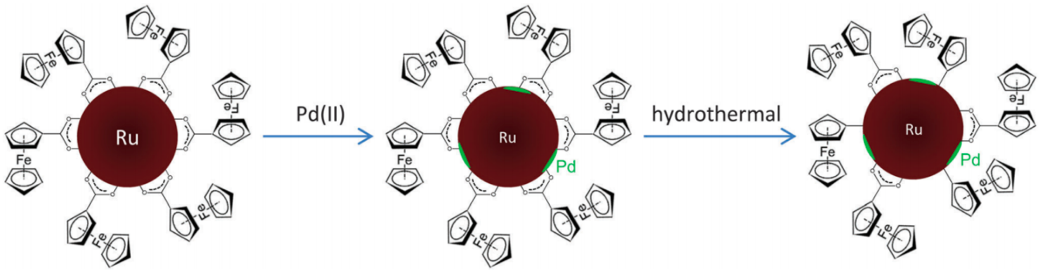

Scheme 2.1

Electrochemistry

Voltammetric measurements were carried out with a CHI 440 electrochemical workstation. A polycrystalline gold disk electrode (sealed in glass tubing) was used as the working electrode, with a surface area of 0.70 mm^2. A Ag/AgCl wire and a Pt coil were used as the (quasi)reference and counter electrodes, respectively. The gold electrode was first polished with 0.05 μm alumina slurries and then cleansed by sonication in H_2SO_4 and nanopure water successively. Note that the potentials were all calibrated against the formal potential of ferrocene monomers (Fc^+/Fc) in the same electrolyte solution.

2.3 Results and Discussion

Figure 2.1 depicts a representative TEM micrograph of the RuFCA nanoparticles. It can be seen that the nanoparticles were well dispersed without apparent aggregation, suggesting effective stabilization of the nanoparticles by the ferrocenecarboxylate ligands. Statistical analysis based on more than 100 nanoparticles showed that the nanoparticles were largely within the narrow range of 0.80 to 1.70 nm in diameter, with a mean value of 1.22 ± 0.23 nm, as manifested in the figure inset.

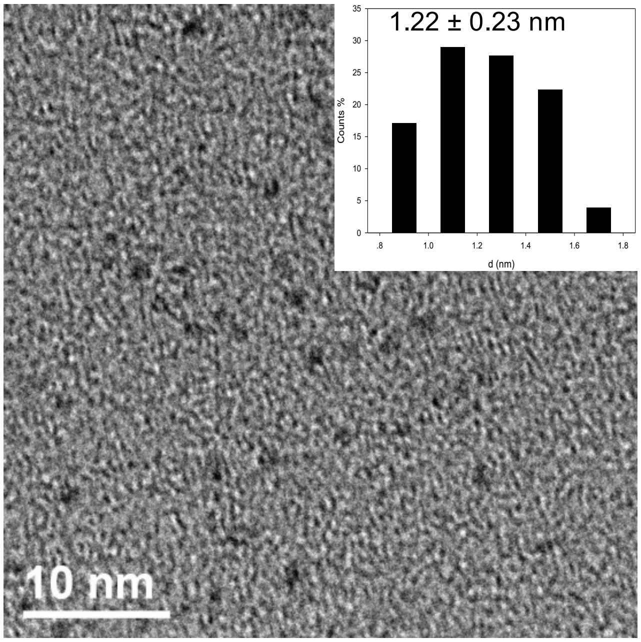

Figure 2.1 Representative TEM micrograph of RuFCA nanoparticles. The inset shows the particle core size histogram. The scale bar is 10 nm.

The structures of the RuFCA nanoparticles were then examined by NMR measurements. Figure 2.2 shows the ^{1}H NMR spectra of RuFCA and monomeric FCA in deuterated DMF. For the monomeric FCA ligands (black curve), three sharp multiplets can be identified at 4.75, 4.46 and 4.24 ppm with the ratio of the integrated peak areas at about a:b:c = 1.08:1:2.59. These are consistent with those of the ferrocenyl ring protons as depicted in the figure inset (the peak at ca 8.0 ppm was from the DMF solvent and that at 3.5 ppm was due to residual water in the solvent). For the RuFCA nanoparticles (red curve), however, these three peaks were found to shift somewhat to 4.66, 4.40, and 4.20 ppm, which suggests decreasing electron density (bonding order) of the ferrocenyl skeleton (*vide infra*) as compared to that of the monomeric ligands.

In addition, the peaks were apparently broadened and the ratio of the integrated peak areas reduced to 0.37:1:1.72. The broadening can be attributed to inhomogeneity of the magnetic field in the local chemical environments on the ruthenium nanoparticle surface.[20] The closer the protons are to the metal cores, the stronger the influence is. Thus the deviation of the ratio of the (a), (b) and (c) protons from the expected value of 1:1:2.5 is most likely due to the varied degrees of signal broadening. In particular, the apparent underestimation of protons (a) may be accounted for by their close proximity to the carboxylic acid moieties that are the presumed anchoring sites onto the nanoparticle surface. Furthermore, the lack of sharp features in the NMR measurements indicates that the nanoparticles were free of excessive monomeric ligands. Such a phenomenon has been observed extensively with organically capped metal nanoparticles, as a result of (1) spin relaxation from dipolar interactions at the ligand/core interface and (2) spin-spin relaxation broadening caused by particle core size dispersity.[7]

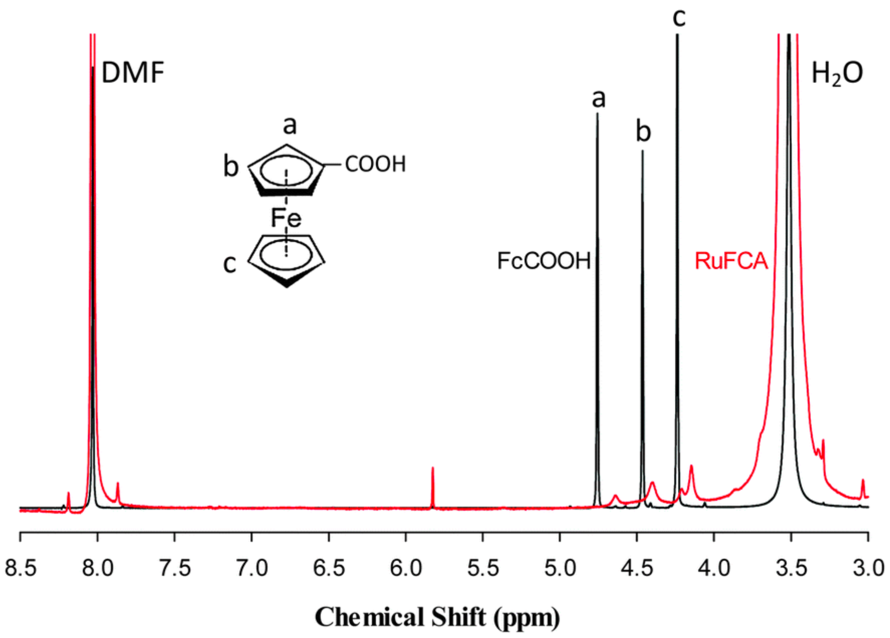

Figure 2.2 1H NMR spectra of (black curve) monomeric FCA and (red curve) RuFCA nanoparticles in deuterated DMF.

FTIR measurements further confirmed that the FCA ligands were indeed bound on the nanoparticle surface with the carboxylate moieties symmetrically anchored to Ru, as depicted in Figure 2.3. For the FCA monomers (black curve), the peaks at 1654 cm^{-1} and 1284 cm^{-1} may be assigned to the C=O and C–O stretching vibrations of the carboxyl moieties, respectively; the ferrocenyl ring skeleton (C=C) vibrations can be found at 1476 and 1400 cm^{-1}, along with the cyclopentadienyl C-H vibrational stretch at about 3095 cm^{-1} and bending vibration at 1161 cm^{-1}.[21-23] Interestingly, when the ligands were bound onto the ruthenium nanoparticle surface (red curve), the C–O vibration peaks diminished significantly and the C=O band red-shifted to 1635 cm^{-1}. This decrease of bonding order might be accounted for by the formation of carboxylate-like species when the ligands were bound onto the nanoparticle surface in a bidentate configuration (Scheme 2.1), because of the strong coupling between C=O and C–O.[2,18] In addition, the ring skeleton vibrations of the ferrocenyl moieties red-shift slightly to 1474 and 1393 cm^{-1}. This is consistent with the red-shift of the ferrocenyl ring protons in NMR measurements as observed in Figure 2.2. Additionally, one may notice that three small peaks emerged in the region of 1900 to 2100 cm^{-1}. These are likely due to Ru–H vibrational stretches that were formed in the thermolytic synthesis of ruthenium nanoparticles, where the variation of the vibrational frequencies might be ascribed to the Ru–H bonds at different surface sites.[24-26]

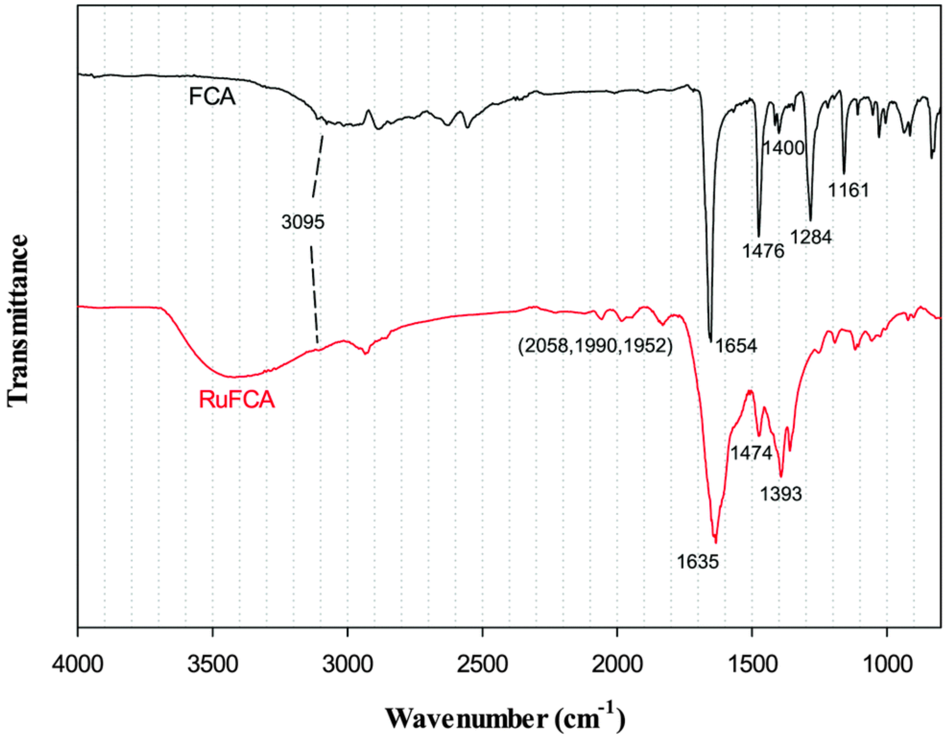

Figure 2.3 FTIR spectra of FCA monomers (black curve) and RuFCA nanoparticles (red curve).

Further structural insights were obtained from XPS measurements. Based on the XPS survey spectra in Figure 2.4 (A), the elements of C (Ru), O and Fe can be clearly identified in both FCA monomers and RuFCA nanoparticles (note that the binding energy of C1s and Ru3d electrons overlaps around 285 eV[27]). Yet clear discrepancy can be seen in high-resolution scans, as manifested in panels (B) to (D) (black curves are experimental data and color curves are deconvolution fits). For instance, in panel (B), deconvolution of the XPS profile of the FCA monomers revealed two peaks at 285.7 (blue curve) and 288.8 eV (yellow curve), which may be assigned to the ferrocenyl (C=C) and carboxyl (COO) C1s, respectively, and the ratio of the integrated peak areas is estimated to be 9.3:1, close to 10:1 expected from molecular structure. For the RuFCA nanoparticles, four peaks were resolved by deconvolution. Among these the one at 285.4 eV was most likely due to the ferrocenyl ring carbons (blue curve), the one at 287.6 eV to carbonyl carbon (magenta curve)-the ratio of their integrated peak areas is also close to 10:1, consistent with the bidentated binding of the FCA ligands onto the ruthenium nanoparticles surface (scheme 2.1). Additionally, the pairs at 281.5 (green curve) and 285.6 eV (yellow curve) may be assigned to Ru3d electrons. It should be noted that in a previous study with alkyne-stabilized ruthenium nanoparticles, the binding energy of the Ru3d electron was found to be markedly lower at 280.5 and 284.6 eV.[27] This may be ascribed to the difference of the chemical nature of the metal-ligand interfacial bonds: in the present study, the attachment of carboxyl moieties onto the ruthenium nanoparticle surface led to the formation of highly polarized Ru–O bonds where charge transfer from Ru to O likely occurred, whereas in alkyne-stabilized nanoparticles, the ruthenium-vinylidene bonds were mostly covalent in nature.[27] The (partial) interfacial charge transfer in Ru–O might also account for the small red-shift of both the carboxyl and ferrocenyl C1s electrons in RuFCA nanoparticles, as compared to those of FCA monomers.

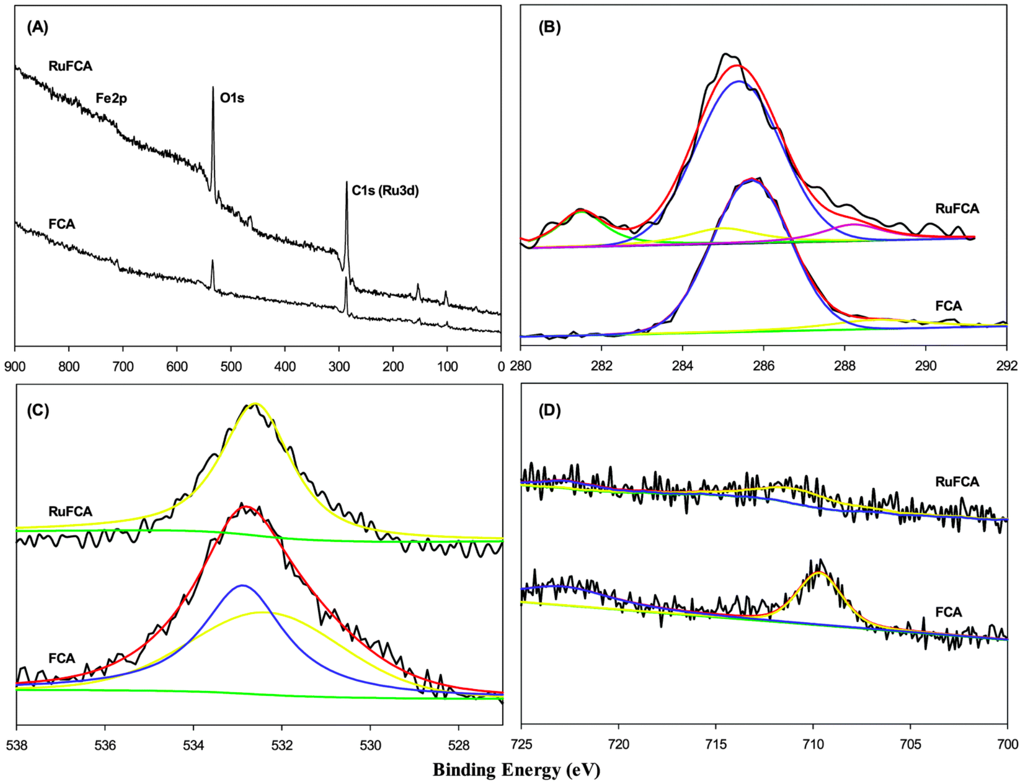

Figure 2.4 (A) XPS survey spectra of FCA monomers, and RuFCA nanoparticles. High-resolution scans of the (B) C1s (Ru3d), (C) O1s and (D) Fe2p electrons are also included, where black curves are the experimental data and color curves are the corresponding deconvolution fits.

Consistent results were observed in the measurements of the O1s and Fe2p electrons. As shown in panel (C), for the FCA monomers, two peaks were resolved in the O1s spectrum at 532.4 (yellow curve) and 532.9 eV (blue curve), corresponding to the C=O and C–O oxygen, respectively. In contrast, only one peak is needed to fit the data of RuFCA which is centered at 532.6 eV, suggesting that the bonding order involved was in the intermediate between C=O and C–O. This is consistent with the structural configuration where the carboxyl moieties were bound onto the ruthenium nanoparticle surface in a symmetrical bidentate fashion (Scheme 2.1). Similarly, for Fe2p electrons that are shown in panel (D), it can be seen that for the FCA monomers, the Fe(II)2p electrons are well-defined at 709.7 (yellow curve) and 722.8 eV (blue curve), whereas 710.8 (yellow curve) and 722.6 eV (blue curve) for the RuFCA nanoparticles. This observation is likely due to the strong polarization of the Ru–O interfacial bonds that diminishes the electron density of the iron centers in RuFCA, in good agreement with the NMR and FTIR results presented above.[28]

The impacts of surface functionalization by ferrocecarboxylate on the particle electronic properties were then examined by electrochemical measurements. Figure 2.5 shows the square wave voltammograms (SWV) of the FCA monomers and RuFCA nanoparticles in DMF with 0.1 M tetra-n-butylammonium perchlorate (TBAP) as the supporting electrolyte at a gold disk electrode. The FCA monomers (black curves) exhibited one pair of voltammetric peaks within the potential range of –0.20 to +0.30 V, with the formal potential (E^{o}') at +0.05 V vs Fc+/Fc. Similar voltammetric features can be seen with the RuFCA nanoparticles (red curves), with a rather comparable peak width at half maximum (103 mV and 110 mV for FCA and RuFCA, respectively); however, the formal potential was found to shift to +0.17 V, 120 mV more positive than that of FCA monomers. This is consistent with the above XPS results where the binding energy of the Fe2p electrons of the RuFCA nanoparticles was markedly higher than that of FCA monomers, again, because of the highly polarized Ru–O interfacial bonds that diminished the electron density of the iron centers (Scheme 2.1).

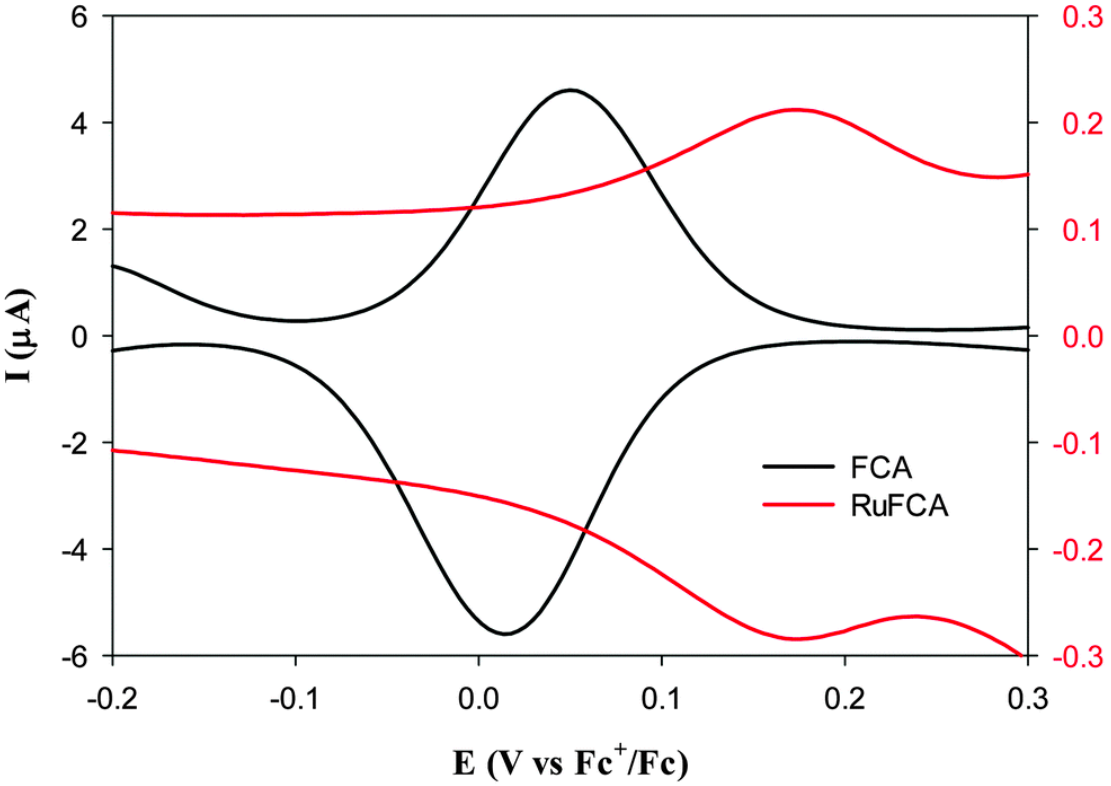

Figure 2.5 SWVs of FCA monomers and RuFCA nanoparticles acquired at a gold electrode in 0.1 M tetrabutylammonium perchlorate (TBAP) in DMF. Electrode surface area 0.70 mm2, FCA concentration 4.3 mM, RuFCA nanoparticle concentration 5 mg mL^{-1}, increment of potential 4 mV, amplitude 25 mV and frequency 15 Hz.

Interestingly, when the RuFCA nanoparticles underwent galvanic exchange reactions with $PdCl_4^{2-}$ followed by hydrothermal treatment at 200 °C for 4 h, the resulting nanoparticles exhibited drastically different voltammetric responses. This is to take advantage of the spontaneous galvanic exchange reaction of Ru(0) with Pd(II), as the redox potential of $PdCl_4^{2-}$ + 2e → Pd + 4Cl$^-$ (+0.591 V vs NHE) is more positive than that of $Ru^{2+} + 2e \rightarrow Ru$ (+0.455 V vs NHE),[29] where Pd was most likely deposited on the nanoparticle surface in the form of small clusters *(vide infra)*. It should be noted that Pd may serve as an effective catalyst for decarboxylation under hydrothermal conditions.[30] Therefore, the resulting RuPdFCA nanoparticles were subjected to hydrothermal treatment. It was antivipated that the ferrocenyl moieties would be directly bonded to the metal cores (Scheme 2.1) such that intraparticle charge delocalization occurred between the particle-bound ferrocenyl moieties. Indeed, as evidenced by the black curves in Figure 2.6, electrochemical measurements of these nanoparticles exhibited two pairs of voltammetric peaks within the potential range of −0.30 to +0.40 V (vs Fc+/Fc), with the formal potentials at +0.190 and −0.072 V, a behaviour consistent with intervalence charge transfer between the particle-bound ferrocenyl moieties.[8] Notably, the potential spacing (ΔV) of 260 mV between the two voltammetric peaks is markedly greater than those observed in the previous study (ca. 200 mV) where the ferrocenyl moieties were bound onto the ruthenium nanoparticles by ruthenium-carbene bonds,[8] but very comparable to those of conventional biferrocene derivatives.[31,32] This is consistent with Class II compounds as defined by Robin and Day.[33] In sharp contrast, for the nanoparticles prior to hydrothermal treatment (red curves), only a single pair of voltammetric peaks appear at +0.20 V, indicating the lack of effective electronic communication between the ferrocenyl functional groups on the nanoparticle surface because of insulation by the Ru−O linkages.

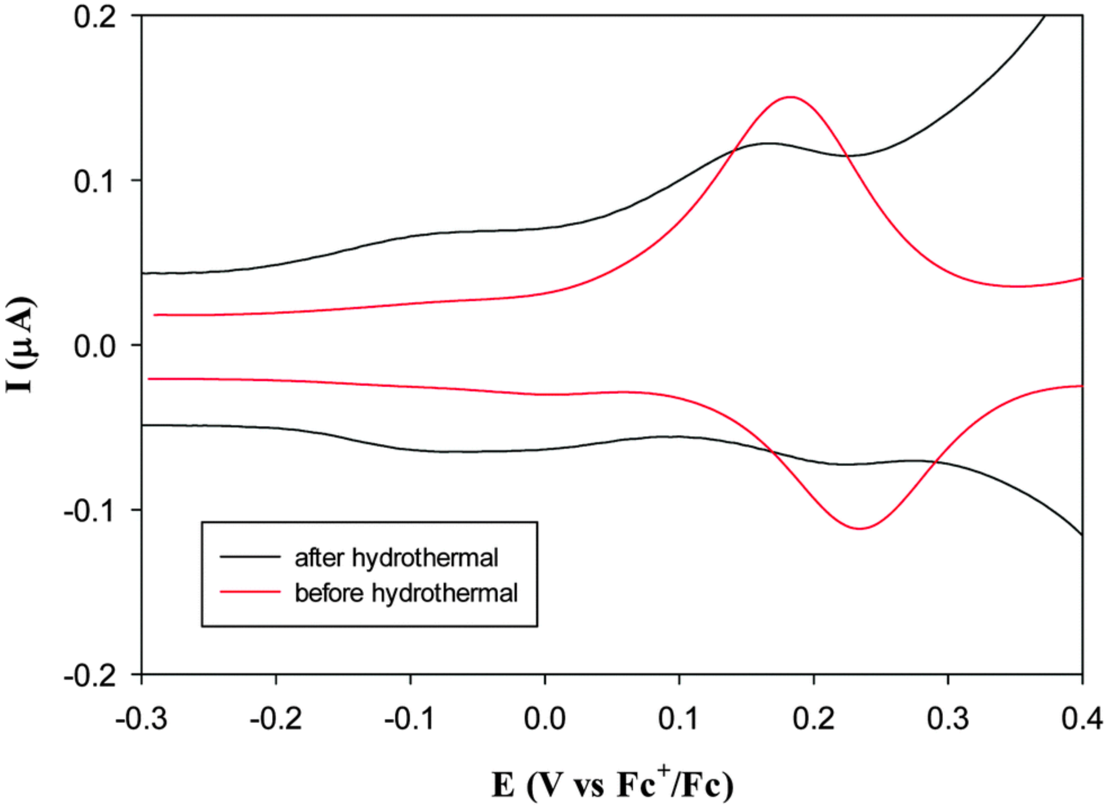

Figure 2.6 SWVs of RuFCA nanoparticles after galvanic exchange reactions with Pd(II) followed by hydrothermal treatment at 200 °C for 4 h. Other experimental conditions the same as those in Figure 2.5.

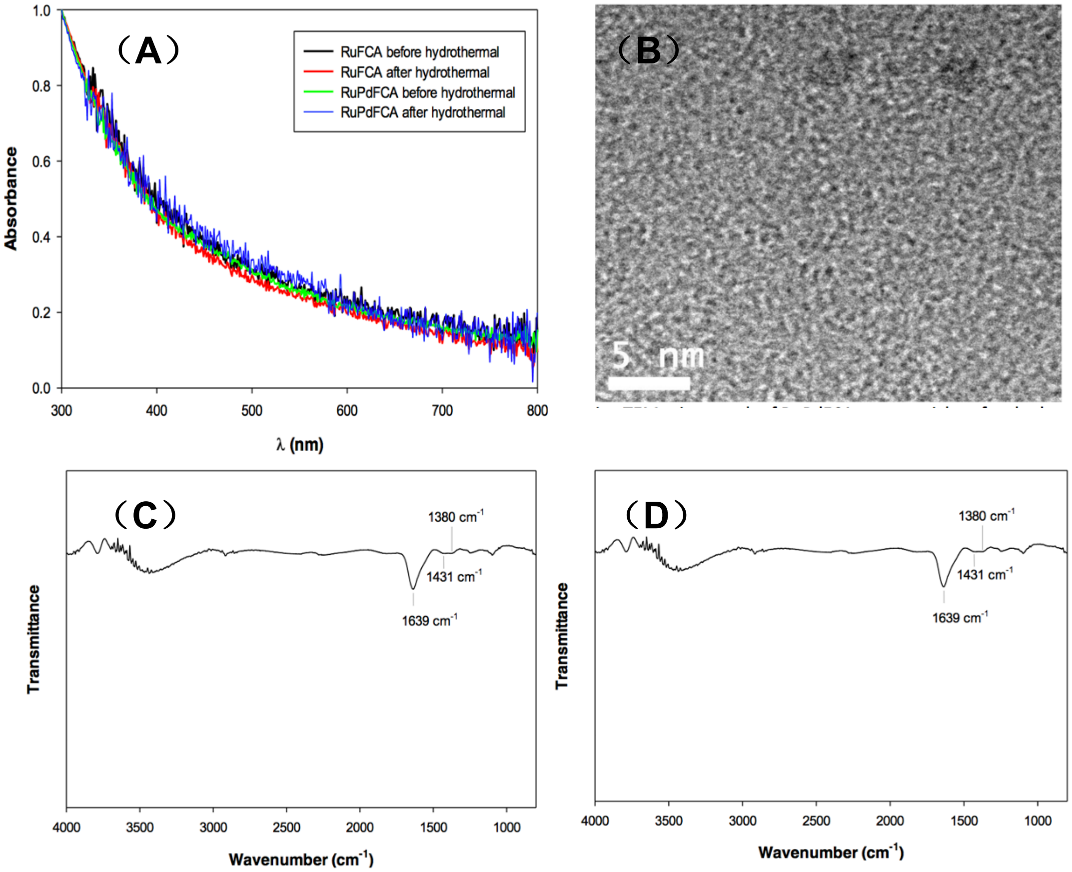

Figure 2.7 (A) UV-vis absorption spectra of RuFCA nanoparticles and RuPdFCA nanoparticles prepared by galvanic exchange reactions of RuFCA with Pd(II) before and after hydrothermal treatment. The data were normalized to the respective absorbance at 300 nm. The overlap of the spectra signifies little variation of the metal cores in the four nanoparticle samples. (B) Representative TEM micrograph of RuPdFCA nanoparticles after hydrothermal treatment. The size of the nanoparticles is around 2.5 nm. (C) FTIR spectrum of RuPdFCA nanoparticles after hydrothermal treatment. (D) ^{1}H NMR of hydrothermally treated RuPdFCA nanoparticles in deuterated DMF.

Furthermore, there are several aspects that warrant attention here. First, the RuPdFCA nanoparticles exhibited almost unchanged UV-vis absorption profiles before and after hydrothermal treatments, which were also consistent with that of the original RuFCA nanoparticles (Figure 2.7(A)), whereas TEM measurements showed that the size of the RuPdFCA nanoparticles increased to about 2.5nm after hydrothermal treatments (Figure 2.7(B)). Second, in FTIR measurements the C=O vibrational band at ca. 1639 cm^{-1} remained rather prominent with the hydrothermally treated RuPdFCA nanoparticles (Figure 2.7(C)), suggesting only partial decarboxylation of the FCA ligands on the nanoparticles. This is most likely due to the inhomogeneous distribution of the Pd (cluster) catalysts during galvanic exchange reactions and consistent with results from XPS measurements. From Figure 2.8, in the full survey spectrum of the RuPdFCA nanoparticles the Pd3d electrons can be identified at around 340 eV. However the signals are rather weak, signifying a low Pd concentration (most likely in the form of small clusters) in the nanoparticles; and the low signals renders it difficult to have a reliable quantitative assessment of the Pd loading. In addition, deconvolution of the C1s and Ru3d region yields four peaks at 281.1 eV (Ru3d5/2), 285.3 eV (Ru3d3/2), 285.2 eV (C1s C=C) and 287.5 eV (C=O C1s), Note that the ratio of the integrated peak areas between the C=C and C=O carbons was now 18.7:1, almost twice the values observed with the FCA monomers and RuFCA nanoparticles (vide ante). This suggests that close to 50% of the surface capping ligands were decarboxylated (Scheme 2.1), a result consistent with the voltammetric data presented in Fig. 2.6. The direct attachment of the ferrocenyl moieties onto the nanoparticle surface is also manifested in 1H NMR measurements with a single broad peak at around 4.3 ppm which may be assigned to the combined contributions of protons (b) and (c) whereas protons (a) were broadened into baseline (Figure 2.7(D)). Third, for the RuFCA nanoparticles subject to the same hydrothermal treatment but without galvanic exchange reactions with Pd(II), electrochemical measurements exhibited only one pair of voltammetric peaks, essentially the same as that of the original nanoparticles. This highlights the important role of Pd in the catalytic decarboxylation of the FCA ligands on the nanoparticle surface. Fourth, no stable palladium nanoparticles could be prepared with ferrocenecarboxylate as the capping ligands by the same thermolytic route. Thus, ligand decarboxylation on monometallic Pd nanoparticles could not be tested and compared.

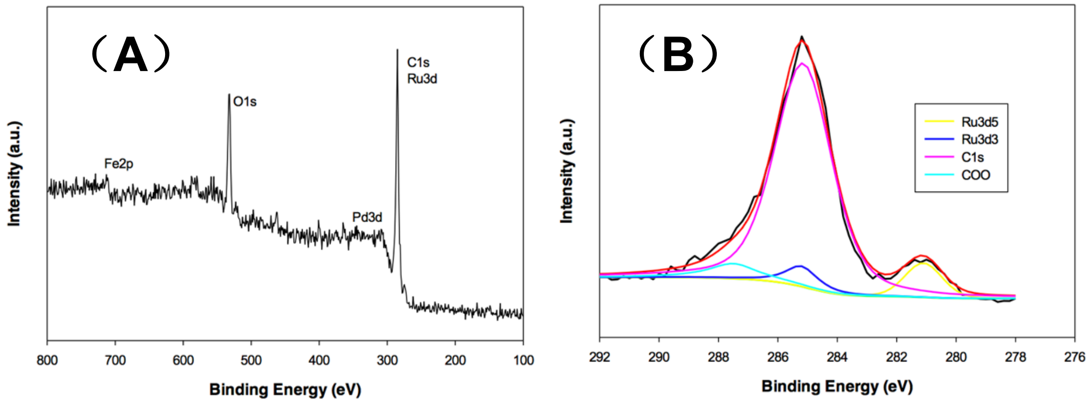

Figure 2.8 (A) XPS survey spectrum of RuPdFCA nanoparticles after hydrothermal treatment. (B) High-resolution scan of the C1s and Ru3d electrons where the black curve is the experimental data and color curves are the deconvolution fits.

2.4 Conclusion

In summary, stable ruthenium nanoparticles were prepared by using ferrocenecarboxylate as the protecting ligands through the formation of Ru–O bonds in a bidentate configuration, as evidenced in TEM, FTIR, ^{1}H NMR and XPS measurements. Notably, the formation of highly polarized Ru–O bonds led to a marked increase of the Fe2p binding energy as a result of the diminishment of the electron density of the ferrocenyl ring skeleton and iron center. Consistent results were obtained in electrochemical measurements where the formal potential of the particle-bound ferrocenyl moieties increased by ca. 120 mV as compared to that of the monomeric ligands. Importantly, the nanoparticles may undergo galvanic exchange reactions with Pd(II), leading to effective palladium-catalyzed decarboxylation of the ligands such that the ferrocenyl groups were now directly bonded to the metal surface. This was manifested in voltammetric measurements that suggested intervalence charge transfer between the ferrocenyl groups on the nanoparticle surface. The results presented herein may be of fundamental significance in the development of new protocols for the interfacial functionalization and engineering of nanoparticle materials

2.5 References

(1) Zehl, G.; Schmithals, G.; Hoell, A.; Haas, S.; Hartnig, C.; Dorbandt, I.; Bogdanoff, P.; Fiechter, S. On the structure of carbon-supported selenium-modified ruthenium nanoparticles as electrocatalysts for oxygen reduction in fuel cells. *Angew Chem Int Ed* **2007**, *46*, 7311-7314.

(2) Durap, F.; Zahmakiran, M.; Ozkar, S. Water soluble laurate-stabilized ruthenium(0) nanoclusters catalyst for hydrogen generation from the hydrolysis of ammonia-borane: High activity and long lifetime. *Int J Hydrogen Energ* **2009**, *34*, 7223-7230.

(3) Joo, S. H.; Park, J. Y.; Renzas, J. R.; Butcher, D. R.; Huang, W. Y.; Somorjai, G. A. Size Effect of Ruthenium Nanoparticles in Catalytic Carbon Monoxide Oxidation. *Nano Lett* **2010**, *10*, 2709-2713.

(4) Chen, S. W.; Templeton, A. C.; Murray, R. W. Monolayer-protected cluster growth dynamics. *Langmuir* **2000**, *16*, 3543-3548.

(5) Pan, C.; Pelzer, K.; Philippot, K.; Chaudret, B.; Dassenoy, F.; Lecante, P.; Casanove, M.-J. Ligand-Stabilized Ruthenium Nanoparticles: Synthesis, Organization, and Dynamics. *J. Am. Chem. Soc* **2001**, *123*, 7584-7593.

(6) Salas, G.; Santini, C. C.; Philippot, K.; Colliere, V.; Chaudret, B.; Fenet, B.; Fazzini, P. F. Influence of amines on the size control ofin situ synthesized ruthenium nanoparticles in imidazolium ionic liquids. *Dalton Trans.* **2011**, *40*, 4660-4668.

(7) Chen, W.; Davies, J. R.; Ghosh, D.; Tong, M. C.; Konopelski, J. P.; Chen, S. W. Carbene-functionalized ruthenium nanoparticles. *Chem Mater* **2006**, *18*, 5253-5259.

(8) Chen, W.; Chen, S. W.; Ding, F. Z.; Wang, H. B.; Brown, L. E.; Konopelski, J. P. Nanoparticle-mediated intervalence transfer. *J Am Chem Soc* **2008**, *130*, 12156-12162.

(9) Chen, W.; Zuckerman, N. B.; Kang, X. W.; Ghosh, D.; Konopelski, J. P.; Chen, S. W. Alkyne-Protected Ruthenium Nanoparticles. *J Phys Chem C* **2010**, *114*, 18146-18152.

(10) Kang, X. W.; Zuckerman, N. B.; Konopelski, J. P.; Chen, S. W. Alkyne-Functionalized Ruthenium Nanoparticles: Ruthenium-Vinylidene Bonds at the Metal-Ligand Interface. *J Am Chem Soc* **2012**, *134*, 1412-1415.

(11) Liu, K.; Kang, X. W.; Zhou, Z. Y.; Song, Y.; Lee, L. J.; Tian, D.; Chen, S. W. Platinum nanoparticles functionalized with acetylene derivatives: Electronic

conductivity and electrocatalytic activity in oxygen reduction. *J Electroanal Chem* **2013**, *688*, 143-150.

(12) Chen, W.; Zuckerman, N. B.; Konopelski, J. P.; Chen, S. W. Pyrene-Functionalized Ruthenium Nanoparticles as Effective Chemosensors for Nitroaromatic Derivatives. *Analy Chem* **2010**, *82*, 461-465.

(13) Kang, X. W.; Zuckerman, N. B.; Konopelski, J. P.; Chen, S. W. Alkyne-Stabilized Ruthenium Nanoparticles: Manipulation of Intraparticle Charge Delocalization by Nanoparticle Charge States. *Angew Chem Int Edn* **2010**, *49*, 9496-9499.

(14) Kang, X. W.; Chen, W.; Zuckerman, N. B.; Konopelski, J. P.; Chen, S. W. Intraparticle Charge Delocalization of Carbene-Functionalized Ruthenium Nanoparticles Manipulated by Selective Ion Binding. *Langmuir* **2011**, *27*, 12636-12641.

(15) Kang, X. W.; Li, X.; Hewitt, W. M.; Zuckerman, N. B.; Konopelski, J. P.; Chen, S. W. Manipulation of Intraparticle Charge Delocalization by Selective Complexation of Transition-Metal Ions with Histidine Moieties. *Anal Chem* **2012**, *84*, 2025-2030.

(16) Bruneau, C.; Dixneuf, P. H.: Ruthenium catalysts and fine chemistry; *Springer*: Berlin; New York, 2004.

(17) Chakroune, N.; Viau, G.; Ammar, S.; Poul, L.; Veautier, D.; Chehimi, M. M.; Mangeney, C.; Villain, F.; Fievet, F. Acetate- and thiol-capped monodisperse

ruthenium nanoparticles: XPS, XAS, and HRTEM studies. *Langmuir* **2005**, *21*, 6788-6796.

(18) Wu, N. Q.; Fu, L.; Su, M.; Aslam, M.; Wong, K. C.; Dravid, V. P. Interaction of fatty acid monolayers with cobalt nanoparticles. *Nano Lett* **2004**, *4*, 383-386.

(19) Guo, Y.; Chen, L. M.; Song, Y.; Hu, P. G.; Chen, S. W. Ruthenium Nanoparticles Stabilized by the Self-Assembly of Acetylene, Carboxylate, and Thiol Derivatives. *Sci Adv Mater* **2014**, *6*, 1060-1067.

(20) Leff, D. V.; Brandt, L.; Heath, J. R. Synthesis and characterization of hydrophobic, organically-soluble gold nanocrystals functionalized with primary amines. *Langmuir* **1996**, *12*, 4723-4730.

(21) Qiu, J. D.; Zhou, W. M.; Guo, J.; Wang, R.; Liang, R. P. Amperometric sensor based on ferrocene-modified multiwalled carbon nanotube nanocomposites as electron mediator for the determination of glucose. *Anal Biochem* **2009**, *385*, 264-269.

(22) Guan, L. H.; Shi, Z. J.; Li, M. X.; Gu, Z. N. Ferrocene-filled single-walled carbon nanotubes. *Carbon* **2005**, *43*, 2780-2785.

(23) Yong-Xiang, M.; Chun-Lin, M. Syntheses and properties of titanocene derivatives containing ferrocenecarboxylato ligands. *Chemistry Papers* **1989**, *43*, 761-770.

(24) Nichols, R. J.; Bewick, A. Spectroscopic Identification of the Adsorbed Intermediate in Hydrogen Evolution on Platinum. *J Electroanal Chem* **1988**, *243*, 445-453.

(25) Silantyev, G. A.; Filippov, O. A.; Tolstoy, P. M.; Belkova, N. V.; Epstein, L. M.; Weisz, K.; Shubina, E. S. Hydrogen Bonding and Proton Transfer to Ruthenium Hydride Complex CpRuH(dppe): Metal and Hydride Dichotomy. *Inorg Chem* **2013**, *52*, 1787-1797.

(26) Hashimoto, K.; Toukai, N. Decomposition of ammonia over a catalyst consisting of ruthenium metal and cerium oxides supported on Y-form zeolite. *J Mol Catal a-Chem* **2000**, *161*, 171-178.

(27) Kang, X. W.; Chen, S. W. Electronic conductivity of alkyne-capped ruthenium nanoparticles. *Nanoscale* **2012**, *4*, 4183-4189.

(28) Rohde, R. D.; Agnew, H. D.; Yeo, W. S.; Bailey, R. C.; Heath, J. R. A non-oxidative approach toward chemically and electrochemically functionalizing Si(111). *J Am Cheml Soc* **2006**, *128*, 9518-9525.

(29) Lide, D. R.: *CRC Handbook of Chemistry and Physics*; Electronic ed.; CRC Press: Boca Raton, FL, 2001.

(30) Matsubara, S.; Yokota, Y.; Oshima, K. Palladium-catalyzed decarboxylation and decarbonylation under hydrothermal conditions: Decarboxylative deuteration. *Organic Letters* **2004**, *6*, 2071-2073.

(31) Ribou, A. C.; Launay, J. P.; Sachtleben, M. L.; Li, H.; Spangler, C. W. Intervalence electron transfer in mixed valence diferrocenylpolyenes. Decay law of the metal-metal coupling with distance. *Inorg Chem* **1996**, *35*, 3735-3740.

(32) Levanda, C.; Bechgaard, K.; Cowan, D. O. Mixed-Valence Cations - Chemistry of Pi-Bridged Analogs of Biferrocene and Biferrocenylene. *J Org Chem* **1976**, *41*, 2700-2704.

(33) Robin, M. B.; Day, P. Mixed-valence chemistry - a survey and classification. *Adv Inorg Chem Radiochem* **1967**, *10*, 247 - 422.

Chapter 3

Chemical Reactivity of Naphthalenecarboxylate-Protected Ruthenium Nanoparticles: Intraparticle Charge Delocalization Derived from Interfacial Decarboxylation

Reproduced with permission from (Limei Chen, Peiguang Hu, Christopher P. Deming, Wei Li, Ligui Li, Shaowei Chen, Chemical Reactivity of Naphthalenecarboxylate-Protected Ruthenium Nanoparticles: Intraparticle Charge Delocalization Derived from Interfacial Decarboxylation, J. Phys. Chem. C, 2015, 119, 15449.) Copyright © 2015 American Chemical Society.

3.1 Introduction

Organically capped metal nanoparticles have been attracting extensive interest because the material properties may be readily controlled by the chemical nature of the metal cores and the organic protecting ligands as well as their interfacial bonding interactions.[1-5] In fact, the bonding linkages at the metal–ligand interface have been observed to impact the nanoparticle dimensions, morphology, and stability. Conversely metal nanoparticles also have influence on the ligand physical and chemical property, reactivity, and configuration.[4,6,7] Of these, ruthenium nanoparticles have been intensively studied due to its stability and affinity to many organic capping ligands, such as mercapto derivatives, alkylamines, diazo, acetylene, nitrene, and carboxylate moieties.[4,7-11] For instance, for ruthenium nanoparticles functionalized by acetylene derivatives, the formation of conjugated metal–ligand π-bonds leads to intraparticle charge delocalization, and hence, the nanoparticles exhibit new optical/electronic characteristics that are analogous to those of diacetylene derivatives.[11-13] These results highlight the significance of interfacial engineering in the manipulation of nanoparticle materials properties.

Conjugated metal–ligand interfacial bonds may also be produced by exploiting the unique interfacial reactivity of organic ligands on nanoparticle surfaces. For instance, we recently observed that alkene derivatives might self-assemble onto platinum nanoparticle surfaces, forming platinum–vinylidene or −acetylide bonds as a consequence of platinum-catalyzed dehydrogenation and transformation of the olefin groups.[14] In another study, ruthenium nanoparticles were protected by ferrocenecarboxylates, and galvanic exchange reactions with Pd(II) led to the deposition of a small amount of Pd onto the nanoparticle surface, which catalyzed the decarboxylation of the organic capping ligands under hydrothermal conditions, such that the electrochemical profiles of the resulting nanoparticles were similar to those of biferrocene derivatives.[15]

Results from these studies offer a new, effective protocol for the interfacial functionalization and engineering of transition-metal nanoparticles. In the present study, sodium naphthalenecarboxylate was used as a new protecting ligand to functionalize ruthenium nanoparticles where Ru–O bonds were formed at the metal–ligand interface; subsequent hydrothermal treatments at elevated temperatures effectively removed the carboxylate moieties even without the incorporation of Pd catalysts, such that the naphthalene (NA) moieties were now attached to the metal core by the Ru–C bonds.[7] Note that the bond strengths of Ru–O and Ru–C are actually quite similar, with the former[16] around 460 cm^{-1} and the latter[17] between 470 and 500 cm^{-1} as determined by Raman spectroscopic measurements. In fact, experimentally, it was found that hydrothermal treatment did not compromise the nanoparticle stability. Nevertheless, a drastic deviation was observed of the optical and electronic properties of the resulting nanoparticles as compared to those of the as-produced nanoparticles, as evidenced by a red shift of the photoluminescence (PL) emission and a negative shift of the formal potential of NA groups on the nanoparticle surface. This was ascribed to effective electronic coupling between the particle-bound NA groups where nanoparticle core electrons might spill into the organic capping ligands.

3.2 Experimental Section

Chemicals

Sodium hydroxide (NaOH, extra pure, Acros), sodium bicarbonate ($NaHCO_3$, +99%, Fisher Scientific), ruthenium chloride ($RuCl_3$, 35–40%Ru, Acros), naphthalene (NA, ultrapure, National Diagnostics), 2-naphthoic acid (NAA, 99%, Acros), and 1,2-propanediol (ACROS) were used as received. Solvents were purchased at their highest purity and used without further treatment. Water was supplied by a Barnstead Nanopure water system (18.3 MΩ·cm).

Synthesis of Naphthalenecarboxylate-Protected Ruthenium (RuCOONA) Nanoparticles

The synthetic procedure was similar to that used previously for the preparation of acetate-stabilized Ru particles.[15] In brief, 0.6 mmol of NAA, 0.6 mmol of NaOH, and 0.1 mmol of $RuCl_3$were dissolved in 1,2-propanediol (100 mL), and the solution was heated at 175 °C for 2 h under magnetic stirring. A rapid change of solution color was observed from dark orange to dark brown, signifying the formation of Ru nanoparticles. The solution was then cooled down to room temperature and purified by dialysis in Nanopure water for 3 days. Rotary evaporation of the resulting solution produced a solid, which was then rinsed with a copious amount of methanol to remove excessive free ligands and impurities, affording RuCOONA nanoparticles.

Decarboxylation of RuCOONA Nanoparticles

A calculated amount of the RuCOONA nanoparticles obtained above was then dispersed in a mixed solvent of DMF/water (7:1 v:v) and transferred into a polyphenyl (PPL)-lined autoclave. The sealed autoclave was put in an oven and heated at 250 °C for 14 h. A precipitate was produced at the bottom of the autoclave that was collected and rinsed with methanol five times. The purified nanoparticles were denoted as RuNA, which now became readily dispersible in common organic media, for example, CH_2Cl_2, *N*,*N*-dimethylformamide (DMF), and tetrahydrofuran (THF).

Characterizations

TEM measurements were carried out with a JEOL-F 200 kV field-emission analytical transmission electron microscope. In sample preparation, a drop of the particle solution in DMF was cast onto a 200 mesh holey carbon-coated copper grid. FTIR spectra were acquired with a PerkinElmer FTIR spectrometer (Spectrum One, spectral resolution 4 cm^{-1}), with the nanoparticles deposited onto a ZnSe disk. PL measurements were performed with a PTI fluorospectrometer. UV–vis absorption spectra were acquired with an ATI Unicam UV4 spectrometer using a 10 mm quartz cuvette at a resolution of 2 nm. X-ray photoelectron spectra (XPS) were recorded with a PHI 5400 XPS instrument equipped with an Al K_α source operated at 350 W and at 10^{-9} Torr. Silicon wafers were sputtered by argon ions to remove carbon from the background and used as substrates. The spectra were charge-referenced to the Si 2p peak (99.03 eV).

Electrochemistry

Electrochemical measurements were carried out with a CHI 440 electrochemical workstation. A polycrystalline gold disk electrode (sealed in glass tubing) was used as the working electrode (surface area 0.40 mm^2). A Ag/AgCl wire and a Pt coil were used as the (quasi)reference and counter electrodes, respectively. Prior to use, the gold electrode was polished with 0.05 μm alumina slurries and then cleansed by sonication in Nanopure water. Note that the potentials were all calibrated against the formal potential of ferrocene monomers (Fc^+/Fc) in the same electrolyte solution.

3.3 Results and Discussion

The size and morphology of the RuCOONA nanoparticles were first examined by TEM measurements. From the representative TEM image in Figure 3.1, one can see good dispersion of the nanoparticles with no obvious agglomeration, signifying effective stabilization of the nanoparticles by the naphthalenecarboxylate ligands due to the formation of Ru–O bonds at the metal–ligand interface.[7] High-resolution TEM measurements (lower inset) show well-defined lattice fringes of the nanoparticle cores at an interplanar spacing of 0.23 nm, in good agreement with that of Ru(100) crystalline planes.[12] Furthermore, the nanoparticle cores were found to fall in the narrow range of 0.8–2.2 nm in diameter, where the mean diameter was estimated to be 1.30 ± 0.27 nm, based on statistical analysis of over 120 nanoparticles, as depicted in the core size histogram (upper inset).

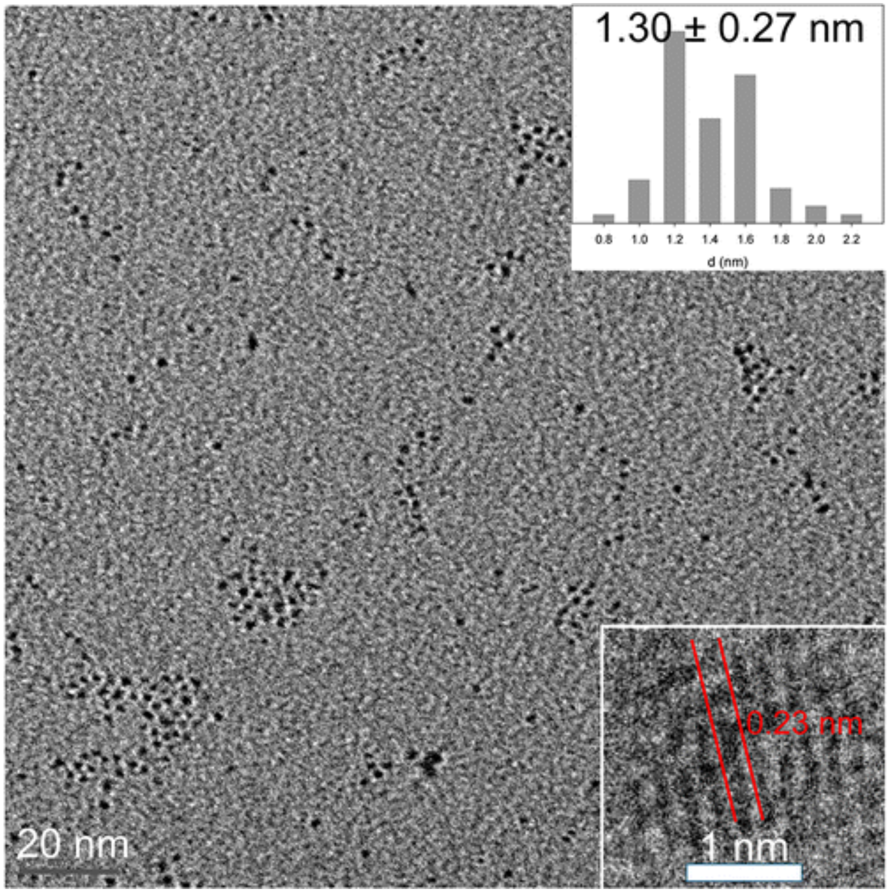

Figure 3.1 Representative TEM micrograph of RuCOONA nanoparticles. Scale bar = 20 nm. The lower inset is a high-resolution image of a nanoparticle (scale bar = 1 nm), and the upper inset is the particle core size histogram.

UV–vis absorption measurements were then carried out to examine the nanoparticle optical properties. For monomeric NAA, four characteristic absorption bands can be observed at 277, 290, 317, and 329 nm. The first pair might be assigned to the phenyl ring π → π* electronic transitions, whereas the last two are due to n → π* transitions of the carboxylic moiety (black curve, Figure 3.2(A)).[18] These spectral features remained well-defined even after the NAA monomers were subject to hydrothermal treatment at 250 °C (red curve) for 14 h, signifying the thermal stability of the molecules. In contrast, the RuCOONA nanoparticles (green curve) displayed a mostly exponential decay profile that is consistent with nanosized ruthenium colloids,[19] along with two small peaks at 270 and 291 nm for the π → π* transitions of phenyl ring electrons. The absence of the two n → π* transitions was due to the bidentate anchoring of the carboxylate groups onto the Ru nanoparticle surface where the two oxygen atoms of the COO^-group were now bonded to ruthenium symmetrically (Scheme 3.1).[7] After hydrothermal treatments, no obvious change of the absorption profile was observed with the resulting RuNA nanoparticles (yellow curve); note that TEM measurements showed an increase of the nanoparticle core size to ~2.5 nm after hydrothermal treatment (not shown).[15]

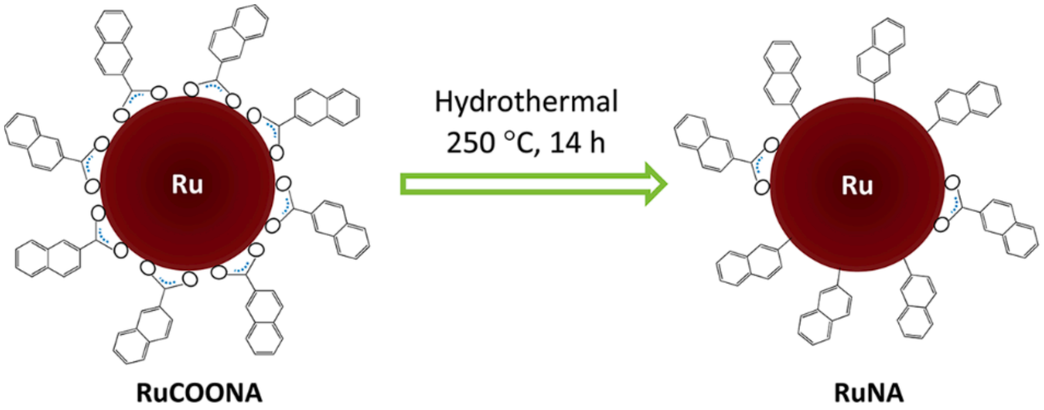

Scheme 3.1

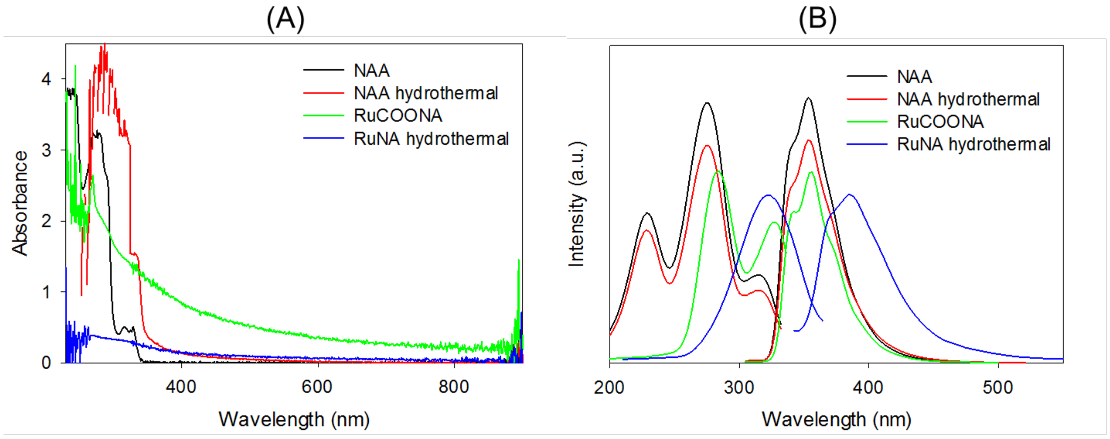

Figure 3.2 (A) UV–visible and (B) excitation and emission spectra of RuCOONA and RuNA nanoparticles in DMF. The spectra of NAA ligands before and after hydrothermal treatments are also included.

However, marked differences can be seen of the nanoparticle PL properties. As shown in Figure 3.2(B), one can see that the NAA ligands (black curves) exhibit three well-defined excitation peaks at 229, 275, and 317 nm, in good agreement with the UV–vis absorption peaks identified in panel (A), and when excited at 275 nm, a prominent emission peak can be seen at 353 nm (along with a shoulder at ca. 340 nm), characteristic of NA derivatives.[20] Note that after hydrothermal treatments, the overall PL profiles of the NAA monomers (red curves) were rather consistent, where two excitation peaks (281 and 325 nm) and a single emission peak at 354 nm were seen. Interestingly, for RuCOONA nanoparticles (green curves), similar PL profiles were also observed with two excitation peaks at 286 and 327 nm and an emission peak at 355 nm. These results suggest that (i) NAA ligands alone were structurally robust even after hydrothermal treatments, (ii) the ruthenium nanoparticles were readily functionalized with the NAA ligands, and (iii) the bonding interactions between the metal cores and carboxylate groups of the protecting ligands did not impact the luminescence property of the NA moieties. However, after the RuCOONA nanoparticles were hydrothermally treated, the resulting nanoparticles exhibited drastically different PL profiles (yellow curves). From panel (B), one can see only a single excitation peak at 322 nm and an emission one at 384 nm, analogous to those of 2,2′-binaphthalene derivatives.[21-23] Such an apparent red shift, in comparison with the results of the as-produced RuCOONA nanoparticles, may be ascribed to (partial) removal of the carboxylate groups of the NAA ligands and the direct bonding of the naphthenyl groups to the ruthenium metal nanoparticles (Scheme 3.1). This is in sharp contrast to our earlier study where interfacial decarboxylation did not occur with pure ruthenium nanoparticles but only when a trace amount of palladium was incorporated onto the ruthenium nanoparticle surface by galvanic exchange reactions.[15] Yet, one should note that in the previous study,[15] a Teflon-lined autoclave was used, which limited the hydrothermal temperature to 200 °C, whereas in the present study, a PPL-lined autoclave was used instead, which allowed an elevated temperature (250 °C) for hydrothermal treatment. These results suggest that whereas palladium is a well-known decarboxylation catalyst,[24] ruthenium nanoparticles are also able to catalyze the decarboxylation reaction of particle-bound carboxylate derivatives, but only at a higher temperature (Scheme 3.1).

Decarboxylation of the NAA ligands at the metal–ligand interface was further confirmed by FTIR measurements. Figure 3.3 shows the infrared spectra of NAA monomers, RuCOONA, and RuNA nanoparticles. One can see that the NAA monomers (black curve) displayed two vibrational bands at 1685 and 1311 cm^{-1}, which arose from the carboxylic C═O and C–O stretches, respectively, and the aromatic C–H vibrations appeared at 3055 cm^{-1}, along with the aromatic ring C═C stretches at 1472 and 1516 cm^{-1}.[25] Note that the weak bands between 1750 and 2000 cm^{-1}were most likely due to overtones of the aromatic ring vibrations. In contrast, for RuCOONA nanoparticles (red curve) where the ligands were bonded to the Ru nanoparticle surface, the two carboxylic vibrational bands at 1685 and 1311 cm^{-1} disappeared, and two new peaks emerged at 1639 and 1405 cm^{-1}. The latter are actually consistent with those of carboxylate groups, confirming that the NAA ligands were indeed bonded to the metal nanoparticle surface in a symmetrical bidentate fashion.[15,26] After hydrothermal treatment (green curve), the vibrational features of the carboxylate groups remained visible, but the intensity diminished drastically, suggesting (partial) decarboxylation of the NAA ligands at the metal–ligand interface. In addition, the aromatic C–H vibrations was found to red shift to below 3000 cm^{-1}. This might be ascribed to the direct bonding of the NA moieties onto the nanoparticle surface, leading to intraparticle charge delocalization between the particle-bound functional groups (Scheme 3.1).[6]

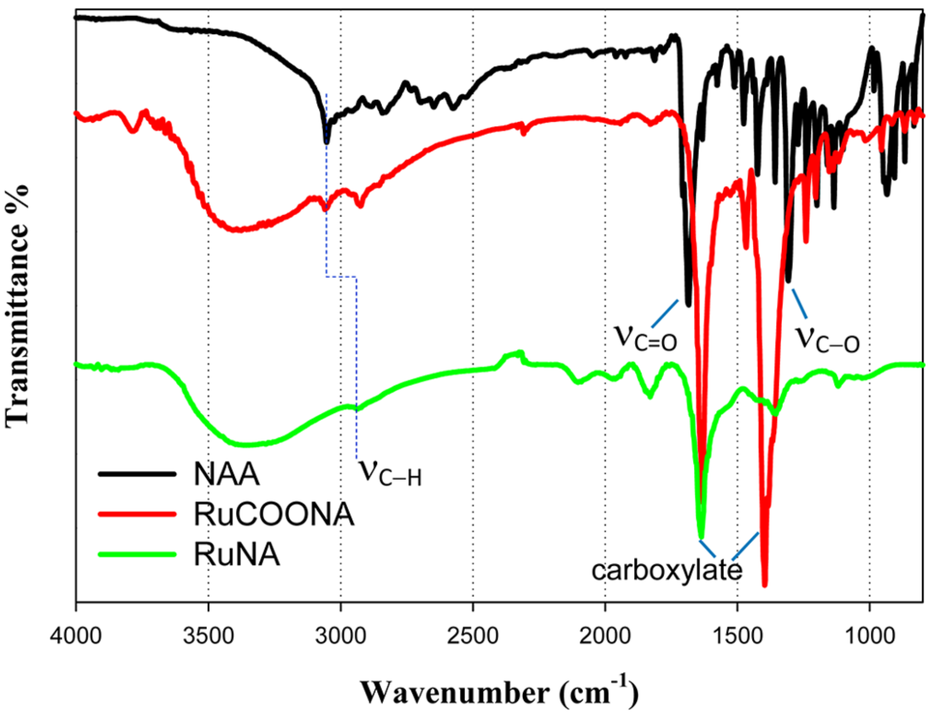

Figure 3.3 FTIR spectra of NAA monomers, RuCOONA, and RuNA nanoparticles.

Interfacial decarboxylation of the RuCOONA nanoparticles was also quantitatively determined by XPS measurements. From Figure 3.4, one can see that for the as-prepared RuCOONA nanoparticles (top black curve), two main peaks can be seen within the range of 278–292 eV. This includes the combined contributions of C 1s and Ru 3d electrons. In fact, deconvolution yields four peaks: the doublet at 280.6 (yellow curve) and 284.4 eV (blue curve) most likely arose from the $3d_{5/2}$ and $3d_{3/2}$ electrons of metallic ruthenium, respectively, whereas the peak at 285.3 eV (magenta curve) might be assigned to the C sp^2 electrons of the phenyl ring carbons and the one at 289.2 eV (aqua blue curve) to the carboxylate carbon. It should be noted that similar to ferrocenecarboxylate-stabilized ruthenium nanoparticles reported in the previous study,[15] the binding energies of the Ru 3d electrons were somewhat higher than those of alkyne-capped ruthenium nanoparticles because the Ru–O bonds were far more polar than the Ru–C ones.[4] In addition, on the basis of the integrated peak areas, the molar ratio of the COO^- carbon to the phenyl ring carbon was estimated to be 1:7.7, close to that (1:10) anticipated from the NAA molecular structure.

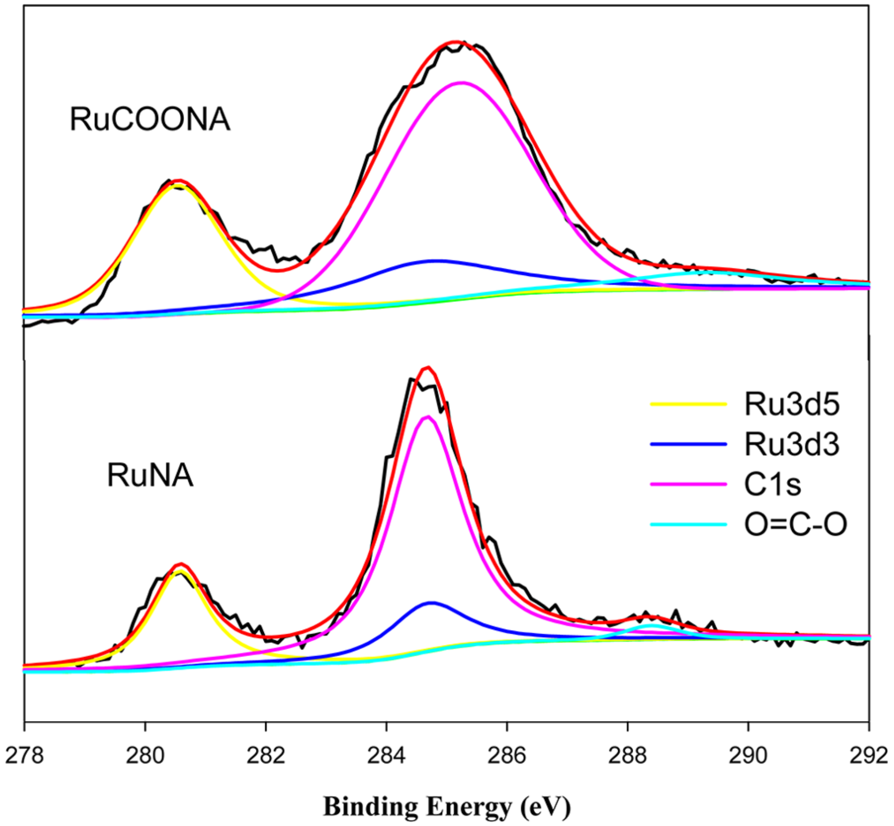

Figure 3.4 XPS spectra of the C 1s (Ru 3d) of RuCOONA nanoparticles (top) before and (bottom) after hydrothermal treatment (RuNA). Experimental data are denoted by the black curves, and deconvolution fits are represented by the color curves.

After hydrothermal treatment (RuNA, bottom black curve), the Ru 3d electrons exhibited virtually no change of binding energy at 280.6 (yellow curve) and 284.8 eV (blue curve), while C sp^2 red shifted somewhat to 284.8 eV (magenta curve) and carboxylate C to 288.4 eV (aqua blue curve). The latter might be ascribed to interfacial decarboxylation of the NAA ligands catalyzed by the ruthenium nanoparticles such that the NA moieties were now bonded directly to the nanoparticle surface. In fact, one can see that the concentration of carboxylate C decreased significantly as the molar ratio of COO^{-} to C sp^2 reduced to only 1:27. This indicates that ~63% of the NAA ligands were indeed decarboxylated by hydrothermal treatment (Scheme 3.1).

The impacts of interfacial decarboxylation of the NAA ligands on the particle electron-transfer properties were then investigated by voltammetric measurements. Figure 3.5 depicts the square wave voltammograms (SWV) of naphathalene, monomeric NAA, RuCOONA, and RuNA nanoparticles in DMF with 0.1 M tetra-*n*-butylammonium perchlorate (TBAP) as the supporting electrolyte. One can see a pair of voltammetric peaks for the RuCOONA nanoparticles (green curves), and the formal potential $E^{\circ\prime}$ was estimated to be −3.07 V (versus Fc^{+}/Fc), which is very consistent with the response observed with NAA monomers ($E^{\circ\prime} = -3.03$ V, red curves) and may be ascribed to the reversible reduction of NA moieties to monoanionic radicals.[27] This suggests that the bidentate bonding of the NAA ligands onto the ruthenium nanoparticles did not significantly impact the energy state of the NA moieties, most probably due to the nonconjugated Ru–O bonds on the nanoparticle surface. Yet, in comparison with the voltammetric response of monomaeric NA ($E^{\circ\prime} = -3.23$ V, black curve), one may see an anodic shift of $E^{\circ\prime}$ by about 160 mV, most likely due to the electron-withdrawing carboxyl moiety that facilitated electroreduction of the NA moieties. Interestingly, after hydrothermal treatment, the voltammetric peaks of the resulting RuNA nanoparticles (yellow curves) now appeared at $E^{\circ\prime} = -3.39$ V, more than 300 mV more negative than that of RuCOONA and even 160 mV more negative than that of monomeric NA. This may be accounted for by the direct bonding of the NA moieties to the ruthenium nanoparticle surface because of interfacial decarboxylation of the NAA ligands. Thanks to the low resistance of the Ru–C bonds,[28] metal core electrons might spill into the organic capping ligands, which would render the electroreduction of the particle-bound NA moieties to take place at a more negative potential position.[29,30] This is consistent with results from the PL measurements (Figure 3.2), which suggests that the particle-bound functional moieties behave analogously to the dimeric counterparts.

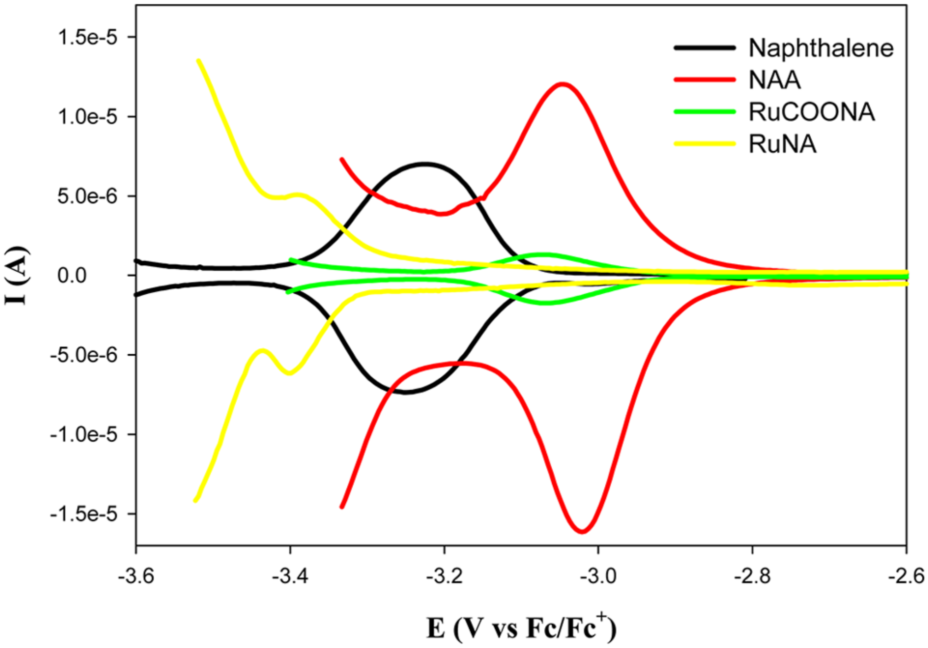

Figure 3.5 SWVs of NA, monomeric NAA, and RuCOONA metal nanoparticles before and after hydrothermal treatment in DMF with 0.1 M TBAP. The surface area of the Au disk electrode is 0.40 mm^2. The NA concentration is 2 mg/mL, NAA is 3 mg/mL, RuCOONA is 3 mg/mL, and RuNA is 2 mg/mL. In SWV measurements, the frequency was 15 Hz, the potential increment was 4 mV, and the amplitude was 25 mV.

3.4 Conclusion

In this study, ruthenium nanoparticles were functionalized with naphthalenecarboxylate ligands, forming Ru–O interfacial bonds in a symmetrical bidentate fashion. Hydrothermal treatment at controlled temperatures resulted in effective decarboxylation of the surface capping ligands, as evidenced in spectroscopic and electrochemical measurements. Notably, interfacial decarboxylation led to direct bonding of the NA group onto the nanoparticle metal cores. Thanks to the low metal–ligand interfacial resistance, intraparticle charge delocalization occurred between the particle-bound NA moieties, leading to the appearance of new optical and electronic properties that were analogous to those of the dimeric counterparts. These results may offer new fundamental insights into the interfacial functionalization and engineering of transition-metal nanoparticles.

3.5 References

(1) Nath, S.; Jana, S.; Pradhan, M.; Pal, T. Ligand-stabilized metal nanoparticles in organic solvent. *J Colloid Interf Sci* **2010**, *341*, 333-352.

(2) Pan, C.; Pelzer, K.; Philippot, K.; Chaudret, B.; Dassenoy, F.; Lecante, P.; Casanove, M. J. Ligand-stabilized ruthenium nanoparticles: Synthesis, organization, and dynamics. *J Am Chem Soc* **2001**, *123*, 7584-7593.

(3) Lara, P.; Rivada-Wheelaghan, O.; Conejero, S.; Poteau, R.; Philippot, K.; Chaudret, B. Ruthenium Nanoparticles Stabilized by N-Heterocyclic Carbenes:

Ligand Location and Influence on Reactivity. *Angew Chem Int Edit* **2011**, *50*, 12080-12084.

(4) Kang, X. W.; Chen, S. W. Electronic conductivity of alkyne-capped ruthenium nanoparticles. *Nanoscale* **2012**, *4*, 4183-4189.

(5) Viau, G.; Brayner, R.; Poul, L.; Chakroune, N.; Lacaze, E.; Fievet-Vincent, F.; Fievet, F. Ruthenium nanoparticles: Size, shape, and self-assemblies. *Chem Mater* **2003**, *15*, 486-494.

(6) Hu, P. G.; Song, Y.; Rojas-Andrade, M. D.; Chen, S. W. Platinum Nanoparticles Functionalized with Ethynylphenylboronic Acid Derivatives: Selective Manipulation of Nanoparticle Photoluminescence by Fluoride Ions. *Langmuir* **2014**, *30*, 5224-5229.

(7) Guo, Y.; Chen, L. M.; Song, Y.; Hu, P. G.; Chen, S. W. Ruthenium Nanoparticles Stabilized by the Self-Assembly of Acetylene, Carboxylate, and Thiol Derivatives. *Sci Adv Mater* **2014**, *6*, 1060-1067.

(8) Deming, C. P.; Kang, X. W.; Liu, K.; Chen, S. W. Nitrene-functionalized ruthenium nanoparticles: Selective manipulation of nanoparticle electronic conductivity by vinyl derivatives. *Sensor Actuat B-Chem* **2014**, *194*, 319-324.

(9) Chen, W.; Zuckerman, N. B.; Lewis, J. W.; Konopelski, J. P.; Chen, S. W. Pyrene-Functionalized Ruthenium Nanoparticles: Novel Fluorescence

Characteristics from Intraparticle Extended Conjugation. *J Phys Chem C* **2009**, *113*, 16988-16995.

(10) Chen, W.; Ghosh, D.; Sun, J.; Tong, M. C.; Deng, F. J.; Chen, S. W. Dithiocarbamate-protected ruthenium nanoparticles: Synthesis, spectroscopy, electrochemistry and STM studies. *Electrochim Acta* **2007**, *53*, 1150-1156.

(11) Chen, W.; Chen, S. W.; Ding, F. Z.; Wang, H. B.; Brown, L. E.; Konopelski, J. P. Nanoparticle-mediated intervalence transfer. *J Am Chem Soc* **2008**, *130*, 12156-12162.

(12) Chen, W.; Zuckerman, N. B.; Kang, X. W.; Ghosh, D.; Konopelski, J. P.; Chen, S. W. Alkyne-Protected Ruthenium Nanoparticles. *J Phys Chem C* **2010**, *114*, 18146-18152.

(13) Kang, X. W.; Zuckerman, N. B.; Konopelski, J. P.; Chen, S. W. Alkyne-Functionalized Ruthenium Nanoparticles: Ruthenium-Vinylidene Bonds at the Metal-Ligand Interface. *J Am Chem Soc* **2012**, *134*, 1412-1415.

(14) Hu, P. G.; Duchesne, P. N.; Song, Y.; Zhang, P.; Chen, S. W. Self-Assembly and Chemical Reactivity of Alkenes on Platinum Nanoparticles. *Langmuir* **2015**, *31*, 522-528.

(15) Chen, L. M.; Song, Y.; Hu, P. G.; Deming, C. P.; Guo, Y.; Chen, S. W. Interfacial reactivity of ruthenium nanoparticles protected by ferrocenecarboxylates. *Phys Chem Chem Phys* **2014**, *16*, 18736-18742.

(16) Yukawa, Y.; Handa, M.; Hoshino, Y. Resonance Raman-Spectra of Tris(Acetylacetonato)Iron(Iii) and Ruthenium(Iii) Complexes and Their Solvent Effect. *J Solution Chem* **1995**, *24*, 19-24.

(17) Toyohara, K.; Tsuge, K.; Tanaka, K. Comparison of Ru-C Bond Characters Involved in Successive Reduction of Ru-Co2 to Ru-Ch2oh. *Organometallics* **1995**, *14*, 5099-5103.

(18) Myhre, C. E. L.; Nielsen, C. J. Optical properties in the UV and visible spectral region of organic acids relevant to tropospheric aerosols. *Atmos Chem Phys* **2004**, *4*, 1759-1769.

(19) Creighton, J. A.; Eadon, D. G. Ultraviolet Visible Absorption-Spectra of the Colloidal Metallic Elements. *J Chem Soc Faraday T* **1991**, *87*, 3881-3891.

(20) Maeda, H.; Maeda, T.; Mizuno, K. Absorption and Fluorescence Spectroscopic Properties of 1- and 1,4-Silyl-Substituted Naphthalene Derivatives. *Molecules* **2012**, *17*, 5108-5125.

(21) Kondo, S.; Sonoda, H.; Katsu, T.; Unno, M. Improvement of solubility of 2,2 '-binaphthalene derivatives bearing urea groups as anion receptors and their application to a chloride selective electrode. *Sensor Actuat B-Chem* **2011**, *160*, 684-690.

(22) Parker, K. S.; Townshend, A.; Bale, S. J. Determination of the Enantiomeric Composition of 1-Phenylethylamine Based on Its Quenching of the Fluorescence of 2,2'-Dihydroxy-1,1'-Binaphthalene. *Anal Proc* **1995**, *32*, 329-332.

(23) Irie, M.; Yorozu, T.; Hayashi, K. Steric Effect on Fluorescence Quenching of 1,1'-Binaphthyl by Chiral Amines. *J Am Chem Soc* **1978**, *100*, 2236-2237.

(24) Matsubara, S.; Yokota, Y.; Oshima, K. Palladium-catalyzed decarboxylation and decarbonylation under hydrothermal conditions: Decarboxylative deuteration. *Org Lett* **2004**, *6*, 2071-2073.

(25) Silverstein, R. M.; Bassler, G. C.; Morrill, T. C.: *Spectrometric identification of organic compounds*; 5th ed.; Wiley: New York, 1991.

(26) Wu, N. Q.; Fu, L.; Su, M.; Aslam, M.; Wong, K. C.; Dravid, V. P. Interaction of fatty acid monolayers with cobalt nanoparticles. *Nano Lett* **2004**, *4*, 383-386.

(27) Meerholz, K.; Heinze, J. Multiple Reversible Electrochemical Reduction of Aromatic-Hydrocarbons in Liquid Alkylamines. *J Am Chem Soc* **1989**, *111*, 2325-2326.

(28) Ghosh, D.; Chen, S. W. Solid-state electronic conductivity of ruthenium nanoparticles passivated by metal-carbon covalent bonds. *Chem Phys Lett* **2008**, *465*, 115-119.

(29) Fernando, R.; Etheridge, F.; Muller, E.; Sauve, G. Tuning the optical and electrochemical properties of core-substituted naphthalenediimides with styryl imide substituent. *New J Chem* **2015**, *39*, 2506-2514.

(30) Zweig, A.; Maurer, A. H.; Roberts, B. G. Oxidation Reduction and Electrochemiluminescence of Donor-Substituted Polycyclic Aromatic Hydrocarbons. *J Org Chem* **1967**, *32*, 1322-&.

Chapter 4

Ruthenium Nanoparticles Stabilized by the Self-Assembly of Acetylene, Carboxylate, and Thiol

Reproduced with permission from (Yan Guo†, Limei Chen†, Yang Song, Peiguang Hu, and Shaowei Chen, "Ruthenium Nanoparticles Stabilized by the Self-Assembly of Acetylene, Carboxylate, and Thiol", Sci. Adv. Mater., 2014, 6, 1060. (†equal contribution)) Copyright © 2014 by American Scientific Publishers.

4.1 Introduction

Organically capped transition-metal nanoparticles represent a unique class of functional nanomaterials that exhibit interesting chemical and physical properties and thus have been attracting a great deal of attention in diverse applications such as nanoelectronics, catalysis, and sensing.[1-3] Because of their nanocomposite nature, the material properties of these nanoparticles may be readily manipulated by the chemical nature of the metal cores, the structures of the surface organic ligands, as well as the metal-ligand interfacial bonding interactions.[4,5] For instance, ruthenium nanoparticles display unique and novel optical, electronic and chemical properties when functionalized with different organic ligands forming various metal-ligand interfacial bonds.[6,7] This has been exemplified in the studies of the temperature dependence of electronic conductivity of aliphatic ligands-capped Ru nanoparticles,[8] and the catalytic activity of ionic liquid-stabilized Ru nanoparticles.[9] In these studies, it is recognized that the interfacial bonding interactions may impact the electron transfer pathways and kinetics within and between the nanoparticles. This is akin to the observations of different electron transport pathways in linear and cyclic conjugated molecules,[10,11] as well as discrepancy of electronic conductivity through a same molecular skeleton but at different valence states caused by oxidization and reduction.[12]

In these studies, scanning tunneling microscopy and spectroscopy (STM/S) is an effective tool to unravel the electron transfer characteristics of individual nanoparticles of selected sizes and structures. In STS measurements, both Coulomb blockade and Coulomb staircase phenomena may be observed. Coulomb blockade is an electronic phenomenon where the tunneling current is suppressed because the electron does not have sufficient energy to tunnel through the junctions. The origin of this phenomenon lies in the fundamental quantization of the electronic charge, and it occurs in systems with small quantum charge fluctuations. As a result, the redistribution of junction charges necessarily associated with a current flow can be made only in quantized units of e (where e is the elementary charge unit). The corresponding quantized electrostatic charging energy, which for small nanoscale junctions can be large as compared to other relevant energies related to temperature and bias voltage, tends to block the current flow.[13,14] Coulomb staircase is a step-like electron-transfer feature when two pre-requisites are satisfied.[15,16] First, to observe single electron tunneling of an isolated metallic nanoparticle of capacitance (C), the energy associated with transferring one electron ($E_c = e^2/2C$) must exceed thermal kinetic energy (k_BT). At room temperature ($k_BT = 26$ meV), this dictates that the metal nanoparticle size must be below 10 nm so that the capacitance is on the order of 10^{-18} F. Second, the electrical contacts to the particles must have tunneling resistance larger than the quantum resistance ($h/4e^2 \sim 6.5$ kΩ), in order to suppress quantum fluctuations of the electronic charge.

The features of Coulomb staircase and Coulomb blockade are critically dependent on the structure and conformation of the nanoparticles sandwiched between two conductors (for instance, an STM tip and an electrode substrate forming a double-barrier tunneling junction). The electron-transfer properties through the junction have been found to be influenced by the nanoparticle core sizes[17-19] and chemical environments.[20] Yet, to our knowledge, reports have been scarce in the study of the impacts of metal-organic interfacial contacts on nanoparticle Coulomb staircase.

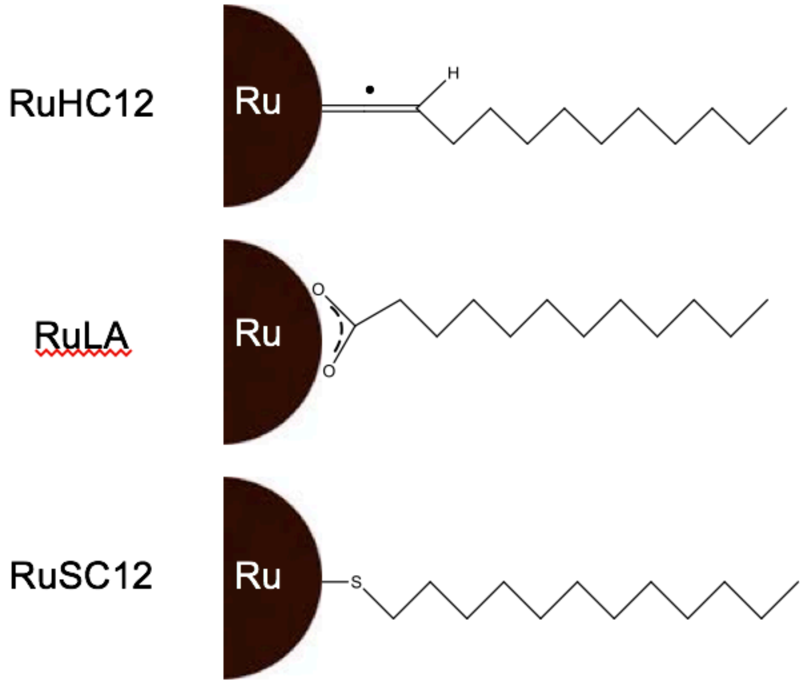

Scheme 4.1

Therefore, in this study, we investigated the electron transfer behaviors of ruthenium nanoparticles capped with three different kinds of organic ligands, 1-dodecyne, sodium laurate and 1-dodecanethiol, forming ruthenium vinylidene (Ru=C=CH−), ruthenium−oxygen (Ru−O) and ruthenium−thiolate (Ru−S) interfacial bonds (Scheme 1), respectively. XPS measurements suggested increasing polarization of the order of Ru=C=CH− < Ru−S < Ru−O. STS studies showed apparent Coulomb staircase and Coulomb blockade features that varied with the size and metal−ligand interfacial bonds. The results indicate that metal-ligand interfacial contact is indeed an important parameter in the design and manipulation of nanoparticle charge transfer properties.

4.2. Experimental Section

Materials

Ruthenium chloride ($RuCl_3$, 99+%, ACROS), 1-dodecyne (ACROS, 98%), 1-dodecanethiol (Aldrich, 98+%), lauric acid (ACROS, 99.5+%), sodium hydroxide (NaOH, extra pure), 1,2-propanediol (ACROS), and sodium acetate (NaOAc, MC&B) were used as received. All solvents were obtained from typical commercial sources and used without further treatment. Water was supplied by a Barnstead Nanopure water system (18.3 MΩ cm).

Dodecyne- and dodecanethiol-capped Ru nanoparticles were synthesized by following a procedure detailed previously.[4,21] In brief, 0.28 mmol of $RuCl_3$ and 2 mmol of NaOAc were dissolved in 200 mL of 1,2-propanediol. The mixed solution was heated to 165 °C for 1 h under vigorous stirring, where the solution turned dark brown signifying the formation of nanometer-sized ruthenium colloids. The solution was then removed from the heating mantle and cooled to room temperature. A calculated amount of 1-dodecyne or 1-dodecanethiol in toluene was added to the solution under rigorous stirring. The toluene phase was found to exhibit a dark brown color whereas the alcohol phase became colorless, indicating the effective transfer of the nanoparticles into the toluene phase because of the self-assembly of the dodecyne or dodecanethiol ligands onto the ruthenium surface. The toluene phase was then collected, dried under rotary evaporation and rinsed with a copious amount of methanol to remove excessive ligands, affording purified nanoparticles that were denoted as RuHC12 and RuSC12, respectively.

Laurate-stabilized ruthenium (RuLA) nanoparticles were prepared in a similar fashion except that sodium acetate was substituted by an equal amount of sodium laurate in the thermolytic reduction of $RuCl_3$ in 1,2-propanediol (sodium laurate was synthesized a prior by mixing a stoichiometric amount of NaOH with lauric acid in methanol). The resulting nanoparticles were then dialyzed in a dialysis bag (cutoff molecular weight 2000 Da) for 3 days. The collected solids were found to be soluble in apolar organic solvents such as CH_2Cl_2, $CHCl_3$, and THF but not in water or alcohols.

Characterizations

Proton NMR measurements were carried out with a Varian Unity 500 MHz NMR spectrometer using concentrated solutions of the nanoparticles in CD_2Cl_2. The absence of any sharp spectral features indicated that the nanoparticles were free of excessive ligands. FTIR measurements were carried out with a Perkin-Elmer FTIR spectrometer (Spectrum One, spectral resolution 4 cm^{-1}) where samples were prepared by casting the ruthenium nanoparticles onto a ZnSe disk. Thermogravimetric analysis (TGA) was performed with a Perkin-Elmer Pyris 1 thermogravimetric analyzer under a constant flow of ultrahigh-purity N_2 (99.999%) at a heating rate of 10 °C/min. Transmission electron microscopic (TEM) measurements were carried out whereby samples were prepared by casting a drop of the particle solution in dichloromethane onto a 200-mesh carbon-coated copper grid; and at least three images were acquired for each sample with a JEOL 1200 EX transmission electron microscope (TEM) operated at 80 kV. The particle core size was estimated by using ImageJ® analysis of the TEM micrographs. X-ray photoelectron spectra (XPS) were recorded with a PHI 5400 XPS instrument equipped with an Al Kα source operated at 350 W and at 10^{-9} torr.

STM/STS measurement

STM topographs and I-V curves of the nanoparticles of selected sizes were acquired with a Molecular Imaging PicoLE scanning probe microscope. Au thin films supported on mica were supplied from Molecular Imaging Inc. Prior to use, the Au substrates were subject to UV-ozone (Model 42, Jelight Co.) cleaning for 15 min and then immersed into an ethanolic solution of 1 mM n-butanethiol to form a self-assembled monolayer that helped immobilize nanoparticles deposited onto the surface. The particles were dissolved in dichloromethane and drop-cast onto the Au substrate using a Hamilton microliter syringe and dried under a gentle stream of nitrogen. A mechanically cut Pt/Ir tip was used in the STM measurements. A high impedance of 75 M (bias 1.5 V and set point 0.02 nA) was used to prevent tip damaged or capture of the metal particles. All STM topographic images were recorded in constant current mode. *I-V* data were collected in the spectroscopy mode where the feedback loop was turned off. Initially, isolated nanoparticles were located by scanning in a large area (typically 400 nm × 400 nm), and stable, nondrifting images were then acquired by zooming into smaller areas. The nanoparticle dimensions were estimated by the cross section in STM measurements. At least two hundred I-V data points were collected in a typical voltage sweep of ±2 V. All *I-V* curves were the averaged results of five measurements.

4.3 Results and Discussion

In the thermolytic reduction of $RuCl_3$ in 1,2-propanediol, the resulting ruthenium nanoparticles were stabilized by carboxylate derivatives added in the solution.[22] Figure 4.1 depicts two representative TEM micrographs of the nanoparticles synthesized in the presence of (A) sodium acetate and (B) sodium laurate. Statistical analysis based on more than 300 nanoparticles showed that the average diameters of the nanoparticles were close, at 1.90 ± 0.34 nm and 2.60 ± 0.20 nm, respectively. In the former, with the addition of 1-dodecyne or 1-dodecanethiol, they replaced the acetate ligands and adsorbed onto the ruthenium nanoparticle surface, forming RuHC12 and RuSC12 nanoparticles. Thus, in comparison with the RuLA counterparts, the organic capping ligands were of similar chainlength but there was clear discrepancy of the metal-ligand interfacial bonds (Scheme 1). This provides a simple structural framework within which the nanoparticle dielectric properties may be evaluated and compared, as manifested below.

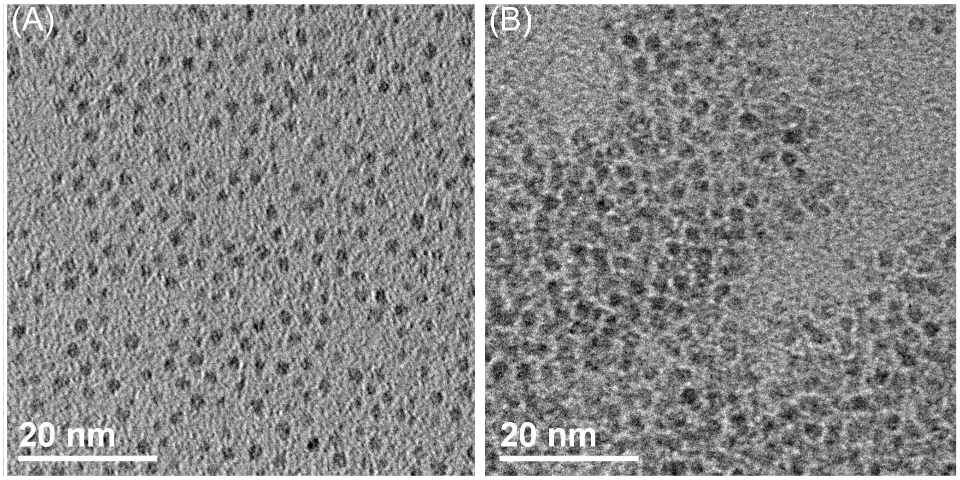

Figure 4.1 Representative TEM micrographs of ruthenium nanoparticles prepared by thermolysis of $RuCl_3$ in the presence of (A) sodium acetate and (B) sodium laurate. Scale bars are both 20 nm.

Consistent results were obtained in STM topographic measurements. Figure 4.2 shows a representative STM topograph of (A) RuHC12, (B) RuLA, and (C) RuSC12 nanoparticles. One can see that all particles exhibited a roughly circular shape with the topographic diameters largely in the range of 4 to 6 nm. Note that in STM measurements, the size of the nanoparticles includes the metal cores plus two fully-extended organic capping ligands. As the chainlengths of the capping ligands are 1.36 nm for 1-dodeyne, 1.51 nm for laurate, and 1.55 nm for 1-dodecanethiol (estimated by Hyperchem®), the corresponding core diameters can be found to range from 1 to 3 nm, in good agreement with the TEM results.

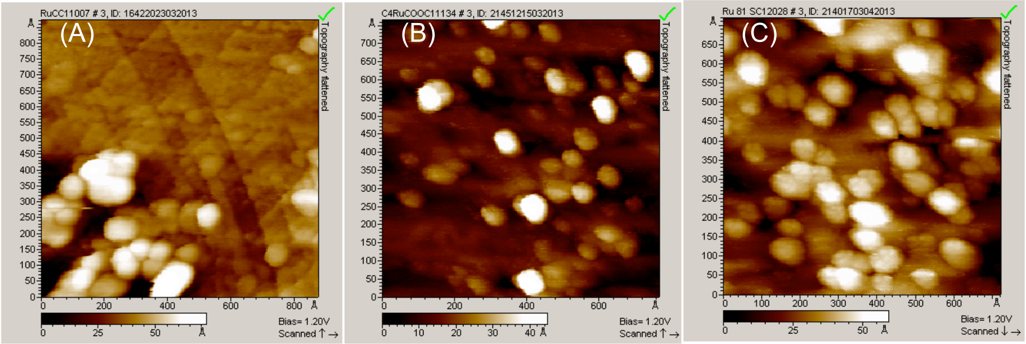

Figure 4.2 STM topographies of (A) RuHC12, (B) RuLA, and (C) RuSC12 nanoparticles.

The structures of the organic capping ligands were then examined by FTIR measurements. Figure 4.3 depicts the infrared spectra of the RuHC12, RuLA and RuSC12 nanoparticles, along with those of the corresponding monomeric ligands. It can be seen that for all samples, the methyl and methylene vibrational stretches are very consistent and well-defined at 2957, 2924, and 2854 cm^{-1}. However, there are several spectral features that are specific to the organic capping ligands and warrant special attention here. For instance, for the 1-dodecyne ligands the ≡C–H stretch can be clearly identified at 3314 cm^{-1} and the C≡C stretch at 2119 cm^{-1}. Yet both features were absent for the RuHC12 nanoparticles. This was observed previously and accounted for by the formation of ruthenium-vinylidene (Ru=C=CH–) conjugated interfacial linkages through a tautomeric rearrangement process when alkyne ligands were self-assembled onto ruthenium surfaces.[23,24] In these studies, the three vibrational features within the range of 1910 and 2090 cm^{-1} were assigned to the vibrational stretches of the particle-bound acetylene moieties where the red-shift, as compared to that of the monomeric ligands, was ascribed to intraparticle charge delocalization between the acetylene groups because of the formation of conjugated metal-ligand interfacial bonds.[23,24] However, consistent vibrational features can also be seen with the RuLA and RuSC12 nanoparticles that possessed no acetylene (C≡C) moieties. Thus, it is likely that these spectral features were due to the ruthenium-hydride (Ru-H) vibrations instead, where the hydrogen was generated from the thermolysis of 1,2-propanediol. In fact, in early studies of ruthenium hydride complexes[25] and hydrogen adsorption on CeO_2-supported ruthenium surfaces,[26] the Ru-H vibrations were observed within the range of 1850 and 2050 cm^{-1}, where the variation of the vibrational frequency was ascribed to adsorption onto different metal surface sites.

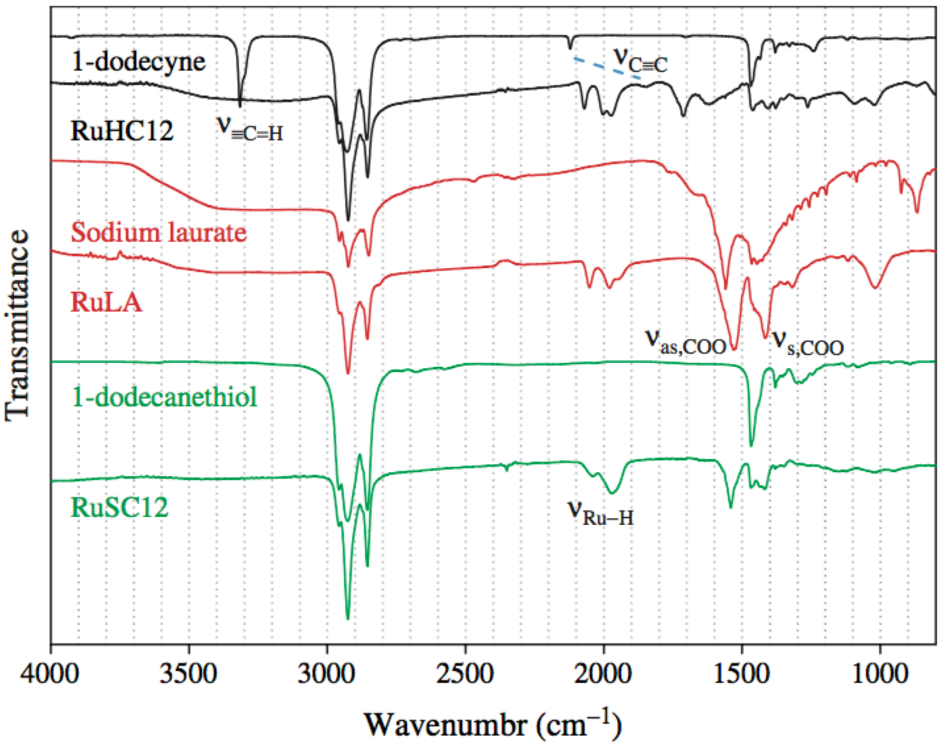

Figure 4.3 FTIR spectra of RuHC12, RuLA, and RuSC12 nanoparticles, along with those monomeric 1-dodecyne, sodium laurate, and 1-dodecanethiol.

With this assignment, the weak vibrational peak at 1847 cm^{-1} is therefore attributed to the particle-bound acetylene moieties, which is consistent with the vibrational frequencies of metal-coordinated acetylene molecules.[27] The rather significant red-shift (272 cm^{-1}), as compared to that of monomeric 1-dodecyne, may be explained by the conjugated ruthenium-vinylidene interfacial bonds such that extended charge delocalization occurred between the particle-bound acetylene moieties.[23,24]

For monomeric sodium laurate, the asymmetric (ν_{as}) and symmetric (ν_s) vibrational stretches of the carboxylate moiety can be found at 1562 and 1449 cm^{-1}. Similar features can be observed with the RuLA nanoparticles but with a rather marked red-shift to 1526 and 1413 cm^{-1}, respectively. This is likely due to the adsorption of the carboxylate moieties onto the Ru nanoparticle surface (Scheme 4.1).[28] Note that in a previous study of anthraquinone-2-carboxylic acid adsorbed on a gold electrode surface,[29] it was proposed that the two oxygen atoms of the COO^- group were bonded to gold symmetrically and the vibrational stretch of the carboxylate moiety also exhibited an apparent red-shift, as compared to that of the monomeric solids.

Therefore, it is likely that in the RuLA nanoparticles, the laurate ligands also formed a similar structure with the carboxylate moieties symmetrically bonded to the Ru surface. Such a structural configuration is in good agreement with the observation that the nanoparticles were readily soluble in apolar organic solvents like CH_2Cl_2 and $CHCl_3$ but not in water or alcohols. For the RuSC12 nanoparticles, the spectral features were consistent with those of monomeric 1-dodecanethiol, as reported earlier.[30] In these nanoparticles, the ligands were bound onto the metal core surface forming Ru–S bonds (Scheme 4.1).

TGA measurements were then carried out to quantitatively evaluate the amounts of organic ligands on the Ru nanoparticle surface. As shown in Figure 4.4, the weight loss of all the nanoparticle samples commenced at about 150 °C, exhibited an abrupt transition and ended at around 300 °C, with a total weight loss of 20%, 51% and 39% for the RuHC12, RuLA, and RuSC12 nanoparticles, respectively. The results were consistent with those reported earlier for similar organically capped nanoparticles.[31,32]

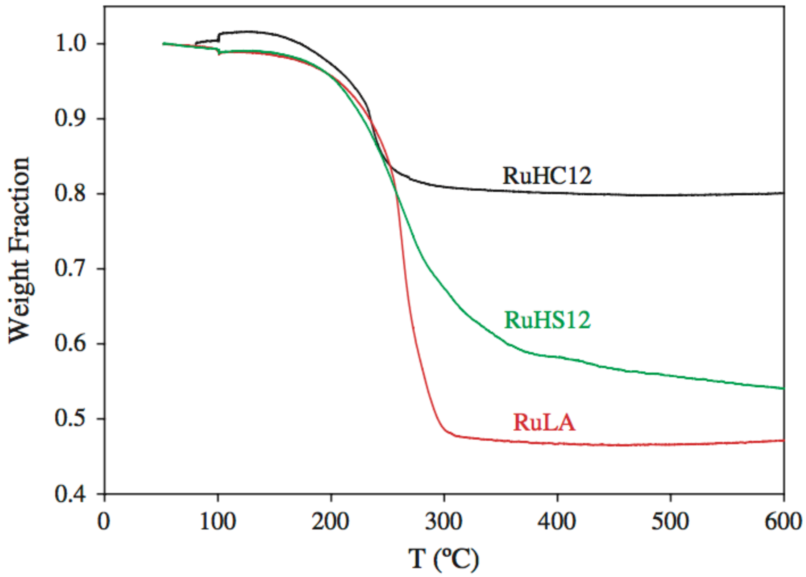

Figure 4.4 TGA curves of RuHC12, RuLA, and RuSC12 nanoparticles measured under a N_2 atmosphere at a heating rate of 10 °C/min.

The difference of the metal-ligand interfacial bonding interactions among these three nanoparticles was also manifested in XPS measurements. As observed earlier,[24] the binding energy of the Ru3d electrons for the RuHC12 nanoparticles was found at

280.45 and 284.36 eV, which increased somewhat to 280.98 and 285.62 eV for the RuSC12 nanoparticles, and further to 281.49 and 285.82 eV for the RuLA nanoparticles. Note that in ruthenium nanoparticles capped by acetylene derivatives, the ruthenium-vinylidene (Ru=C=CH–) interfacial bonds were formed by a tautomeric rearrangement process, which were mostly covalent in nature.[4] In contrast, the interfacial linkages became increasingly polarized in RuSC12 and RuLA nanoparticles, likely because of partial charge transfer from ruthenium to the anchoring groups of the organic capping ligands forming Ru–S and Ru–O bonds.

The impacts of the metal-ligand interfacial bonding interactions on the nanoparticle electron-transfer properties were then evaluated by STS measurements of individual nanoparticles of selected sizes. Figure 4.5 depicts the *I-V* profiles (left panels) and the corresponding derivative (dI/dV, right panels) curves of three representative nanoparticles of each sample (a_i, b_i, and c_i, with i = 1, 2, and 3): (A) RuHC12, (B) RuLA, and (C) RuSC12. The respective insets show the topographs of the nanoparticles for each measurement, from which the topographic radii (r_t) as well as core radii (r) of the nanoparticles were estimated and summarized in Table 4.1.

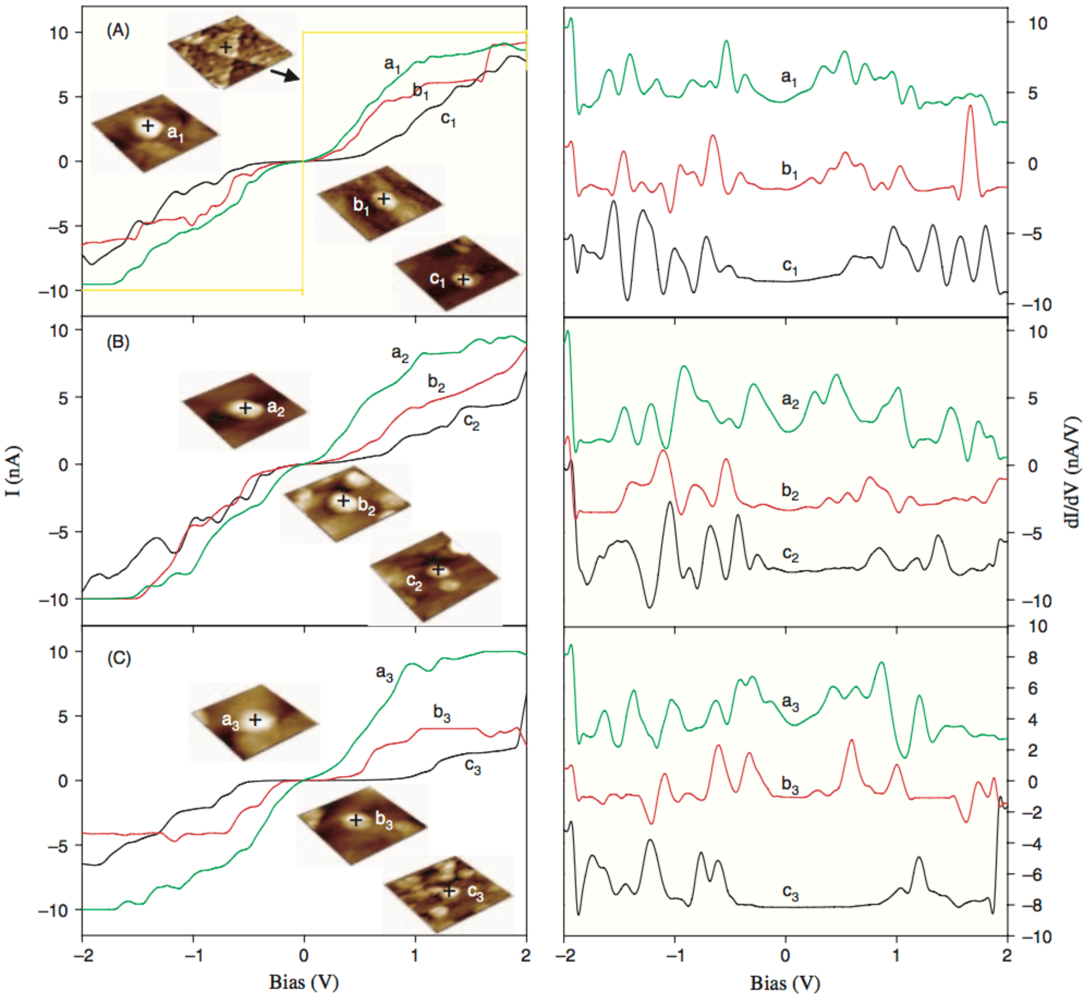

Figure 4.5 (left) I-V and (right) corresponding dI/dV derivative curves of (A) RuHC12, (B) RuLA, and (C) RuSC12 nanoparticles of selected sizes (a_i, b_i, and c_i, with i = 1, 2, 3). Insets show the respective topographic images of the nanoparticles. In panel (A), the I-V curve of the Au substrate is also included (yellow curve).

I–V measurements were carried out by parking the Pt/Ir tip over selected nanoparticles (a_i, b_i, and c_i, with i = 1, 2, and 3) with the feedback loop switched off. There are several aspects that are common to all samples regardless of the metal-ligand interfacial bonds. First, it can be seen from Figure 4.5 that for the largest nanoparticles (a's, diameter ~ 3 nm) all *I-V* profiles (green curves) show a series of rather distinctively defined step-like features, which are largely evenly separated along the bias axis, in contrast to the featureless profile acquired with the tip parked onto the gold substrate surface (yellow curve in panel A). These are the so-called Coulomb staircase that signifies discrete electron tunneling through selected individual nanoparticles, and the slight asymmetry of the tunneling currents in the negative and positive bias regions was ascribed to nonzero residual charge residing on the nanoparticles.[33] For the RuHC12 nanoparticles (a_1, r = 1.54 nm), the average potential spacing (ΔV) between neighboring current steps was estimated to be 0.22 V, which increases to 0.26 V for the RuLA nanoparticles (a_2, r = 1.84 nm), and 0.30 V for RuSC12 nanoparticles (a_3, r = 1.35 nm). From these, the nanoparticle capacitance (C) may be estimated by $C = e/\Delta V$ to be 0.73 aF, 0.62 aF and 0.53 aF, respectively.

In contrast, for the smallest nanoparticles (c's, diameter < 1 nm, black curves), one may notice that whereas the tunneling currents exhibited step-like features at very negative or positive bias, there was essentially zero conductance in the central region around zero bias. This is the so-called Coulomb blockade and its appearance has been ascribed to the emergence of a semiconductor-like bandgap because of the ultrasmall size of the metal nanoparticles.[16,34] For instance, the width of the Coulomb blockade was estimated to be about 0.94 V for particle c_1 (r = 0.34 nm), which increases to 1.00 V for particle c_2 (r = 0.29 nm) and further to 1.21 V for particle c_3 (r = 0.30 nm). From this gap the electrostatic charging energy ($E_c = e^2/2C$) may be quantified to be about 0.47 eV, 0.50 eV and 0.61 eV, respectively, and thus the corresponding nanoparticle capacitance (C) is 0.17 aF (c_1), 0.16 aF (c_2), and 0.13 aF (c_3).

For nanoparticles in the intermediate size range (b's), both Coulomb blockade and Coulomb staircase features can be observed, with the potential gaps of Coulomb blockade smaller than those of particles c's.[16,34] Based upon these, the corresponding nanoparticle capacitance was estimated to be 0.32 aF (b_1, r = 0.79 nm), 0.55 aF (b_2, r = 1.24 nm), and 0.26 aF (b_3, r = 0.65 nm). These data are summarized in Table 4.1.

Note that for organically capped nanoparticles, the particle capacitance can be expressed as $C = 4\pi\varepsilon_0\varepsilon(r/d)(r+d)$, where ε_0 is the permittivity of free space, ε the dielectric constant of the ligand shell, *r* the metal core radius, and *d* the fully extended chainlength of the organic capping ligands.[35] Thus, from this equation, one may quantify the effective dielectric constant of the nanoparticles, which are listed in Table 4.1. Note that the dielectric constants for bulk 1-dodecyne, sodium laurate, and 1-dodecanethiol are all very close, at 2.2, 2.3, and 2.0, respectively.[36,37] Yet from Table 4.1, it can be seen that for the largest nanoparticles (a's) the calculated dielectric constants were all very close to their respective bulk values; and the ε value exhibited an apparent increase with shrinking particle dimensions. This is likely because of the increasing surface curvatures of the nanoparticle cores of diminishing dimensions. The resulting tilting of the organic capping ligands means that the effective thickness of the organic capping layers is markedly smaller than the corresponding fully extended chain length. The tilting is anticipated to be most significant with the laurate ligands because of the large anchoring moiety (carboxylate, Scheme 4.1). This is consistent with the largest deviation observed with RuLA (c_2), as compared to RuHC12 (c_1) and RuSC12

(c_3). Additional contributions may arise from the effective dielectric constants of the metal cores that have been known to increase with decreasing particle core size.[38,39]

Table 4.1 Summary of the topograghic radii (r_t), core radii (r), molecular capacitance (C) and effective dielectric constants (ε) of selected nanoparticles.

		r_t (nm)	r (nm)	C (aF)	ε
RuHC12	a_1	2.90	1.54	0.73	2.00
	b_1	2.15	0.79	0.32	2.30
	c_1	1.70	0.34	0.17	3.60
RuLA	a_2	2.96	1.45	0.62	1.96
	b_2	2.75	1.24	0.55	2.20
	c_2	1.80	0.29	0.16	4.17
RuSC12	a_3	2.90	1.35	0.53	1.90
	b_3	2.20	0.65	0.26	2.27
	c_3	1.88	0.30	0.13	3.26

A close analysis shows that the nanoparticle dielectric constants indeed increase linearly with the reciprocal of the particle core radius, as depicted in Figure 4.6. Interestingly, based on the linear regressions, one can see that within the present experimental context, at any given particle core size, the effective dielectric constant increases in the order of RuSC12 > RuHC12 > RuLA. Note that in the afore-mentioned XPS measurements, the polarization of the metal-ligand interfacial bonds was found to increase in the order of RuHC12 < RuSC12 < RuLA. Thus, the high dielectric constants observed with RuLA nanoparticles may be ascribed to the highly polarized Ru-O bonds; and the fact that the dielectric constant of the RuHC12 nanoparticles was even higher than that of RuSC12 may be due to the formation of conjugated ruthenium-vinylidene interfacial bonds that leads to extensive spilling of core electrons into the organic capping shell and hence enhanced dielectric constants. This further supports the notion that metal-ligand interfacial bonding contacts play a significant role in the manipulation of nanoparticle optical and electronic properties.

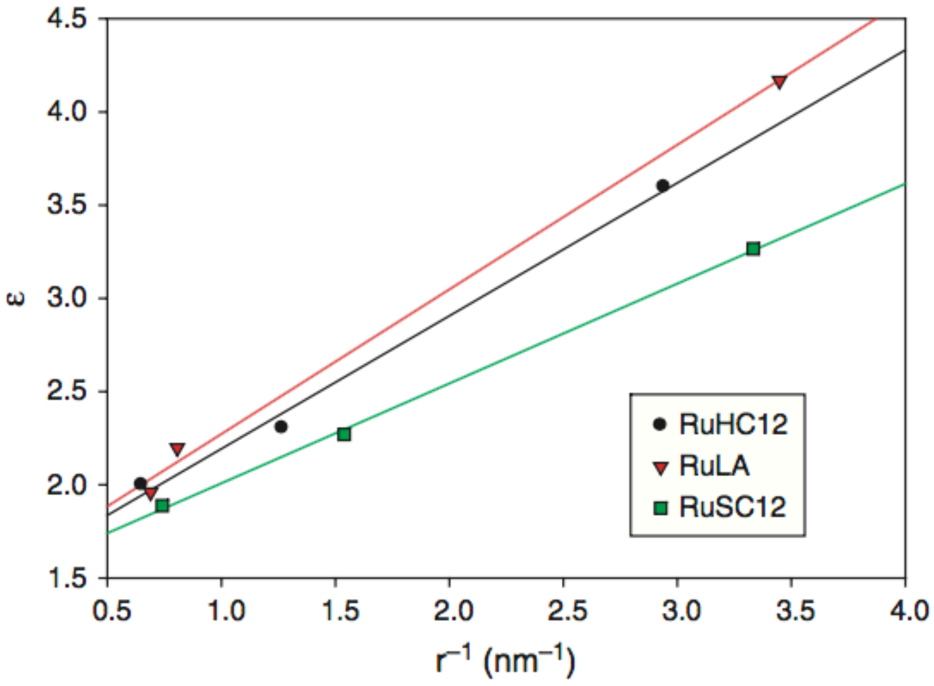

Figure 4.6 Variation of nanoparticle dielectric constant (ε) with the reciprocal of particle core size (r). Symbols are experimental data from Table 4.1, and lines are the corresponding linear regressions.

4.4 Conclusion

In this work, stable ruthenium nanoparticles were prepared by using three types of organic capping ligands, 1-dodecyne, sodium laurate, and 1-dodecanethiol, forming

Ru=C=CH−, Ru−O and Ru−S interfacial bonds, respectively. TEM studies showed the nanoparticles were about 2 nm in diameter and spectroscopic measurements confirmed the bonding attachments of the organic ligands onto the ruthenium nanoparticle surface. The electron transfer behaviors of these ruthenium nanoparticles were then studied by the STS method. In all three samples, for the large nanoparticles (dia. ~ 3 nm) I-V measurements showed clearly-defined Coulomb staircase features, whereas for small particles (dia. < 2 nm), Coulomb blockade started to emerge, and enlarged with diminishing particle core size. Furthermore, based on a concentric structural model, the effective nanoparticle dielectric constants were estimated from the nanoparticle capacitance which showed a clear increase with decreasing particle core size, and within the present experimental context, at any given particle core size, the effective dielectric constants increased in the order of RuSC12 < RuHC12 < RuLA. This is somewhat different from the XPS measurements where the polarization of the interfacial bonds was found to increase in the order of RuHC12 < RuSC12 < RuLA. Whereas the high dielectric constants of RuLA nanoparticles may be accounted for by the highly polarized Ru-O bonds at the metal-ligand interface, the fact that RuHC12 nanoparticles exhibited a higher dielectric constant than RuSC12 was likely due to the formation of conjugated metal-ligand interfacial bonds in RuHC12 that led to intraparticle charge delocalization. These results further support the notion that metal-ligand interafacial bonding interactions play a significant role in manipulating the nanoparticle material properties.

4.5 References

(1) Jeong, Y.; Patra, D.; Sanyal, A.; Rotello, V. M. Fabrication of Stable Nanoparticle-Based Colloidal Microcapsules. *Curr Org Chem* **2013**, *17*, 49-57.

(2) Thaxton, C. S.; Rosi, N. L.; Mirkin, C. A. Optically and chemically encoded nanoparticle materials for DNA and protein detection. *Mrs Bull* **2005**, *30*, 376-380.

(3) Sardar, R.; Funston, A. M.; Mulvaney, P.; Murray, R. W. Gold Nanoparticles: Past, Present, and Future. *Langmuir* **2009**, *25*, 13840-13851.

(4) Kang, X.; Zuckerman, N. B.; Konopelski, J. P.; Chen, S. Alkyne-functionalized ruthenium nanoparticles: Ruthenium-vinylidene bonds at the metal-Ligand interface. *J. Am. Chem. Soc.* **2012**, *134*, 1412-1415.

(5) Kang, X.; Li, X.; Hewitt, W. M.; Zuckerman, N. B.; Konopelski, J. P.; Chen, S. Chemical analysis of surface oxygenated moieties of fluorescent carbon nanoparticles. *Anal. Chem.* **2012**, *4*, 1010-1015.

(6) Yao, C.-J.; Zhong, Y.-W.; Nie, H.-J.; Abruña, H. D.; Yao, J. Near-IR electrochromism in electropolymerized films of a biscyclometalated ruthenium complex bridged by 1,2,4,5-tetra(2-pyridyl)benzene. *J. Am. Chem. Soc* **2011**, *133*, 20720-20723.

(7) Robson, K. C. D.; Koivisto, B. D.; Gordon, T. J.; Baumgartner, T.; Berlinguette, C. P. Triphenylamine-modified ruthenium(II) terpyridine complexes:

Enhancement of light absorption by conjugated bridging motifs. *Inorg. Chem.* **2010**, *49*, 5335-5337.

(8) Ghosh, D.; Chen, S. Solid-state electronic conductivity of ruthenium nanoparticles passivated by metal–carbon covalent bonds. *Chem. Phys. Lett.* **2008**, *465*, 115-119.

(9) Zhu, Y.; Kong, Z. N.; Stubbs, L. P.; Lin, H.; Shen, S.; Anslyn, E. V.; Maguire, J. A. Conversion of Cellulose to Hexitols Catalyzed by Ionic Liquid-Stabilized Ruthenium Nanoparticles and a Reversible Binding Agent. *ChemSusChem* **2010**, *3*, 67-70.

(10) Liu, H.; Yu, C.; Gao, N.; Zhao, J. The diversity of electron-transport behaviors of molecular junctions: Correlation with the electron-transport pathway. *ChemPhysChem* **2010**, *11*, 1895-1902.

(11) Wang, N.; Liu, H.; Zhao, J.; Cui, Y.; Xu, Z.; Ye, Y.; Kiguchi, M.; Murakoshi, K. Theoretical investigation on the electron transport path through the porphyrin molecules and chemisorption of CO. *J. Phys. Chem. C* **2009**, *113*, 7416-7423.

(12) Solomon, E. I.; Penfield, K. W.; Gewirth, A. A.; Lowery, M. D.; Shadle, S. E.; Guckert, J. A.; LaCroix, L. B. Electronic structure of the oxidized and reduced blue copper sites: contributions to the electron transfer pathway, reduction potential and geometry. *Inorg. Chim. Acta* **1996**, *243*, 67-78.

(13) Gorelik, L. Y.; Isacsson, A.; Voinova, M. V.; Kasemo, B.; Shekhter, R. I.; Jonson, M. Shuttle Mechanism for Charge Transfer in Coulomb Blockade Nanostructures. *Phys. Rev. Lett.* **1998**, *80*, 4526-4529.

(14) Park, J.; Pasupathy, A. N.; Goldsmith, J. I.; Chang, C.; Yaish, Y.; Petta, J. R.; Rinkosk, M.; Sethna, J. P.; Abruňa, H. D.; McEuen, P. L.; Ralph, D. C. Coulomb blockade and the Kondo effect in single-atom transistors. *Nature* **2002**, *417*, 722-725.

(15) Fan, F.-R. F.; Bard, A. J. An electrochemical Coulomb staircase: Detection of single electron-transfer events at nanometer electrodes. *Science* **1997**, *277*, 1791-1793.

(16) Chen, S.; Ingram, R. S.; Hostetler, M. J.; Pietron, J. J.; Murray, R. W.; T. Gregory Schaaff; Khoury, J. T.; Alvarez, M. M.; Whetten, R. L. Gold nanoelectrodes of varied size: Transition to molecule-like charging. *Science* **1998**, *280*, 2098-2101.

(17) Tong, M. C.; Chen, W.; Sun, J.; Ghosh, D.; Chen, S. Dithiocarbamate-Capped Silver Nanoparticles. *J. Phys. Chem. B* **2006**, *110*, 19238-19242.

(18) Chen, W.; Ghosh, D.; Sun, J.; Tong, M. C.; Deng, F.; Chen, h. Dithiocarbamate-protected ruthenium nanoparticles: Synthesis, spectroscopy, electrochemistry and STM studies. *Electrochim. Acta* **2007**, *53*, 1150-1156.

(19) Thomas, P. J.; Kulkarni, G. U.; Rao, C. N. R. Effect of size on the Coulomb staircase phenomenon in metal nanocrystals. *Chem. Phys. Lett.* **2000**, *321*, 163-168.

(20) Xu, L.-P.; Chen, S. Scanning tunneling spectroscopy of gold nanoparticles: Influences of volatile organic vapors and particle core dimensions. *Chem. Phys. Lett.* **2009**, *468*, 222-226.

(21) Kang, X.; Zuckerman, N. B.; Konopelski, J. P.; Chen, S. Alkyne-stabilized ruthenium nanoparticles: Manipulation of intraparticle charge delocalization by nanoparticle charge states. *Angew. Chem.* **2010**, *122*, 9686-9689.

(22) Danheiser, R. L.; Miller, R. F.; Brisbois, R. G.; Park, S. Z. An Improved Method for the Synthesis of Alpha-Diazo Ketones. *J Org Chem* **1990**, *55*, 1959-1964.

(23) Kang, X. W.; Zuckerman, N. B.; Konopelski, J. P.; Chen, S. W. Alkyne-Functionalized Ruthenium Nanoparticles: Ruthenium-Vinylidene Bonds at the Metal-Ligand Interface. *J Am Chem Soc* **2012**, *134*, 1412-1415.

(24) Kang, X. W.; Chen, S. W. Electronic conductivity of alkyne-capped ruthenium nanoparticles. *Nanoscale* **2012**, *4*, 4183-4189.

(25) Silantyev, G. A.; Filippov, O. A.; Tolstoy, P. M.; Belkova, N. V.; Epstein, L. M.; Weisz, K.; Shubina, E. S. Hydrogen Bonding and Proton Transfer to Ruthenium Hydride Complex CpRuH(dppe): Metal and Hydride Dichotomy. *Inorg Chem* **2013**, *52*, 1787-1797.

(26) Hashimoto, K.; Toukai, N. Decomposition of ammonia over a catalyst consisting of ruthenium metal and cerium oxides supported on Y-form zeolite. *J Mol Catal a-Chem* **2000**, *161*, 171-178.

(27) Cho, H. G.; Andrews, L. Infrared Spectra of M-eta(2)-C2H2, HM-C CH, and HM-C CH- Prepared in Reactions of Laser-Ablated Group 3 Metal Atoms with Acetylene. *J Phys Chem A* **2012**, *116*, 10917-10926.

(28) Durap, F.; Zahmakiran, M.; Ozkar, S. Water soluble laurate-stabilized rhodium(0) nanoclusters catalyst with unprecedented catalytic lifetime in the hydrolytic dehydrogenation of ammonia-borane. *Appl Catal a-Gen* **2009**, *369*, 53-59.

(29) Han, S. W.; Joo, S. W.; Ha, T. H.; Kim, Y.; Kim, K. Adsorption characteristics of anthraquinone-2-carboxylic acid on gold. *J Phys Chem B* **2000**, *104*, 11987-11995.

(30) Hostetler, M. J.; Stokes, J. J.; Murray, R. W. Infrared spectroscopy of three-dimensional self-assembled monolayers: N-alkanethiolate monolayers on gold cluster compounds. *Langmuir* **1996**, *12*, 3604-3612.

(31) Kang, X.; Chen, S. Electronic conductivity of alkyne-capped ruthenium nanoparticles. *Nanoscale* **2012**, *4*, 4183-4189.

(32) Zhou, Z.-Y.; Kang, X.; Song, Y.; Chen, S. Ligand-Mediated Electrocatalytic Activity of Pt Nanoparticles for Oxygen Reduction Reactions. *J. Phys. Chem. C* **2012**, *116*, 10592-10598.

(33) Majumdar, K.; Hershfield, S. Magnetoresistance of the double-tunnel-junction Coulomb blockade with magnetic metals. *Phys. Rev. B* **1998**, *57*, 11521-11526.

(34) Yang, Y. Y.; Chen, S. W. Surface manipulation of the electronic energy of subnanometer-sized gold clusters: An electrochemical and spectroscopic investigation. *Nano Letters* **2003**, *3*, 75-79.

(35) Chen, S.; Murray, R. W.; Feldberg, S. W. Quantized capacitance charging of monolayer-protected Au clusters. *J. Phys. Chem. B* **1998**, *102*, 9898-9907.

(36) Lide, D. R.: *CRC Handbook of Chemistry and Physics*; Electronic ed.; CRC Press: Boca Raton, FL, 2001.

(37) Parthasarathy, R.; Lin, X.-M.; Jaeger, H. M. Electronic transport in metal nanocrystal arrays: The effect of structural disorder on scaling behavior. *Phys. Rev. Lett.* **2001**, *87*, 186807.

(38) Kuzma, A.; Chovan, J.; Uherek, F.; Weis, M. Surface Plasmon Resonance of Gold and Silver Nanoparticle Monolayers: Effect of Coupling and Surface Oxides. *Proceedings of SPIE* **2013**, *8915*, 89151N-89151.

(39) Kreibig, U. Electronic Properties of Small Silver Particles - Optical-Constants and Their Temperature-Dependence. *J Phys F Met Phys* **1974**, *4*, 999-1014.

Chapter 5

Intervalence Charge Transfer of Ruthenium-Nitrogen Moieties Embedded within Nitrogen-Doped Graphene Quantum

Reproduced with permission from (Limei Chen, Peiguang Hu, Christopher P. Deming, Nan Wang, Jia En Lu, and Shaowei Chen. "Intervalence Charge Transfer of Ruthenium-Nitrogen Moieties Embedded within Nitrogen-Doped Graphene Quantum Dots", J. Phys. Chem. C, 2016, 120, 13303.) Copyright © 2016 American Chemical Society.

5.1 Introduction

Electronic communication between metal centers of mixed-valence complexes has received significant attention in recent decades.[1-3] Depending on the extent of electronic coupling, the complexes are classified by Robin and Day into three categories: Class I (uncoupled), Class II (moderately coupled), and Class III (strongly coupled), which refer to no or little interaction between metal centers at mixed valence, partially delocalized mixed-valence system, and fully delocalized system, respectively.[4] To date, most studies have focused on organometallic complexes where multiple metal centers are bridged by conjugated chemical linkers. At mixed valence, these complexes demonstrate novel photochemical and electrochemical properties that arise from intervalence charge transfer (IVCT) between the metal centers. The electrochemical signatures typically entail the appearance of at least two voltammetric wave, and spectroscopically an apparent absorption band emerges in the visible to near-infrared (NIR) range. Such a unique character may be exploited for diverse applications.[5,6]

Among these, ruthenium-based organometallic complexes have been used rather extensively as the illustrating examples because ruthenium ions are well-known to form strong coordination bonds with various functional moieties, such as nitrogens in pyridine and pyrazine. In fact, IVCT has been observed with a number of ruthenium binuclear complexes with different bridging ligands.[5-8] For instance, studies of the formation and dynamics of the pyrazine-bridged dimer of (Ru_3O) triruthenium clusters have shown that electron transfer is fast and delocalization takes place on the sub-100 fs time scale.[9] In another study, the rate of intramolecular electron transfer between Ru(II) and cobalt(III) metal centers is found to be dominated by the electronic factors instead of the nuclear factors.[10] Additionally, the $[(Ru(bpy)_2)_2(m\text{-}hat)]^{n+}$ compound (hat = 1,4,5,8,9,12-hexaazatriphenylene and bpy = 2,2′-bipyridine) has been prepared and exhibited two pairs of voltammetric peaks that are separated by 220 mV and a NIR peak at 1250–2850 nm at mixed valence, corresponding to a Class II/III delocalized system.[5] In another study, the $[(bpy)_2ClRu(pyz)RuCl(bpy)_2]^{3+}$ complex (pyz = pyrazine) is found to behave as a Class II system, with a potential separation of 120 mV between the two voltammetric peaks and a NIR absorption band at 1300 nm.[7] IVCT has also been observed with the meso-$[\{Ru(bpy)_2\}^{2,3}{}_2(l\text{-}ppz)]^{5+}$ complex (ppz = 4,7-phenanthrolino[6,5-*b*]-pyrazine) which exhibits a NIR absorption at 1862 nm and a potential separation of 224 mV between the voltammetric peaks.[4] Apparent electronic coupling has also been observed with the cyclometalated bis-ruthenium complex bridged by the 2,7-bis-deprotonated form of 1,3,6,8-tetra(pyridin-2-yl)-9-butyl-9*H*-carbazole, which exhibits a high potential separation of 250 mV in voltammetric measurements.[11] In these biruthenium complexes, the extent of IVCT is determined by both the metal centers and the bridging ligands, where the metal–metal charge transfer (MMCT) is generally believed to follow a through-bond pathway (i.e., through the bridging ligands).[4,12]

Thus, an immediate question arises. Will IVCT occur between metal centers embedded within a graphene molecular skeleton? In a prior study, graphene oxide (GO) nanosheets were used as a bridging matrix to study IVCT between ferrocene centers connected by the large π–π* conjugated structure of GO, where two pairs of voltammetric peaks were observed with a peak separation of 515 mV.[13] Significantly, graphene derivatives are known to be readily doped with various heteroatoms depending on the synthetic procedures, which may be exploited for the embedment of metal centers into the conjugated graphitic scaffolds, rendering it possible to study (long-range) graphene-mediated MMCT.[14,15] In fact, nitrogen-doped graphene derivatives can be readily prepared with the nitrogen dopants in various molecular configurations such as pyridinic, pyrrolic, graphitic, etc.[16-19] Of these, it is most likely that the pyridinic nitrogens would behave analogously to pyridine derivatives and chelate with ruthenium ions.[20,21] This will lead to the incorporation of multiple metal centers within the conjugated C sp^2 network, where effective electronic communication most probably takes place (Scheme 5.1). This is the primary motivation of the present study.

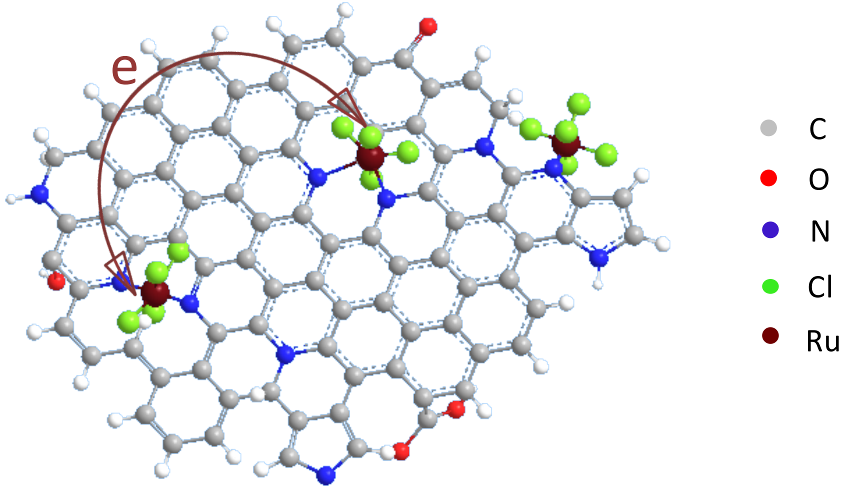

Scheme 5.1

Herein, citric acid and urea were used as the precursors to synthesize luminescent nitrogen-doped graphene quantum dots (NGQDs) by a facile hydrothermal method, in which urea acted as both the base and the N doping source. Complexation with ruthenium ions was achieved by thermal refluxing of NGQDs with $RuCl_2(DMSO)_4$. The resulting compounds (Ru-NGQDs) showed unique spectroscopic and electrochemical properties that suggested IVCT between the ruthenium metal centers at mixed valence.

5.2 Experimental section

Chemicals

Ruthenium chloride ($RuCl_3$, 35–40% Ru, Acros), citric acid monohydrate (99.5%, Acros), urea (99%, Acros), dimethyl sulfoxide (DMSO, 99.7%, Acros), pyridine (99.8%, EMD Millipore), cerium(IV) sulfate ($Ce(SO_4)_2$, 94%, Acros), and potassium nitrate (KNO_3, 99+% Acros) were used as received. Tetra-*n*-butylammonium perchlorate (TBAP, 99+%, TCI America) were recrystallized three times from ethanol prior to use. All solvents were obtained from typical commercial sources and used without further treatment. Water was supplied by a Barnstead Nanopure water system (18.3 MΩ cm).

Synthesis of Nitrogen-Doped Graphene Quantum Dots (NGQDs)

NGQDs were prepared by adopting a procedure published previously.[22] In brief, 0.21 g (1 mmol) of citric acid and 0.18 g (3 mmol) of urea were dissolved in 5 mL of Nanopure water and then transferred into a 20 mL Teflon-lined autoclave. The sealed autoclave was then heated at 160 °C in a furnace for 4 h. The resulting solution was purified by dialysis for 3 days after it was cooled down to room temperature, affording purified NGQDs.

Synthesis of $RuCl_2(DMSO)_4$ Complex

As reported in previous studies,[21,23,24] $RuCl_2(DMSO)_4$ is a convenient starting material for the synthesis of various ruthenium complexes. Briefly, 0.3 g of $RuCl_3$ was dissolved in 10 mL of DMSO and refluxed at 189 °C for 15 min. The solution was found to change to orange-brown rapidly, and addition of excess acetone led to the precipitation of a yellow power. Further purification was achieved by recrystallization from hot DMSO, affording the $RuCl_2(DMSO)_4$compound as a yellow crystal.[25]

Synthesis of Ru-NGQD Compound

To prepare Ru-NGQD compound, 40 mg of NGQDs and 10 mg of $RuCl_2(DMSO)_4$ prepared above were dissolved in 10 mL of water and thermally refluxed at 100 °C for 2 h with the solution purged with a continuous flow of nitrogen. The product was rinsed with a copious amount of ethanol, affording purified Ru-NGQD compound.

Characterizations

The size and morphology of the NGQD and Ru-NGQD compounds were examined by TEM measurements with a JEOL-F 200 kV field-emission analytical transmission electron microscope. Samples were prepared by casting a drop of the solutions in water onto a 200 mesh holey carbon-coated copper grid and dried under ambient conditions. AFM measurements were carried out with a Molecular Imaging PicoLE SPM instrument. UV–vis absorption spectra were acquired with a PerkinElmer Lambda 35 UV–vis spectrometer, and NIR spectra were acquired with an Ocean Optics NIR-512 spectrometer using a 1 cm quartz cuvette. Photoluminescence measurements were carried out with a PTI fluorospectrometer. FTIR spectra were obtained with a PerkinElmer FTIR spectrometer (Spectrum One, spectral resolution 4 cm^{-1}), where the samples were prepared by casting the sample solutions onto a ZnSe disk. X-ray photoelectron spectra (XPS) were recorded with a PHI 5400/XPS instrument equipped with an Al Kα source operated at 350 W and at 10^{-9} Torr. Silicon wafers were sputtered by argon ions to remove carbon from the background and used as substrates. The spectra were referenced to the Si 2p peak (99.03 eV). Raman spectra were acquired using a Thermo Fisher Scientific DXR Raman Microscope with a 532 nm laser source.

Electrochemistry

Electrochemical measurements were carried out with a CHI 440 electrochemical workstation. A glassy carbon disk electrode with a surface area of 0.78 cm^2 was used as the working electrode. A Ag/AgCl wire and a Pt coil were used as the (quasi)reference and counter electrode, respectively. Prior to use, the working electrodes were polished with 0.5 µm alumina slurries and then cleansed by sonication in Nanopure water.

5.3 Results and Discussion

It has been known that hydrothermal treatment of citric acid and urea at controlled temperatures led to the ready formation of NGQDs.[22] From panels A and B of Figure 5.1, one can see that the NGQDs exhibit a roughly spherical morphology with a narrow size distribution within the range of 1.2–2.7 nm and an average size of 2.0 ± 0.4 nm (Figure 5.1 (E)). The NGQDs also display well-defined lattice fringes where the interplanar spacings of 0.373 and 0.248 nm were consistent with the basal plane distance of graphite (002) and in-plane lattice distance of graphite (1120) crystalline planes, respectively.[22,26,27] After complexation with ruthenium ions (Scheme 5.1), the average size of Ru-NGQDs remained almost invariant at 1.9 ± 0.3 nm (Figure 5.1 (F)); yet the distance between the basal planes increased to 0.387 nm while the in-plane lattice spacing was unchanged at 0.243 nm, as depicted in panels C and D of Figure 5.1. The results imply weakened van der Waals interactions between the basal planes with the embedment of ruthenium ions into the graphitic planes of NGQDs.[28]

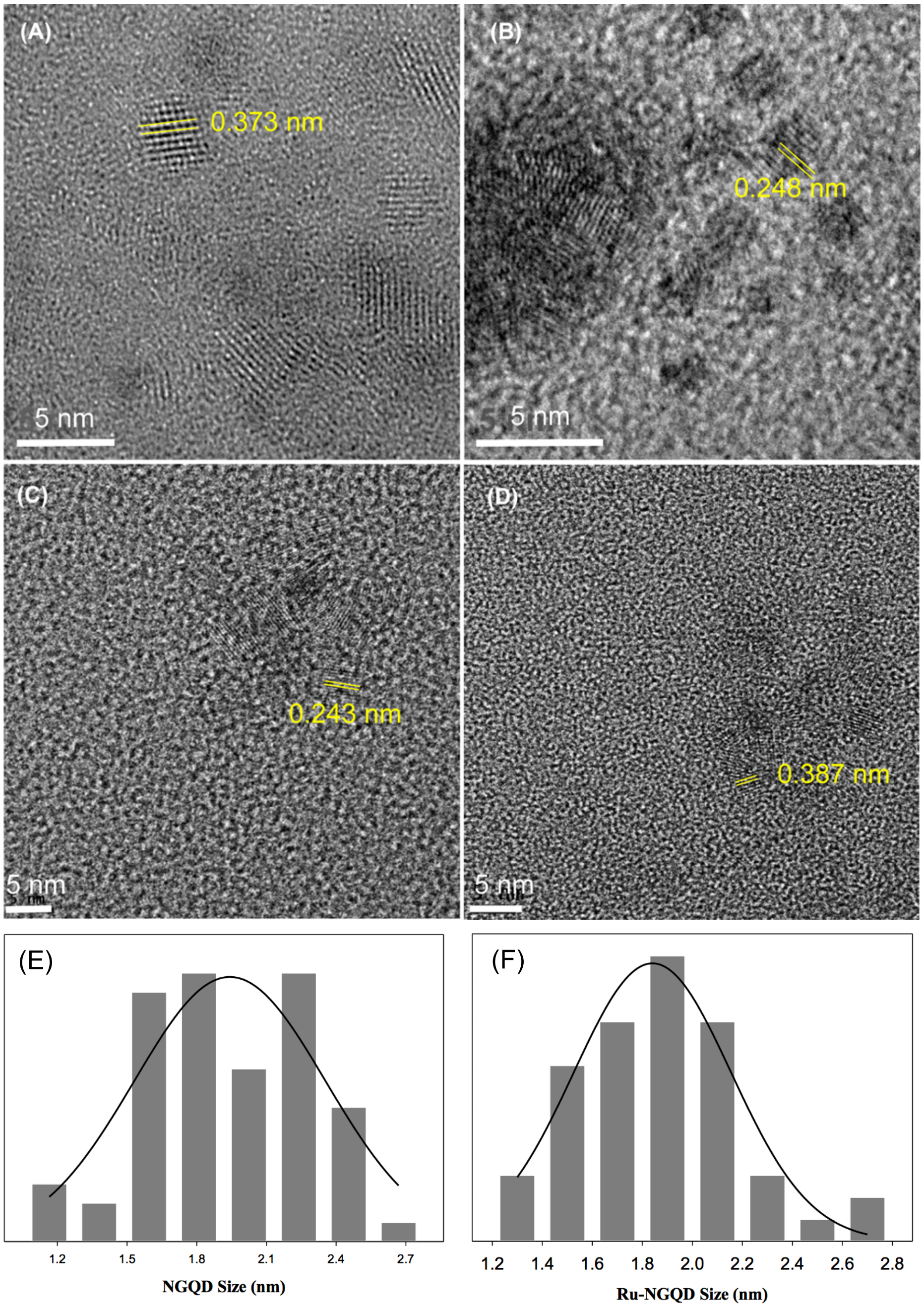

Figure 5.1 Representative HRTEM micrographs and size distribution of (A, B, E) NGQDs and (C, D, F) Ru-NGQDs. Scale bars all 5 nm. Yellow lines highlight the lattice fringes of the NGQDs, and the numbers refer to the interplanar distances between the crystalline planes.

AFM topographic measurements (Figure 5.2) showed that the thickness of NGQDs and Ru-NGQDs were both between 0.6 and 1.2 nm, indicating that NGQDs consisted of three to four layers of graphene.[27,29] FTIR measurements showed that the NGQDs produced in the hydrothermal synthesis actually included a number of oxygenated species, and there was no marked difference after complexation with ruthenium ions, as depicted in Figure 5.3: (A) the broad peak centered at ca. 3210 cm^{-1} is most likely due to the stretching vibrations of O–H moieties; (b) the two bands at 3055 and 2856 cm^{-1} may be ascribed to the sp^2 and sp^3 C–H stretches, respectively;[15] and the peaks at 1707 cm^{-1} can be assigned to C=O, whereas the multiple bands between 1600 and 1300 cm^{-1} likely arise from C=C (with additional contributions from C=N) and 1176 cm^{-1} from C–O (and C–N).[22,30,31]

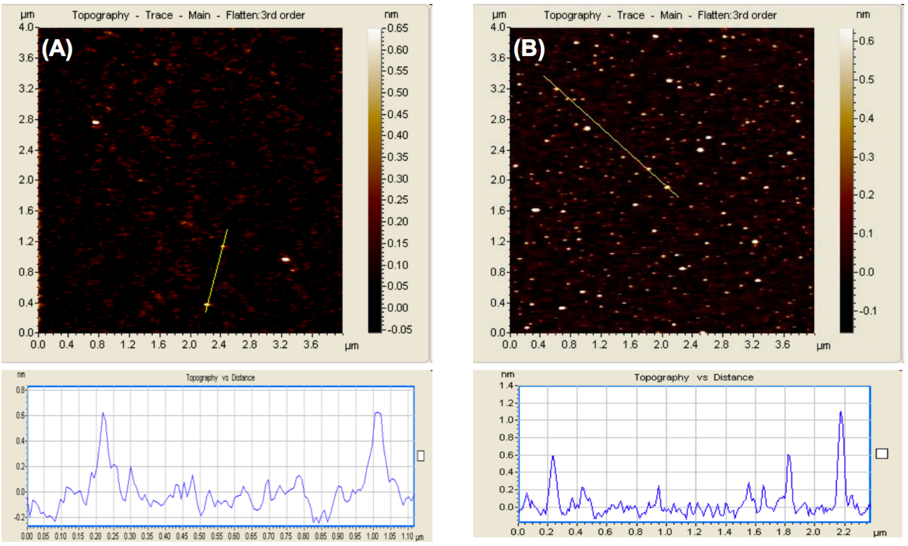

Figure 5.2 AFM images of (A) NGQDs and (B) Ru-NGQDs deposited on a mica substrate. The bottom panels are the topographic height profiles along the yellow lines in the AFM images.

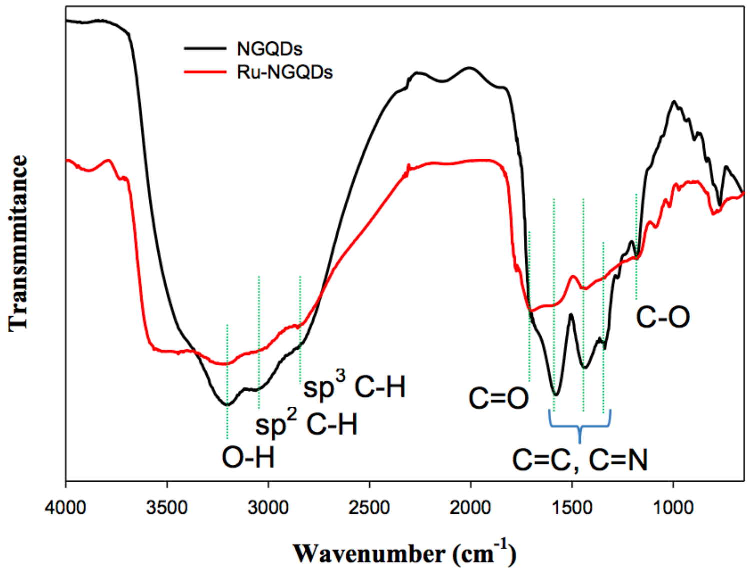

Figure 5.3 FTIR spectra of NGQDs and Ru-NGQDs.

The chemical composition and nitrogen configurations of the NGQD and Ru-NGQD compounds were then examined by XPS measurements. Figure 5.4(A) depicts the survey spectrum of Ru-NGQDs, where three main peaks can be identified at around 285, 401, and 532 eV, corresponding to the C 1s (Ru 3d), N 1s, and O 1s electrons, respectively.[32] From the high-resolution scan of the C 1s (Ru 3d) electrons in Figure 5.4(B), one can see that deconvolution yields five major components. The doublet at 281.6 eV (yellow curve) and 285.7 eV (blue curve) can be assigned to the Ru $3d_{5/2}$ and Ru $3d_{3/2}$ electrons of Ru(II)–pyridine moieties (Figure 5.4 (E)), respectively, along with C═C (pink curve, 284.5 eV), C–C/C–N (cyan curve, 285.3 eV), C–O (gray curve, 286.5 eV), and O–C═O (dark red curve, 288.3 eV).[33-36] Again, this indicates that the NGQDs were indeed functionalized with a number of oxygenated species and ruthenium ions were incorporated into the GQD molecular skeleton. Similarly, three subpeaks can be identified by deconvolution of the N 1s spectrum in Figure 5.4(C) at 399.3, 400.6, and 402.0 eV, which may be assigned to the pyridinic, pyrrolic, and graphitic N, respectively.[37-39] Interestingly, in comparison with the original NGQDs (Figure 5.4 (F)), whereas the binding energies of the pyrrolic, and graphitic nitrogens remained virtually unchanged, the pyridinic nitrogen exhibited a blue-shift of about 0.7 eV. Note that an increase of 0.4 eV has been observed of the N 1s binding energy upon the formation of Ru(II)–polypyridine complexes.[40] This suggests that ruthenium ions were incorporated into the NGQDs most probably by the complexation between Ru(II) and pyridinic nitrogen,[41] leading to apparent polarization of the nitrogen electrons, whereas complexation interactions with other nitrogen dopants were minimal (Scheme 5.1). Furthermore, based on the integrated peak areas, the N/C atomic ratio in NGQDs was estimated to be ca. 0.15:1, among which 57.6% was pyrrolic nitrogen, 27.0% graphitic nitrogen, and 15.4% pyridinic nitrogen. This corresponds to a Ru:pyridinic N molar ratio of 1:2.3 (the atomic ratio of Ru:C was ca. 0.01:1), implying incomplete coordination of the ruthenium metal centers by pyridinic nitrogens (Figure 5.5), although the exact coordination structure remained unknown at this point.

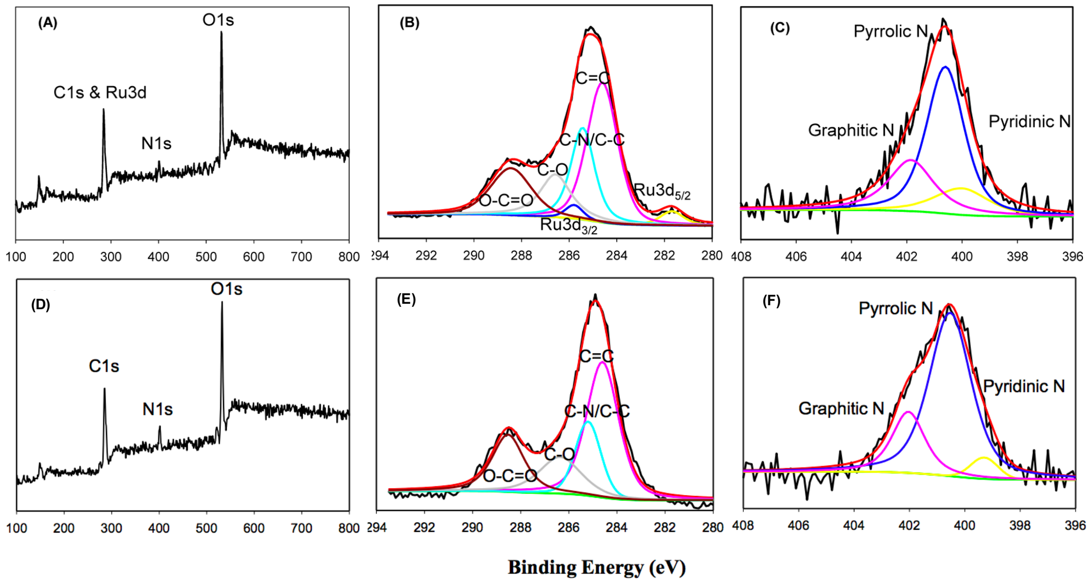

Figure 5.4. XPS survey spectrum and the corresponding high-resolution scans of C 1s (Ru 3d) and N 1s electrons for (A, B, C) Ru-NGQD and (D, E, F) NGQDs. In (B, E), the black curve is experimental data, and the red curve is the sum of deconvolution fits (yellow curve for Ru 3d5/2, blue curve for Ru 3d3/2, pink curve for C═C, cyan curve for C–N/C–C, gray curve for C–O, and dark red curve for O–C═O). In (C, F), the black curve is experimental data, and red curve is the sum of deconvolution fits (green curve for the baseline, yellow curve for pyridinic N, blue curve for pyrrolic N, and pink curve for graphitic N).

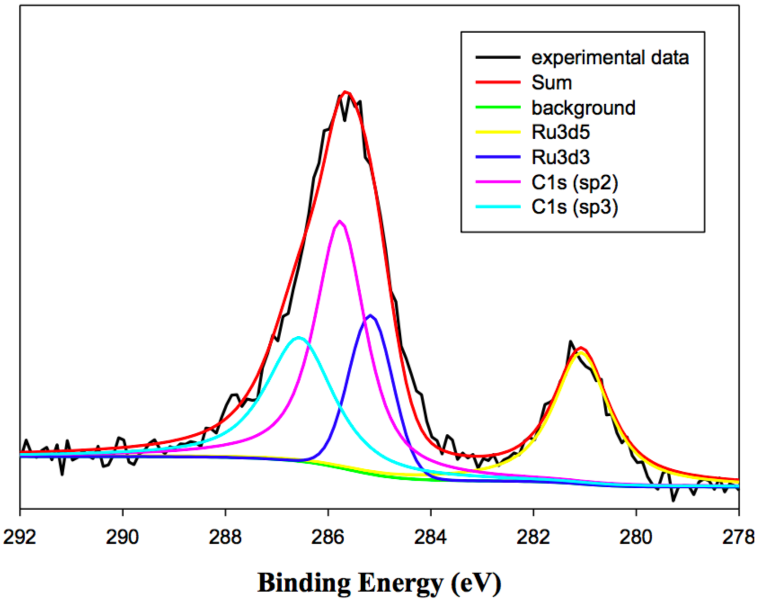

Figure 5.5 XPS spectrum of the C1s and Ru3d electrons of $RuCl_2(Py)_4$ synthesized from $RuCl_2(DMSO)_4$. Black curve is the experimental data and colored curves are deconvolution fits.

The molecular structures of the NGQD and Ru-NGQD compounds were further examined by Raman measurements. From Figure 5.6, one can see that NGQDs exhibited two vibrational bands at 1317 and 1587 cm^{-1}, characteristic of the D and G bands of graphene derivatives.[33-36] After complexation with ruthenium ions, these two bands shifted to 1358 and 1584 cm^{-1}. That is, the G band energy remained virtually unchanged, whereas the D band energy showed a substantial blue-shift of 41 cm^{-1}. This is in good agreement with the embedment of cationic ruthenium metal centers into the graphene skeleton, a behavior analogous to hole doping that has been found to lead to an increase of the D band frequency of graphene.[42] In addition, the ratio of the D and G band intensity (I_D/I_G) was found to increase from 0.89 (NGQDs) to 1.02 (Ru-NGQDs), again consistent with the complexation of ruthenium ions with pyridinic N atoms in NGQDs that resulted in structural distortion of the graphene sheets, as observed in TEM measurements where the distance between the NGQD basal planes increased (Figure 5.1).

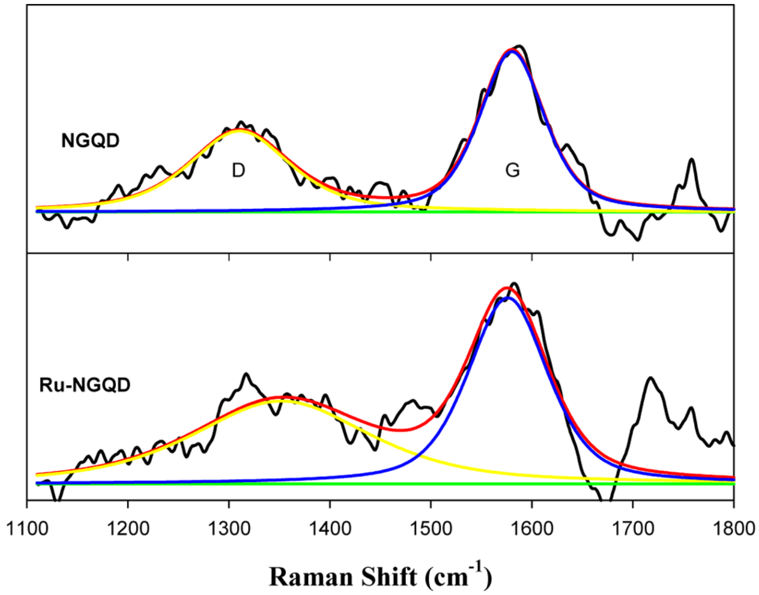

Figure 5.6. Raman spectra of NGQD and Ru-NGQD compounds. Black curves are experimental data, and red curves are the sum of deconvolution fits (yellow curves for the D band, blue curves for the G band, and green curves for the baseline).

The incorporation of ruthenium ions into the NGQD molecular skeleton also led to marked variations of the optical properties. Figure 5.7(A) depicts the UV–vis absorption spectra of NGQDs and Ru-NGQDs. Two major absorption bands can be observed at 235 and 339 nm with the NGQD sample (black curve). Of those, the 235 nm absorption band may be assigned to the π → π* transition of the C sp^2 domains,[14,43] while the peak at 339 nm is likely due to the n → π* transition of C═O bonds as well as the transition of conjugated C–N/C═N.[15] The absorption profile was markedly different upon the incorporation of ruthenium metal centers. Specifically, Ru-

NGQDs (red curve) displayed two absorption peaks at 350 and 407 nm, likely due to the varied degrees of coordination of the ruthenium metal centers with pyridinic N that impacted the C–N/C═N transitions—note that $RuCl_2(Py)_4$ also exhibited a well-defined absorption peak at 405 nm (Figure 5.8(A)). In contrast, with undoped GQDs, the UV–vis spectra were virtually invariant, suggesting the lack of complexation of ruthenium ions to the GQDs (Figure 5.8(B)). Additionally, a broad band centered at ca. 576 nm can also be found, which might be ascribed to metal–ligand charge transfer (MLCT) of the ruthenium–pyridinic N moieties.[44]

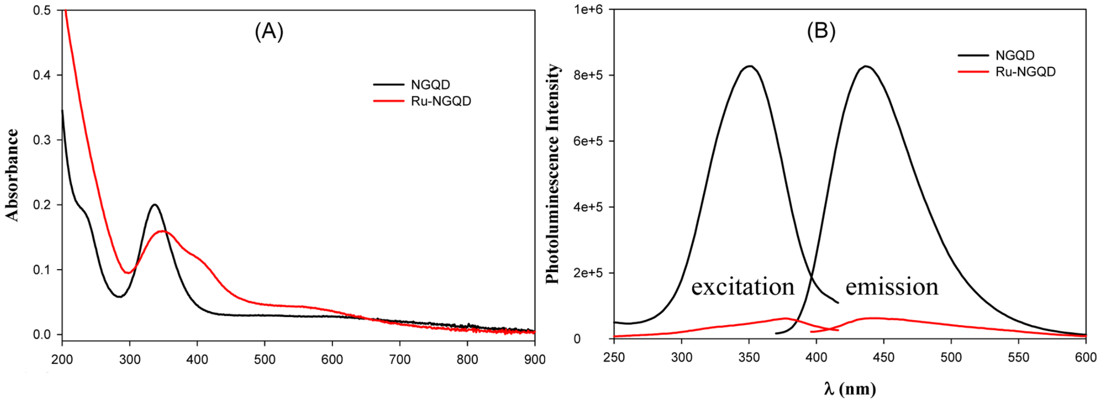

Figure 5.7 (A) UV–vis absorption and (B) photoluminescence spectra of NGQDs and Ru-NGQDs in water. The photoluminescence spectra in (B) have been normalized to the respective absorbance at the excitation wavelength in (A).

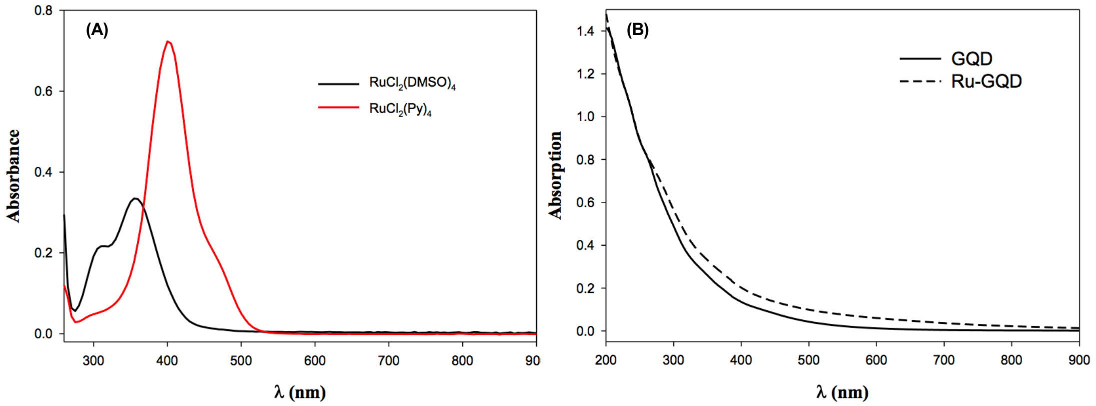

Figure 5.8 (A)UV-vis spectra of $RuCl_2(DMSO)_4$ and $RuCl_2(Py)_4$ in DMF and (B) undoped GQDs before and after mixing with ruthenium ions in water.

An apparent difference is also observed in photoluminescence measurements. Figure 5.7(B) shows the excitation and emission spectra of NGQDs and Ru-NGQDs in water. For NGQDs, the excitation maximum (λ_{ex}) can be identified at 350 nm and the corresponding emission maximum (λ_{em}) at 434 nm, suggesting that the emissions were largely due to the transitions of the C═O and C–N/C═N moieties.[15] The small peak width (full width at half-maximum = ca. 75 nm) suggests a narrow distribution of the NGQD size and surface state.[45] In contrast, one can see that the excitation and emission maxima of Ru-NGQDs red-shifted to 378 and 437 nm, respectively. This may be accounted for by the formation of Ru–N bonds that weakened the electronic transition of C–N/C═N, resulting in a diminishment of the emission energy.[46] Additionally, one can see that the emission intensity of Ru-NGQDs was over 1 order of magnitude lower than that of NGQDs, likely due to the enhanced absorption of Ru-NGQDs in the range of 400–500 nm, where electron transfer from NGQDs to the metal ions led to effective quenching of the photoluminescence.[47] Similar behaviors were observed with the emission in the red (Figure 5.9).

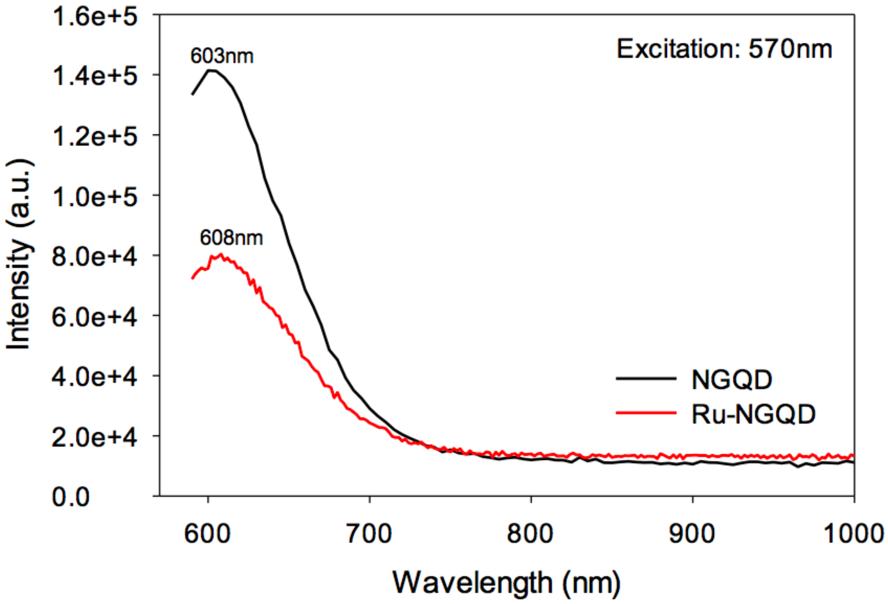

Figure 5.9 Photoluminescence emission spectra of NQGD and Ru-NGQD in water at the excitation wavelength of 570 nm. NGQDs exhibited an emission peak at 603 nm, which red-shifted slightly to 608 nm with Ru-NGQDs. The emission intensity diminished by about 50% from NGQDs to Ru-NGQDs.

Significantly, with the embedment of Ru(II) ions into the conjugated C sp^2 graphitic matrix, the Ru-NGQD compounds exhibited effective charge transfer between the metal centers (i.e., MMCT), as evidenced in NIR spectroscopic and electrochemical measurements. Figure 5.10 depicts the NIR spectra of Ru-NGQD after subtraction of the corresponding ones of NGQDs under the otherwise identical conditions, with the addition of various amounts of $Ce(SO_4)_2$ that acted as the oxidizing reagent.[48] It can be seen that the optical absorbance in the range of 1200–2200 nm initially increased with the addition of increasing amounts of $Ce(SO_4)_2$, reached a maximum when 240 μL of $Ce(SO_4)_2$ was added, and then diminished gradually with a further increase of the $Ce(SO_4)_2$amount. Such a dynamic evolution is better illustrated by the absorption peak at 1450 nm (highlighted by the arrow), as evidenced in Figure 5.10(B), which can be ascribed to the charge transfer between the ruthenium–pyridinic N moieties at mixed valence, a behavior analogous to IVCT of conventional biruthenium complexes[49,50] and nanoparticle-mediated IVCT.[48,50-52] When half of the Ru(II) centers were oxidized (corresponding to the addition of 240 μL of $Ce(SO_4)_2$), maximal MMCT occurred, and thus the absorbance reached the peak. Here, the conjugated C sp^2 scaffolds served as the bridging ligands that allowed effective electronic communication between the ruthenium metal centers (Scheme 5.1). Note that the degree of electronic coupling can be quantitatively described by the parameter Γ, which is calculated according to the classical two-state theory[5]

$$\Gamma=1- \Delta\nu_{1/2(\mathrm{experimental})}/ [16RTln2\nu_{max}]^{1/2}=1- \Delta\nu_{1/2(\mathrm{experimental})}/ \Delta\nu_{1/2}{}^{0}$$

where $\Delta\nu_{1/2(\mathrm{exptl})}$ is the bandwidth at half-height, R is the gas constant, and T is the experimental temperature. From Figure 5.10(A) A, $\Delta\nu_{1/2(\mathrm{exptl})}$ was estimated to be 2087 cm^{-1}, $\nu_{\max} = 6896\ cm^{-1}$, and within the present experimental context $\Delta\nu^{0}{}_{1/2} = 3946\ cm^{-1}$; thus, Γ was calculated to be 0.47. This suggests weak to moderate electronic coupling ($0 < \Gamma < 0.5$) in Ru-NGQD and hence a Class II system.[5,53]

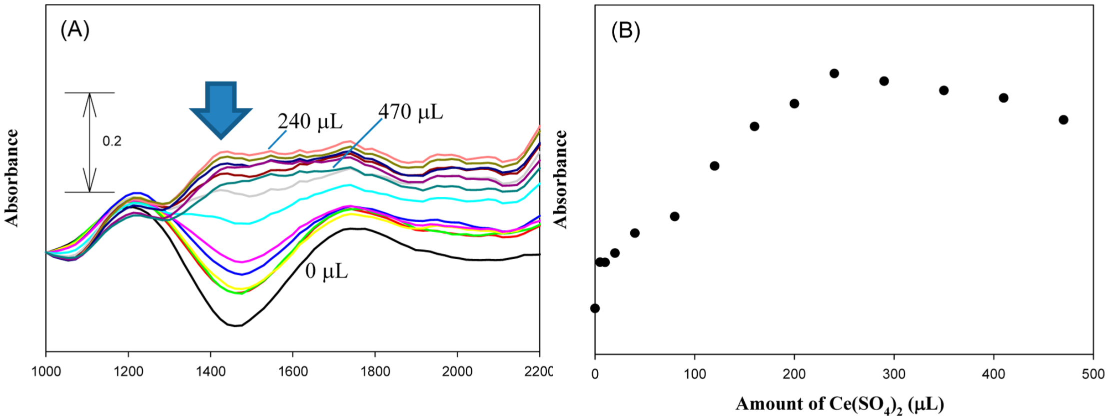

Figure 5.10 (A) NIR spectra of Ru-NGQDs with the addition of varied amounts (0–470 μL) of 0.3 M $Ce(SO_4)_2$ in water after subtraction of the NGQD spectra acquired at the otherwise identical experimental conditions. Arrow indicates the peak at 1450 nm. (B) Variation of the absorbance at 1450 nm with the amount of $Ce(SO_4)_2$ added.

Consistent results are obtained in voltammetric measurements. Figure 5.11 depicts the square wave voltammograms (SWVs) of Ru-NGQDs in water containing 1 M KNO_3 at a glassy carbon electrode, where a pair of broad peaks can be found within the potential range of 0 and +0.9 V (vs Ag/AgCl), in contrast to the largely featureless profiles observed with NGQDs. Interestingly, deconvolution of the Ru-NGQD voltammetric profiles yields two pairs of peaks, with the formal potentials at +0.51 and +0.66 V, respectively. These may be ascribed to the redox reactions involving Ru(III) + e → Ru(II), where IVCT occurred between the ruthenium metal ions embedded within the same NGQD matrix (Scheme 5.1). In addition, the potential separation (150 mV) between these two pairs of peaks fell in the range of 120–230 mV that has been typically observed for Class II complexes involving two or three ruthenium ion centers.[5,54-56] Notably, the results are in good agreement with those from NIR spectroscopic measurements (Figure 5.10).

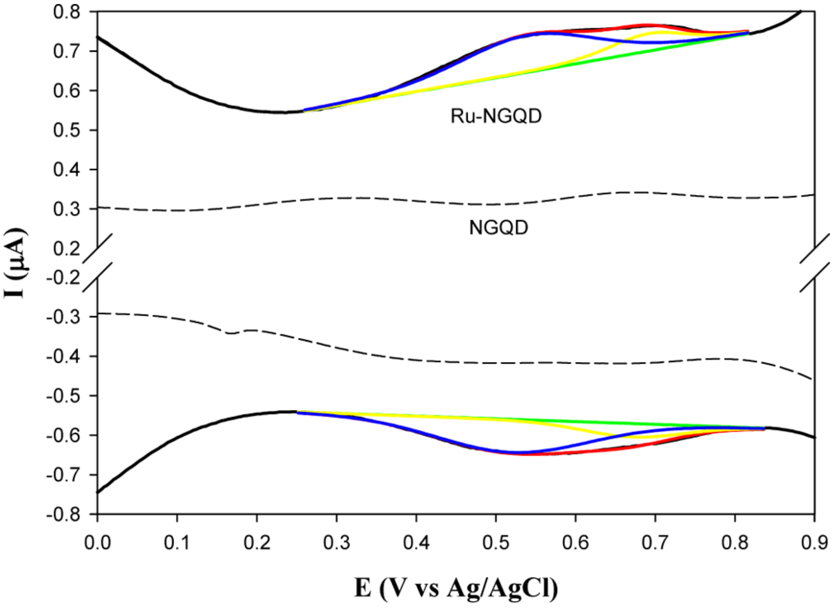

Figure 5.11 Square wave voltammograms of NGQD (dashed black curve) and Ru-NGQDs (solid black curve) in water containing 1 M KNO_3 at a glassy carbon electrode with a surface area of 0.78 cm^2. Increment of potential 2 mV, amplitude 25 mV, and frequency 15 Hz. Colored curves are the deconvolution fits.

5.4 Conclusion

In this study, nitrogen-doped graphene quantum dots were exploited as a unique structural scaffold to incorporate ruthenium(II) ions into the graphitic matrix by the formation of ruthenium–pyridinic N moieties. The resulting compounds exhibited markedly different optical and electrochemical properties as compared to the original NGQDs. Significantly, effective MMCT occurred between the ruthenium metal centers at mixed valence, where the IVCT properties suggested Class II behaviors due to the effective bridging of the metal centers by the conjugated C sp^2 network. The results highlight the unique applications of graphene scaffolds in facilitating nanoscale charge transfer.

5.5 References

(1) Rocha, R. C.; Toma, H. E. Electron transfer in inorganic mixed-valence systems. *Quim Nova* **2002**, *25*, 624-638.

(2) Reimers, J. R.; Cai, Z. L.; Hush, N. S. A priori evaluation of the solvent contribution to the reorganization energy accompanying intramolecular electron transfer: Predicting the nature of the Creutz-Taube ion. *Chem Phys* **2005**, *319*, 39-51.

(3) Wenger, O. S. Photoswitchable mixed valence. *Chem Soc Rev* **2012**, *41*, 3772-3779.

(4) D'Alessandro, D. M.; Keene, F. R. Current trends and future challenges in the experimental, theoretical and computational analysis of intervalence charge transfer (IVCT) transitions. *Chem Soc Rev* **2006**, *35*, 424-440.

(5) D'Alessandro, D. M.; Keene, F. R. Intervalence charge transfer (IVCT) in ruthenium dinuclear and trinuclear assemblies containing the bridging ligand HAT {1,4,5,8,9,12-hexaazatriphenylene}. *Chem-Eur J* **2005**, *11*, 3679-3688.

(6) Ward, M. D. Metal-Metal Interactions in Binuclear Complexes Exhibiting Mixed-Valency - Molecular Wires and Switches. *Chem Soc Rev* **1995**, *24*, 121-134.

(7) Rocha, R. C.; Toma, H. E. Intervalence, electron transfer and redox properties of a triazolate-bridged ruthenium-polypyridine dinuclear complex. *Polyhedron* **2003**, *22*, 1303-1313.

(8) Rocha, R. C.; Brown, M. G.; Londergan, C. H.; Salsman, J. C.; Kubiak, C. P.; Shreve, A. P. Intervalence-resonant Raman spectroscopy of strongly coupled mixed-valence cluster dimers of ruthenium. *J Phys Chem A* **2005**, *109*, 9006-9012.

(9) Petersson, J.; Henderson, J.; Brown, A.; Hammarstrom, L.; Kubiak, C. P. Time-Resolved Electron Transfer in Porphyrin-Coordinated Ruthenium Dimers: From Mixed-Valence Dynamics to Hot Electron Transfer. *J Phys Chem C* **2015**, *119*, 4479-4487.

(10) Creutz, C. Nonadiabatic, short-range, intramolecular electron transfer from ruthenium(II) to cobalt(III) complexes. *J Phys Chem B* **2007**, *111*, 6713-6717.

(11) Wang, L.; Yang, W. W.; Zhong, Y. W.; Yao, J. N. Enhancing the electronic coupling in a cyclometalated bisruthenium complex by using the 1,3,6,8-tetra(pyridin-2-yl)carbazole bridge. *Dalton T* **2013**, *42*, 5611-5614.

(12) Ito, T.; Hamaguchi, T.; Nagino, H.; Yamaguchi, T.; Washington, J.; Kubiak, C. P. Effects of rapid intramolecular electron transfer on vibrational spectra. *Science* **1997**, *277*, 660-663.

(13) Lu, Y. Z.; Jiang, Y. Y.; Wu, H. B.; Chen, W. Ferrocene-Functionalized Graphene Oxide Nanosheets: Efficient Electronic Communication between Ferrocene Centers across Graphene Nanosheets. *Electrochim Acta* **2015**, *156*, 267-273.

(14) Ju, J.; Zhang, R. Z.; He, S. J.; Chen, W. Nitrogen-doped graphene quantum dots-based fluorescent probe for the sensitive turn-on detection of glutathione and its cellular imaging. *Rsc Adv* **2014**, *4*, 52583-52589.

(15) Qu, D.; Zheng, M.; Li, J.; Xie, Z. G.; Sun, Z. C. Tailoring color emissions from N-doped graphene quantum dots for bioimaging applications. *Light-Sci Appl* **2015**, *4*.

(16) Hu, P. G.; Liu, K.; Deming, C. P.; Chen, S. W. Multifunctional graphene-based nanostructures for efficient electrocatalytic reduction of oxygen. *J Chem Technol Biot* **2015**, *90*, 2132-2151.

(17) Fan, X. H.; Phebus, B. D.; Li, L. J.; Chen, S. W. Chemical Functionalization of Graphene Quantum Dots. *Sci Adv Mater* **2015**, *7*, 1990-2010.

(18) Fan, X. H.; Phebus, B. D.; Li, L. J.; Chen, S. W. Graphene-Based Composites for Supercapacitor Electrodes. *Sci Adv Mater* **2015**, *7*, 1916-1944.

(19) Permatasari, F. A.; Aimon, A. H.; Iskandar, F.; Ogi, T.; Okuyama, K. Role of C-N Configurations in the Photoluminescence of Graphene Quantum Dots Synthesized by a Hydrothermal Route. *Sci Rep-Uk* **2016**, *6*.

(20) Gilbert, J. D.; Rose, D.; Wilkinson, G. Preparative Use of Blue Solutions of Ruthenium(Ii) - Ruthenium-(Ii) and Ruthenium-(Iii) Complexes with Amines, Nitriles, Phosphines, Etc. *J Chem Soc A* **1970**, 2765-2769.

(21) Evans, I. P.; Spencer, A.; Wilkinso.G. Dichlorotetrakis(Dimethyl Sulphoxide)Ruthenium(Ii) and Its Use as a Source Material for Some New Ruthenium(Ii) Complexes. *J Chem Soc Dalton* **1973**, 204-209.

(22) Qu, D.; Zheng, M.; Zhang, L. G.; Zhao, H. F.; Xie, Z. G.; Jing, X. B.; Haddad, R. E.; Fan, H. Y.; Sun, Z. C. Formation mechanism and optimization of highly luminescent N-doped graphene quantum dots. *Sci Rep-Uk* **2014**, *4*.

(23) Coe, B. J. Syntheses and characterization of ruthenium(II) tetrakis(pyridine) complexes - An advanced coordination chemistry experiment or mini-project. *J Chem Educ* **2004**, *81*, 718-721.

(24) Jacobsen, C. J. H.; Pedersen, E.; Villadsen, J.; Weihe, H. Esr Characterization of Trans-V(Ii)(Py)4x2 and Trans-Mn(Ii)(Py)4x2 (X = Ncs, Cl, Br, I Py = Pyridine). *Inorg Chem* **1993**, *32*, 1216-1221.

(25) Hazarika, P.; Deka, J.; Bhola, S.; Bhola, R. K.; Medhi, C.; Medhi, O. K. DNA Binding Properties and Biological Studies of Cis-Dichlorotetrakis(dimethylsulfoxide)ruthenium(II) Complex. *Int. J. Drug Des. Discuss.* **2012**, *3*, 907-913.

(26) Tang, L. B.; Ji, R. B.; Li, X. M.; Teng, K. S.; Lau, S. P. Energy-level structure of nitrogen-doped graphene quantum dots. *J Mater Chem C* **2013**, *1*, 4908-4915.

(27) Liu, Q.; Guo, B. D.; Rao, Z. Y.; Zhang, B. H.; Gong, J. R. Strong Two-Photon-Induced Fluorescence from Photostable, Biocompatible Nitrogen-Doped Graphene Quantum Dots for Cellular and Deep-Tissue Imaging. *Nano Lett* **2013**, *13*, 2436-2441.

(28) Dappe, Y. J.; Basanta, M. A.; Flores, F.; Ortega, J. Weak chemical interaction and van der Waals forces between graphene layers: A combined density functional and intermolecular perturbation theory approach. *Phys Rev B* **2006**, *74*.

(29) Ding, Z. C.; Hao, Z.; Meng, B.; Xie, Z. Y.; Liu, J.; Dai, L. M. Few-layered graphene quantum dots as efficient hole-extraction layer for high-performance polymer solar cells. *Nano Energy* **2015**, *15*, 186-192.

(30) Hu, C. F.; Liu, Y. L.; Yang, Y. H.; Cui, J. H.; Huang, Z. R.; Wang, Y. L.; Yang, L. F.; Wang, H. B.; Xiao, Y.; Rong, J. H. One-step preparation of nitrogen-doped graphene quantum dots from oxidized debris of graphene oxide. *J Mater Chem B* **2013**, *1*, 39-42.

(31) Jiang, D.; Chen, Y. P.; Li, N.; Li, W.; Wang, Z. G.; Zhu, J. L.; Zhang, H.; Liu, B.; Xu, S. Synthesis of Luminescent Graphene Quantum Dots with High Quantum Yield and Their Toxicity Study. *Plos One* **2015**, *10*.

(32) Wagner, C. D.; Riggs, W. M.; Davis, L. E.; Moulder, J. F.; Muilenberg, G. E.: *Handbook of X-Ray Photoelectron Spectroscopy: A Reference Book of Standard Data for Use in X-Ray Photoelectron Spectroscopy*; Perkin-Elmer Corp.: Eden Prairie, MN, 1979.

(33) He, G. Q.; Song, Y.; Liu, K.; Walter, A.; Chen, S.; Chen, S. W. Oxygen Reduction Catalyzed by Platinum Nanoparticles Supported on Graphene Quantum Dots. *Acs Catal* **2013**, *3*, 831-838.

(34) Song, Y.; Chen, S. W. Graphene Quantum-Dot-Supported Platinum Nanoparticles: Defect-Mediated Electrocatalytic Activity in Oxygen Reduction. *Acs Appl Mater Inter* **2014**, *6*, 14050-14060.

(35) Liu, K.; Song, Y.; Chen, S. W. Oxygen reduction catalyzed by nanocomposites based on graphene quantum dots-supported copper nanoparticles. *Int J Hydrogen Energ* **2016**, *41*, 1559-1567.

(36) Deming, C. P.; Mercado, R.; Gadiraju, V.; Sweeney, S. W.; Khan, M.; Chen, S. W. Graphene Quantum Dots-Supported Palladium Nanoparticles for Efficient Electrocatalytic Reduction of Oxygen in Alkaline Media. *Acs Sustain Chem Eng* **2015**, *3*, 3315-3323.

(37) Zhou, Y. C.; Leng, Y. H.; Zhou, W. J.; Huang, J. L.; Zhao, M. W.; Zhan, J.; Feng, C. H.; Tang, Z. H.; Chen, S. W.; Liu, H. Sulfur and nitrogen self-doped carbon nanosheets derived from peanut root nodules as high-efficiency non-metal electrocatalyst for hydrogen evolution reaction. *Nano Energy* **2015**, *16*, 357-366.

(38) Niu, W. H.; Li, L. G.; Liu, X. J.; Wang, N.; Liu, J.; Zhou, W. J.; Tang, Z. H.; Chen, S. W. Mesoporous N-Doped Carbons Prepared with Thermally Removable Nanoparticle Templates: An Efficient Electrocatalyst for Oxygen Reduction Reaction. *J Am Chem Soc* **2015**, *137*, 5555-5562.

(39) Liu, X. J.; Zhou, W. J.; Yang, L. J.; Li, L. G.; Zhang, Z. Y.; Ke, Y. T.; Chen, S. W. Nitrogen and sulfur co-doped porous carbon derived from human hair as

highly efficient metal-free electrocatalysts for hydrogen evolution reactions. *J Mater Chem A* **2015**, *3*, 8840-8846.

(40) Rensmo, H.; Westermark, K.; Sodergren, S.; Kohle, O.; Persson, P.; Lunell, S.; Siegbahn, H. XPS studies of Ru-polypyridine complexes for solar cell applications. *J Chem Phys* **1999**, *111*, 2744-2750.

(41) Haga, H.; Hong, H. G.; Shiozawa, Y.; Kawata, Y.; Monjushiro, H.; Fukuo, T.; Arakawa, R. Synthesis and proton-coupled electron-transfer reaction of self-assembled monolayers of a ruthenium(II) complex containing tridentate 2,6-bis(benzimidazol-2-yl)pyridine on a cold surface: Comparison of acid/base chemistry with bulk solution chemistry. *Inorg Chem* **2000**, *39*, 4566-4573.

(42) Liu, J. K.; Li, Q. Q.; Zou, Y.; Qian, Q. K.; Jin, Y. H.; Li, G. H.; Jiang, K. L.; Fan, S. S. The Dependence of Graphene Raman D-band on Carrier Density. *Nano Lett* **2013**, *13*, 6170-6175.

(43) Qu, D.; Zheng, M.; Du, P.; Zhou, Y.; Zhang, L. G.; Li, D.; Tan, H. Q.; Zhao, Z.; Xie, Z. G.; Sun, Z. C. Highly luminescent S, N co-doped graphene quantum dots with broad visible absorption bands for visible light photocatalysts. *Nanoscale* **2013**, *5*, 12272-12277.

(44) Binamirasoriaga, E.; Keder, N. L.; Kaska, W. C. Synthesis and Properties of Binuclear Ruthenium Complexes with 2,7-Bis(2-Pyridyl)-1,8-Naphthyridine (Bpnp) - X-Ray Crystal-Structure of [Ru2(Mu-O2cch3)3bpnp]Pf6. *Inorg Chem* **1990**, *29*, 3167-3171.

(45) Li, L. L.; Wu, G. H.; Yang, G. H.; Peng, J.; Zhao, J. W.; Zhu, J. J. Focusing on luminescent graphene quantum dots: current status and future perspectives. *Nanoscale* **2013**, *5*, 4015-4039.

(46) Jin, S. H.; Kim, D. H.; Jun, G. H.; Hong, S. H.; Jeon, S. Tuning the Photoluminescence of Graphene Quantum Dots through the Charge Transfer Effect of Functional Groups. *Acs Nano* **2013**, *7*, 1239-1245.

(47) Huang, H. D.; Liao, L.; Xu, X.; Zou, M. J.; Liu, F.; Li, N. The electron-transfer based interaction between transition metal ions and photoluminescent graphene quantum dots (GQDs): A platform for metal ion sensing. *Talanta* **2013**, *117*, 152-157.

(48) Kang, X. W.; Zuckerman, N. B.; Konopelski, J. P.; Chen, S. W. Alkyne-Stabilized Ruthenium Nanoparticles: Manipulation of Intraparticle Charge Delocalization by Nanoparticle Charge States. *Angew Chem Int Edit* **2010**, *49*, 9496-9499.

(49) Glover, S. D.; Kubiak, C. P. Persistence of the Three-State Description of Mixed Valency at the Localized-to-Delocalized Transition. *J Am Chem Soc* **2011**, *133*, 8721-8731.

(50) Chen, W.; Chen, S. W.; Ding, F. Z.; Wang, H. B.; Brown, L. E.; Konopelski, J. P. Nanoparticle-mediated intervalence transfer. *J Am Chem Soc* **2008**, *130*, 12156-12162.

(51) Hu, P. G.; Chen, L. M.; Deming, C. P.; Kang, X. W.; Chen, S. W. Nanoparticle-Mediated Intervalence Charge Transfer: Core-Size Effects. *Angew Chem Int Edit* **2016**, *55*, 1455-1459.

(52) Chen, L. M.; Song, Y.; Hu, P. G.; Deming, C. P.; Guo, Y.; Chen, S. W. Interfacial reactivity of ruthenium nanoparticles protected by ferrocenecarboxylates. *Phys Chem Chem Phys* **2014**, *16*, 18736-18742.

(53) Brunschwig, B. S.; Creutz, C.; Sutin, N. Optical transitions of symmetrical mixed-valence systems in the Class II-III transition regime. *Chem Soc Rev* **2002**, *31*, 168-184.

(54) D'Alessandro, D. M.; Keene, F. R. Intervalence charge transfer in a "chain-like" ruthenium trinuclear assembly based on the bridging ligand 4,7-phenanthrolino-5,6 : 5 ',6 '-pyrazine (ppz). *Dalton T* **2006**, 1060-1072.

(55) Callahan, R. W.; Keene, F. R.; Meyer, T. J.; Salmon, D. J. Intervalence Transfer and Electron-Transfer in Mixed-Valence Ion $[(Bpy)_2clru(Pyz)Rucl(Bpy)_2]^{3+}$. *J Am Chem Soc* **1977**, *99*, 1064-1073.

(56) Ebadi, M.; Lever, A. B. P. Ruthenium complexes of quinone related ligands: A study of the electrochemical properties of 2-aminothiophenolatobis(2,2 '-bipyridine)ruthenium(II). *Inorg Chem* **1999**, *38*, 467-474.

Chapter 6

Covalent Crosslinking of Graphene Quantum Dots by McMurry Deoxygenation Coupling

Reproduced with permission from (Limei Chen, Peiguang Hu, Jia En Lu, Shaowei Chen, "Covalent Crosslinking of Graphene Quantum Dots by McMurry Deoxygenation Coupling ", Chem. Asian J., 2017, 12, 973.) Copyright © 2017 Wiley-VCH Verlag GmbH & Co. KGaA, Weinheim.

6.1 Introduction

Graphene oxide (GO) nanosheets have been attracting extensive research interest due to their unique optical and electronic properties and potential applications in diverse areas such as optoelectronics, catalysis, energy generation and storage.[1-5] GO is generally prepared by chemical (oxidative) exfoliation of bulk graphite and carries a number of oxygenated functional groups such as carboxyl, carbonyl, hydroxyl, etc,[3] which render GO readily dispersible in water and polar organic media and may be exploited for the anchored deposition of metal and metal oxide nanoparticles forming functional nanocomposites.[6,7] Towards this end, it is critical to develop effective procedures for the controlled, "bottom-up" assembly of graphene derivatives into large, complicated architectures. In fact, ensembles of GO nanosheets have been prepared by employing molecular or metal templates, interfacial condensation driven by solvent evaporation at separated phases, and Langmuir-based techniques.[8-13] For instance, DNA molecules have been used for the controlled assembly of GO, and 3D GO networks have been formed on the metal surfaces (Zn, Fe, Cu, etc.) by a substrate-assisted reduction and assembly method.[8,11] GO thin films have also been prepared at the dimethyl formamide/air interface, while a honeycomb film is formed on a glass slide by the self-assembly of dimethyldioctadecylammonium bromide-modified GO.[9,14] Large transparent conducting films have also been produced by Langmuir–Blodgett assembly of small graphene sheets in a layer-by-layer manner.[10] In these earlier studies, GO nanosheets were assembled into different architectures mostly through noncovalent interactions such as electrostatic or van der Waals interactions.

One immediate question arises. Is it possible to covalently crosslink GO nanosheets such that mechanically robust ensembles may be produced? This is the primary motivation of the present study, where controlled assembly of graphene quantum dots (GQDs) is achieved by exploiting the unique chemical reactivity of the GQD peripheral oxygenated species.[15] Specifically, GQDs are covalently crosslinked by C=C bonds formed by McMurry deoxygenation coupling of the GQD peripheral carbonyl groups.[16]

In the McMurry reaction, aldehydes and ketones are reduced by low-valence titanium compounds in THF or 1,4-dioxane to afford pinacols and/or olefins in high yields; and refluxing at elevated temperatures leads to effective deoxygenation of the reactant molecules to produce olefins (up to 98 % yield).[17] For instance, two 2-methyl-2,3-dihydro-1*H*-cyclopenta[a]naphthalen-1-one molecules have been coupled to produce the corresponding alkene by thermal refluxing in THF in the presence of $TiCl_4$ and Zn powders.[18]

Notably, GQDs prepared by acid exfoliation of graphite precursors are rich of oxygen-containing functional groups at the surfaces and edges,[3] where the carbonyl groups may be exploited as the active sites for McMurry coupling between GQDs. Herein, 3D networks of GQDs were obtained via covalent coupling by thermal refluxing in THF with $TiCl_4$ and Zn powders as the catalysts (Scheme 6.1). The structures of the resulting GQD ensembles were carefully examined by various microscopic and spectroscopic measurements.

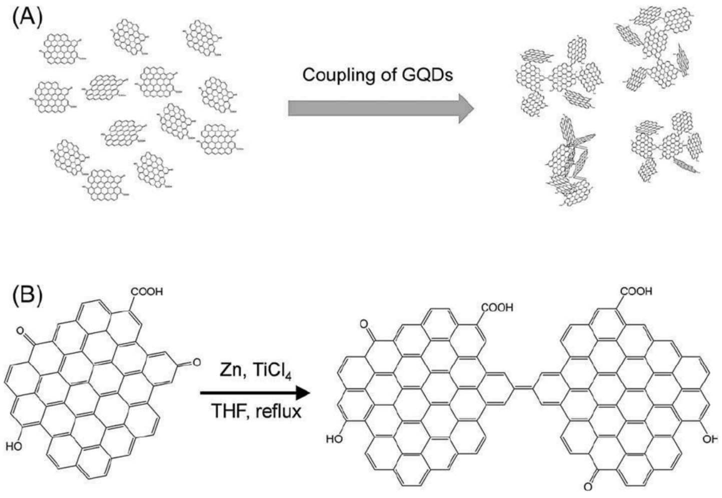

Scheme 6.1 (A) covalent crosslinking of GQDs by (B) McMurry deoxygenation coupling reaction.

6.2 Experimental Section

Chemicals

Pitch carbon fibers (Fiber Glast Development Corporation), sodium hydroxide (NaOH, Fisher Scientific), sodium carbonate (Na_2CO_3, Fisher Scientific), hydrochloric acid (HCl, Fisher Scientific), sulfuric acid (H_2SO_4, Fisher Scientific), nitric acid (HNO_3, Fisher Scientific), tetrahydrofuran (THF, 99.99%, Fisher Scientific), zinc powder (Zn, 98%, Fisher Science Education), and titanium(IV) chloride ($TiCl_4$, 99.9%, ACROS) were all used as received. Water was supplied by a Barnstead Nanopure water system (18.3 MΩ cm).

Synthesis of GQDs

GQDs were synthesized by chemical exfoliation of carbon pitch fibers in concentrated acids.[6,19] Experimentally, carbon pitch fibers (0.3 g) were added to a mixture of concentrated HNO_3 (20 mL) and H_2SO_4 (60 mL) in a round-bottom flask and sonicated for 2 h to allow for dispersion of the carbon fibers. The solution was then thermally refluxing at 100 °C for 24 h. After cooling down to room temperature, the solution was neutralized with dilute NaOH and Na_2CO_3 solutions. The mixture was then placed in a dialysis bag in Nanopure water for 3 d, affording GQDs as the final product after rotary evaporation, which were dispersible in both water and THF.

GQDs coupling

In a typical coupling reaction,[17] 57 μL of $TiCl_4$ was slowly added to 67 mg of zinc powders in 6 mL of THF in a 50 mL of flask under magnetic stirring in an ice bath. The flask was then transferred to an oil bath and refluxed at 66 °C for 2 h, when a black slurry was obtained in THF. 30 mg of GQDs in 1 mL of THF was then added into the flask, and after magnetic stirring for 24 h, the product was collected by centrifugation and washed with a copious amount of THF, rinsed with aqua regia, and dialyzed in water for 3 d. The final product was denoted as GQDs-CH. A second reaction was carried out in the same manner except that the amounts of Zn powders and $TiCl_4$ added were reduced by half, and the corresponding product was referred to as GQD-CL. Both of these two samples were dispersible in water, but barely in THF.

Characterization.

The morphology and size of GQDs before and after coupling were characterized by atomic force microscopic (AFM, Molecular Imaging PicoLE SPM instrument), dynamic light scattering (DLS, Protein Solution Dynapro temperature controlled microsampler) and transmission electron microscopic (TEM, Philips CM300 at 300 kV) studies. FTIR spectra were obtained with a PerkinElmer FTIR spectrometer (Spectrum One, spectral resolution 4 cm^{-1}) where the samples were prepared by casting the sample solutions onto a ZnSe disk. Raman spectra were acquired with a Delta NU 532 nm Raman spectrometer. X-ray photoelectron spectra (XPS) were recorded with a PHI 5400/XPS instrument equipped with an Al Kα source operated at 350 W and 10^{-9} Torr, where silicon wafers were sputtered by argon ions to remove carbon from the background and used as substrates. The spectra were referenced to the Si 2p peak at 99.03 eV.

6.3 Results and Discussion

Experimentally, GQDs were prepared by acid exfoliation of the nanometer-sized sp^2domains in pitch carbon fibers (see the Supporting Information for details).[3] The obtained GQDs were decorated with various oxygenated species, such as epoxy and carbonyl groups, and are readily dispersible in water and polar organic media.[20] Figure 6.1(A) depicts a representative TEM image of the as-prepared GQDs, where individual GQDs can be easily recognized, consistent with the good dispersity of the GQDs in water. Statistical analysis based on more than 100 GQDs showed that the GQDs exhibited a narrow size distribution, with the majority of the GQDs within the size range of 3.0 to 5.0nm and an average diameter of 4.3±1.2nm, as depicted in the inset. Figure 6.1(B) shows the corresponding high-resolution TEM image where well-defined lattice fringes can be seen with a lattice spacing of 0.21 nm, in good agreement with the interplanar distance of carbon (1100).[21]

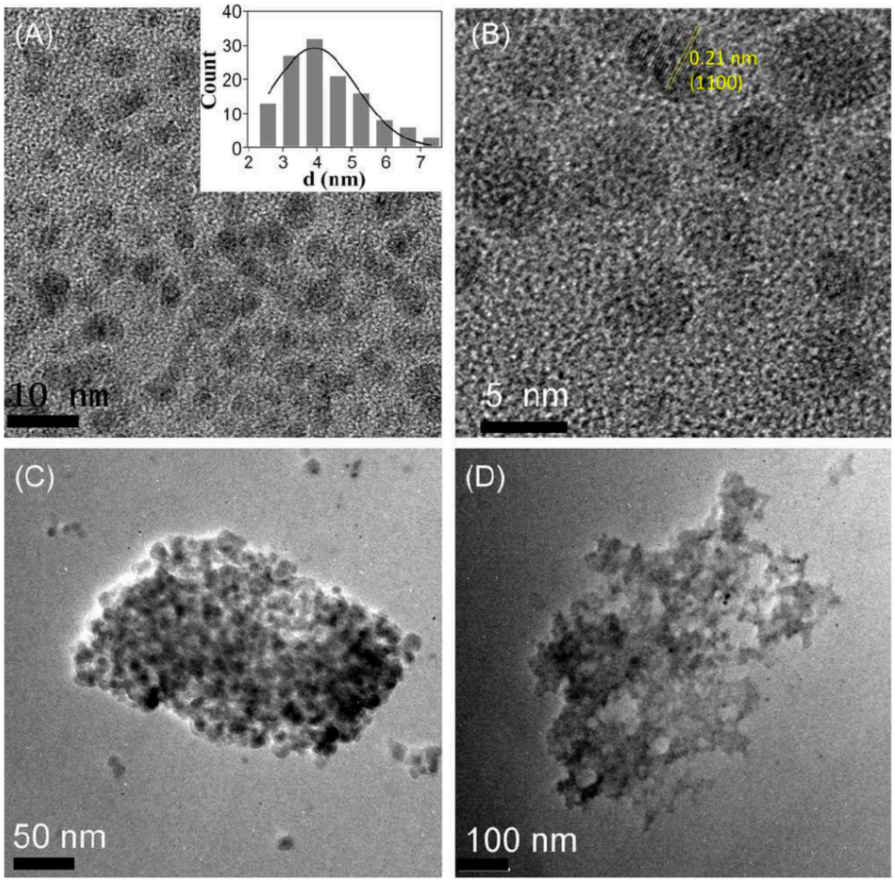

Figure 6.1 (A)TEM images of GQDs as synthesized from carbon fibers. Inset: size distribution of GQDs. (B)HRTEM of GQDs. TEM images of (C)GQDs-CL and (D)GQDs-CH.

Remarkably, after McMurry deoxygenation coupling catalyzed by $TiCl_4$ and zinc in refluxing THF,[16-18] significant crosslinking of GQDs occurred. Two samples were prepared, GQDs-CH and GQDs-CL, where the amount of $TiCl_4$ and zinc added was twice as much in the former as in the latter (see the Supporting Information for details). Both samples remained dispersible in water, but barely in THF. From Figure 6.1(C), one can see that the GQDs-CL sample exhibited the formation of ensembles up to 300 nm across, and even larger agglomerates can be found with the GQDs-CH sample (ca. 600 nm in size, Figure 6.1 (D)). These observations suggest effective covalent crosslinking of GQDs by the McMurry deoxygenation coupling reaction (Scheme 6.1(A)).[5] In this reaction, Ti^{IV} was reduced by metallic Zn to produce low-valence titanium (Ti^{II} or Ti^{III}) which served as catalysts to facilitate the deoxygenation of the GQD carbonyl groups and subsequent covalent coupling between the GQDs (Scheme 6.1 (B)).

AFM and dynamic light scattering (DLS) measurements further confirmed the coupling of GQDs by McMurry deoxygenation. Figure 6.2 depicts the representative AFM topographs of the (A_1) as-prepared GQDs, (B_1) GQDs-CL, and (C_1) GQDs-CH, where individual GQDs and crosslinked ensembles can be readily resolved. Again, this is consistent with the good dispersity of the samples in water. The corresponding line scan profiles were included in panels (A_2), (B_2), and (C_2). One can see that the thickness of the samples increased markedly in the order of as-prepared GQDs<GQDs-CL<GQDs-CH. In fact, from the height histogram (Figure 6.2 (A_3)), the height of the as-prepared GQDs was mostly in the range of 0.6 to 1.2 nm, with an average of 1.0±0.4 nm, corresponding to 1 to 4 graphene layers.[3] In contrast, the heights of both GQDs-CL and GQDs-CH were markedly greater at 5.0±2.8 nm (Figure 6.2 (B_3)) and 17.2±10.5 nm (Figure 6.2 (C_3)), respectively. That is, with the addition of an increasing amount of coupling reagents, the size of the GQD ensembles increased accordingly, consistent with the TEM results in Figure 6.1. A similar variation was observed in DLS measurements, where the average hydrodynamic radius (R_H) in water of the as-

prepared GQDs was estimated to be 20.7nm, which increased drastically to 57.8 nm for GQDs-CL and 237.2 nm for GQDs-CH.

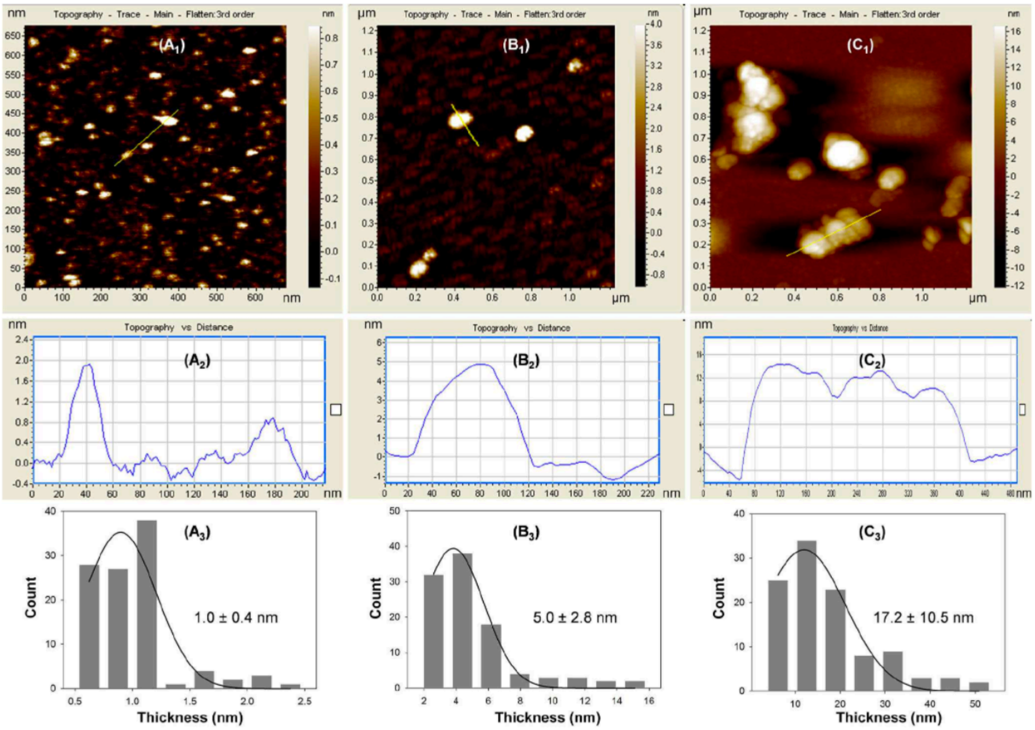

Figure 6.2 Representative AFM topographs, line scans and height distributions of (A_1–A_3) GQDs, (B_1–B_3) GQDs-CL, and (C_1-C_3) GQDs-CH.

The chemical structures of the GQDs before and after McMurry coupling were further examined by FTIR measurements. From Figure 6.3, one can see that the as-prepared GQDs (black curve) exhibited multiple characteristic peaks at 3428 cm^{-1} (O−H stretch), 1738 cm^{-1} (C=O stretch), 1620 cm^{-1} (aromatic C=C stretch), 1405 cm^{-1} (symmetrical stretch of O-H in COOH), and 1197 and 1046 cm^{-1} (C-O-C vibrations).[22-25] This strongly indicates the formation of oxygen-containing functional groups such as hydroxyl, carbonyl, carboxyl and epoxy groups in GQDs.[22] After deoxygenation coupling, whereas these vibrational bands remained visible, the intensity of the oxygenated moieties decreased significantly with respect to that of the C=C vibration. For instance, the relative intensity of the C=O vibrational band at 1738 cm^{-1} to that of aromatic C=C vibration at 1620 cm^{-1} was reduced by 40 % for GQDs-CL and 74 % for GQDs-CH, as compared to that of the as-prepared GQDs. This is consistent with the effective removal of the C=O groups in McMurry deoxygenation coupling which was facilitated by increasing loading of the coupling catalysts.

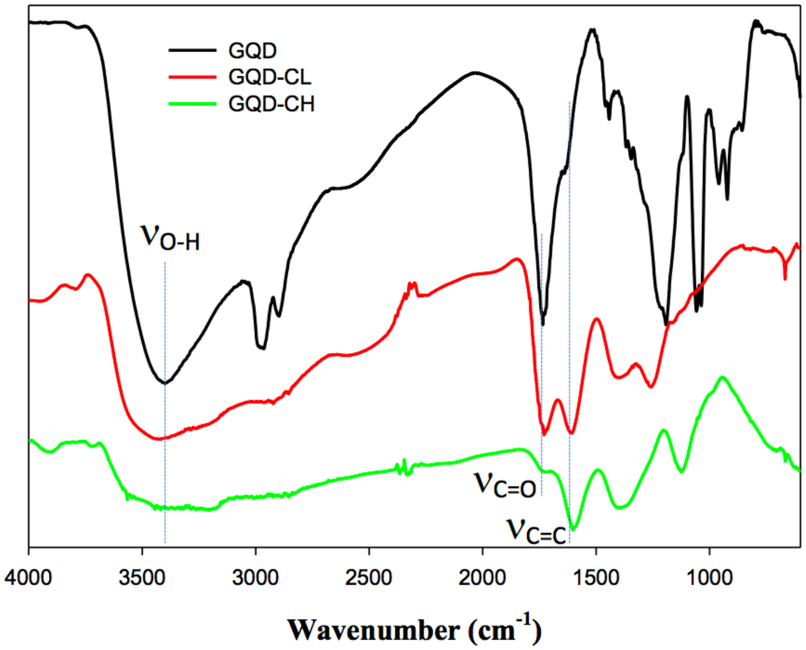

Figure 6.3 FTIR spectra of as-prepared GQDs, GQDs-CL and GQDs-CH.

More quantitative analysis was carried out with XPS measurements. From the survey spectra in Figure 6.4, one can see that the as-prepared GQDs, GQDs-CL and GQDs-CH samples all exhibited only two major peaks at around 285 and 532 eV, corresponding to the binding energies of C 1s and O 1s electrons, respectively. The high-resolution scans of the C 1s electrons are depicted in Figure 6.5 (A_1, B_1, C_1). From Figure 6.5 (A_1), it can be seen that the C 1s spectrum of the as-prepared GQDs can be deconvoluted into three subpeaks at 284.5 eV, 285.5 eV, and 287.7 eV, which may be assigned to sp^2-hybridized carbon (C=C), sp^3-hybridized C (C−O) and carbon in C=O, respectively.[26] This indicates that the GQDs were indeed functionalized with a number of oxygenated species, as suggested by FTIR measurements (Figure 6.3). For the GQDs-CL (Figure 6.5 (B_1)) and GQDs-CH (Figure 6.5 (C_1)) samples, deconvolution of the C 1s spectra also yielded three subpeaks at similar binding energies. However, the concentration of the oxidized carbon (C=O) varied markedly from GQDs to GQDs-CL and GQDs-CH, based on the integrated peak areas. For instance, C=O accounted for 15.3 % of the carbon atoms in the as-prepared GQDs, but only 9.8 % in GQDs-CL and 6.2 % in GQDs-CH; and concurrently, the fraction of sp^2 C increased from 61.3 % in GQDs to 64.3 % in GQDs-CL and 71.9 % in GQDs-CH (whereas the contents of sp^3 carbons remained almost invariant at 23.5 % for GQDs, 25.8 % for GQDs-CL, and 21.8 % for GQDs-CH). Moreover, the C:O mole ratio increased from 6.5 for as-prepared GQDs to 10.2 for GQDs-CL and 16.1 for GQDs-CH. These results are highly consistent with McMurry deoxygenation of the carbonyl moieties and the subsequent formation of C=C covalent linkages that crosslinked GQDs.[18]

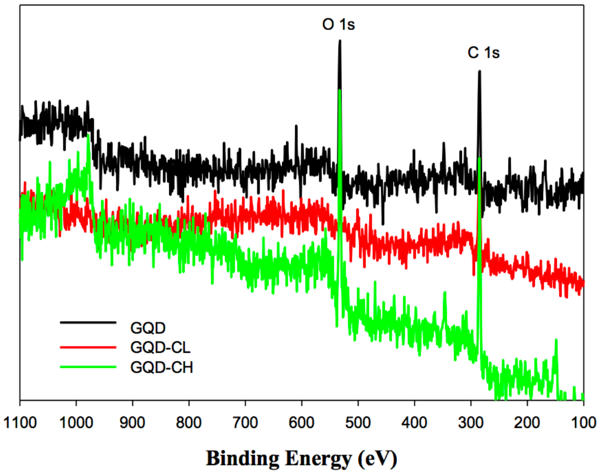

Figure 6.4 XPS survey spectra of as-prepared GQDs, GQDs-CL and GQDs-CH, where O 1s and C 1s electrons are well-defined in all three samples and no other elements such as Ti (2p, ca. 459.5 eV), Zn (2p, ca. 1021 eV), and Cl (2p, ca. 198 eV) can be seen.

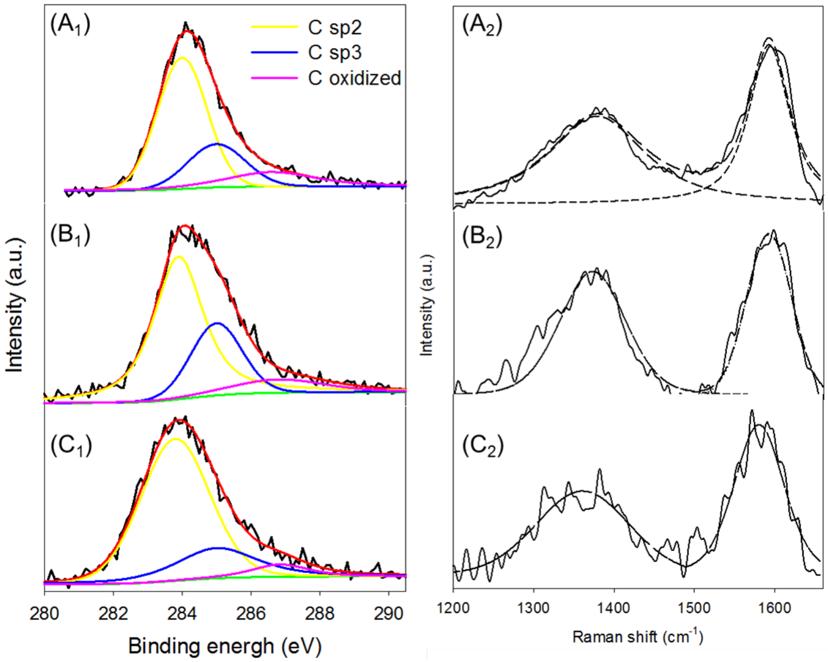

Figure 6.5 High-resolution XPS scans of the C 1s electrons in (A$_1$) as-prepared GQDs, (B$_1$) GQDs-CL, and (C$_1$) GQDs-CH. Black curves are experimental data and colored curves are deconvolution fits and corresponding Raman data (A$_2$, B$_2$, C$_2$).

Consistent results were obtained in Raman measurements. As shown in Figure 6.5 (A_2), the three GQDs samples all exhibited a D band at 1351 cm^{-1} and a G band at 1578 cm^{-1}, [22,26,27] and the ratio of the two band intensities (I_D/I_G) was found to decrease from 1.44 for GQDs to 1.26 for GQDs-CL and 0.94 for GQDs-CH, due to the removal of the oxidized carbons (defects) from the GQD molecular skeletons.

Interestingly, the photoluminescence properties of the GQDs also varied after chemical coupling. For instance, as depicted in Figure 6.6 (B), whereas both the as-produced GQDs and GQDs-CL exhibited a major excitation peak (λ_{ex}) at 368 nm and a corresponding emission peak (λ_{em}) at 550 nm, λ_{ex} and λ_{em} blue-shifted to 360 and 518 nm, respectively, for GQDs-CH. In addition, the photoluminescence intensity (normalized to respective absorbance at the excitation wavelength, Figure 6.6 (A)) was markedly enhanced with GQDs-CH as compared to those of as-produced GQDs and GQDs-CL. This, again, is consistent with the removal of oxygenated species on the GQD surface where quinone-like species are known to be effective electron acceptors and emission quenchers.[28] A similar blue-shift of the peak position of photoluminescence emission and enhanced emission intensity has also been observed with GQDs reduced by sodium borohydride, which is ascribed to the removal of carbonyl and epoxy groups from the GQD surface.[22,29]

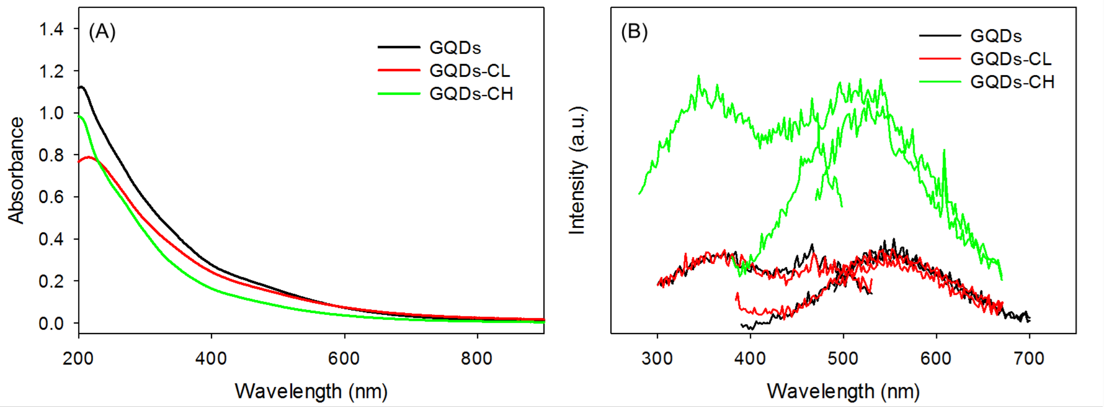

Figure 6.6 (A) UV-Vis and (B)Excitation and emission of spectra of as-produced GQDs, GQDs-CL, and GQDs-CH in water. The photoluminescence intensity has been normalized to the respective absorbance at the excitation position.

6.4 Conclusion

In summary, a facile method was developed to covalently crosslink small GQDs of less than 10 nm into large superstructures of hundreds of nanometers in size by taking advantage of the McMurry deoxygenation reaction for the conversion of ketones or aldehydes to olefins. Specifically, GQDs prepared by acid exfoliation of carbon fibers were readily dispersed both in water and THF, and the peripheral carbonyl moieties provide the active sites for GQD covalent crosslinking catalyzed by $TiCl_4$ and Zn, as manifested in various microscopic and spectroscopic measurements. The results may be exploited as a generic, effective strategy for controllable assembly of graphene oxide and derivatives into more complicated functional architectures.

6.5 References

(1) Yoon, T.; Kim, J. H.; Choi, J. H.; Jung, D. Y.; Park, I. J.; Choi, S. Y.; Cho, N. S.; Lee, J. I.; Kwon, Y. D.; Cho, S.; Kim, T. S. Healing Graphene Defects Using Selective Electrochemical Deposition: Toward Flexible and Stretchable Devices. *Acs Nano* **2016**, *10*, 1539-1545.

(2) Novoselov, K. S.; Fal'ko, V. I.; Colombo, L.; Gellert, P. R.; Schwab, M. G.; Kim, K. A roadmap for graphene. *Nature* **2012**, *490*, 192-200.

(3) Peng, J.; Gao, W.; Gupta, B. K.; Liu, Z.; Romero-Aburto, R.; Ge, L. H.; Song, L.; Alemany, L. B.; Zhan, X. B.; Gao, G. H.; Vithayathil, S. A.; Kaipparettu, B. A.; Marti, A. A.; Hayashi, T.; Zhu, J. J.; Ajayan, P. M. Graphene Quantum Dots Derived from Carbon Fibers. *Nano Lett* **2012**, *12*, 844-849.

(4) Wen, J.; Xu, Y. Q.; Li, H. J.; Lu, A. P.; Sun, S. G. Recent applications of carbon nanomaterials in fluorescence biosensing and bioimaging. *Chem Commun* **2015**, *51*, 11346-11358.

(5) Li, F. H.; Gan, S. Y.; Han, D. X.; Niu, L. Graphene-Based Nanohybrids for Advanced Electrochemical Sensing. *Electroanal* **2015**, *27*, 2098-2115.

(6) Song, Y.; Chen, S. W. Graphene Quantum-Dot-Supported Platinum Nanoparticles: Defect-Mediated Electrocatalytic Activity in Oxygen Reduction. *Acs Appl Mater Inter* **2014**, *6*, 14050-14060.

(7) Pan, D. Y.; Jiao, J. K.; Li, Z.; Guo, Y. T.; Feng, C. Q.; Liu, Y.; Wang, L.; Wu, M. H. Efficient Separation of Electron-Hole Pairs in Graphene Quantum Dots

by TiO2 Heterojunctions for Dye Degradation. *Acs Sustain Chem Eng* **2015**, *3*, 2405-2413.

(8) Tang, L. H.; Wang, Y.; Liu, Y.; Li, J. H. DNA-Directed Self-Assembly of Graphene Oxide with Applications to Ultrasensitive Oligonucleotide Assay. *Acs Nano* **2011**, *5*, 3817-3822.

(9) Bai, Y. F.; Zhang, Y. F.; Zhou, A. W.; Li, H. W.; Zhang, Y.; Luong, J. H. T.; Cui, H. F. Self-assembly of a thin highly reduced graphene oxide film and its high electrocatalytic activity. *Nanotechnology* **2014**, *25*.

(10) Li, X. L.; Zhang, G. Y.; Bai, X. D.; Sun, X. M.; Wang, X. R.; Wang, E.; Dai, H. J. Highly conducting graphene sheets and Langmuir-Blodgett films. *Nat Nanotechnol* **2008**, *3*, 538-542.

(11) Hu, C. G.; Zhai, X. Q.; Liu, L. L.; Zhao, Y.; Jiang, L.; Qu, L. T. Spontaneous Reduction and Assembly of Graphene oxide into Three-Dimensional Graphene Network on Arbitrary Conductive Substrates. *Scientific reports* **2013**, *3,* 2065.

(12) Ardini, M.; Golia, G.; Passaretti, P.; Cimini, A.; Pitari, G.; Giansanti, F.; Di Leandro, L.; Ottaviano, L.; Perrozzi, F.; Santucci, S.; Morandi, V.; Ortolani, L.; Christian, M.; Treossi, E.; Palermo, V.; Angelucci, F.; Ippoliti, R. Supramolecular self-assembly of graphene oxide and metal nanoparticles into stacked multilayers by means of a multitasking protein ring. *Nanoscale* **2016**, *8*, 6739-6753.

(13) Zeng, M. Q.; Wang, L. X.; Liu, J. X.; Zhang, T.; Xue, H. F.; Xiao, Y.; Qin, Z. H.; Fu, L. Self-Assembly of Graphene Single Crystals with Uniform Size and Orientation: The First 2D Super-Ordered Structure. *J Am Chem Soc* **2016**, *138*, 7812-7815.

(14) Yin, S. Y.; Zhang, Y. Y.; Kong, J. H.; Zou, C. J.; Li, C. M.; Lu, X. H.; Ma, J.; Boey, F. Y. C.; Chen, X. D. Assembly of Graphene Sheets into Hierarchical Structures for High-Performance Energy Storage. *Acs Nano* **2011**, *5*, 3831-3838.

(15) Georgakilas, V.; Otyepka, M.; Bourlinos, A. B.; Chandra, V.; Kim, N.; Kemp, K. C.; Hobza, P.; Zboril, R.; Kim, K. S. Functionalization of Graphene: Covalent and Non-Covalent Approaches, Derivatives and Applications. *Chem Rev* **2012**, *112*, 6156-6214.

(16) Mc Murry, J. E.; Fleming, M. P. A new method for the reductive coupling of carbonyls to olefins. Synthesis of beta-carotene. *J Am Chem Soc* **1974**, *96*, 4708-4709.

(17) Mukaiyama, T.; Sato, T.; Hanna, J. Reductive Coupling of Carbonyl-Compounds to Pinacols and Olefins by Using Ticl4 and Zn. *Chem Lett* **1973**, 1041-1044.

(18) ter Wiel, M. K. J.; van Delden, R. A.; Meetsma, A.; Feringa, B. L. Increased speed of rotation for the smallest light-driven molecular motor. *J Am Chem Soc* **2003**, *125*, 15076-15086.

(19) He, G. Q.; Song, Y.; Liu, K.; Walter, A.; Chen, S.; Chen, S. W. Oxygen Reduction Catalyzed by Platinum Nanoparticles Supported on Graphene Quantum Dots. *Acs Catal* **2013**, *3*, 831-838.

(20) Li, Z. Y.; Zhang, W. H.; Luo, Y.; Yang, J. L.; Hou, J. G. How Graphene Is Cut upon Oxidation? *J Am Chem Soc* **2009**, *131*, 6320-+.

(21) Ananthanarayanan, A.; Wang, X. W.; Routh, P.; Sana, B.; Lim, S.; Kim, D. H.; Lim, K. H.; Li, J.; Chen, P. Facile Synthesis of Graphene Quantum Dots from 3D Graphene and their Application for Fe^{3+}Sensing. *Adv Funct Mater* **2014**, *24*, 3021-3026.

(22) Zhang, W. K.; Liu, Y. Q.; Meng, X. R.; Ding, T.; Xu, Y. Q.; Xu, H.; Ren, Y. R.; Liu, B. Y.; Huang, J. J.; Yang, J. H.; Fang, X. M. Graphenol defects induced blue emission enhancement in chemically reduced graphene quantum dots. *Phys Chem Chem Phys* **2015**, *17*, 22361-22366.

(23) Yang, H. B.; Dong, Y. Q.; Wang, X. Z.; Khoo, S. Y.; Liu, B. Cesium Carbonate Functionalized Graphene Quantum Dots as Stable Electron-Selective Layer for Improvement of Inverted Polymer Solar Cells. *Acs Appl Mater Inter* **2014**, *6*, 1092-1099.

(24) Achadu, O. J.; Nyokong, T. Application of graphene quantum dots decorated with TEMPO-derivatized zinc phthalocyanine as novel nanoprobes: probing the sensitive detection of ascorbic acid. *New J Chem* **2016**, *40*, 8727-8736.

(25) Lin, L.; Zhang, S. Creating high yield water soluble luminescent graphene quantum dots via exfoliating and disintegrating carbon nanotubes and graphite flakes. *Chem commun* **2012**, *48*, 10177-10179.

(26) Qu, D.; Zheng, M.; Zhang, L.; Zhao, H.; Xie, Z.; Jing, X.; Haddad, R. E.; Fan, H.; Sun, Z. Formation mechanism and optimization of highly luminescent N-doped graphene quantum dots. *Scientific reports* **2014**, *4*, 5294.

(27) Chen, L. M.; Hu, P. G.; Deming, C. P.; Wang, N.; Lu, J. E.; Chen, S. W. Intervalence Charge Transfer of Ruthenium-Nitrogen Moieties Embedded within Nitrogen-Doped Graphene Quantum Dots. *J Phys Chem C* **2016**, *120*, 13303-13309.

(28) Tian, L.; Song, Y.; Chang, X. J.; Chen, S. W. Hydrothermally enhanced photoluminescence of carbon nanoparticles. *Scripta Mater* **2010**, *62*, 883-886.

(29) Zhu, S. J.; Song, Y. B.; Zhao, X. H.; Shao, J. R.; Zhang, J. H.; Yang, B. The photoluminescence mechanism in carbon dots (graphene quantum dots, carbon nanodots, and polymer dots): current state and future perspective. *Nano Res* **2015**, *8*, 355-381.

Chapter 7

Gold core@silver semishell Janus nanoparticles prepared by interfacial etching

Reproduced with permission from (Limei Chen, Christopher P. Deming, Yi Peng , Peiguang Hu, Jake Stofan and Shaowei Chen, "Gold core@silver semishell Janus nanoparticles prepared by interfacial etching", Nanoscale, 2016, 8, 14565.) Copyright © 2016 The Royal Society of Chemistry.

7.1 Introduction

Transition-metal nanoparticles have been attracting significant attention in diverse research fields, such as (bio)chemical sensing, multifunctional catalysis, and drug delivery, primarily because of their rich chemical functionality.[1-5] These nanoparticles are generally formed with a symmetrical shape and composition because of minimization of surface energy; yet, in the quest for "smart" materials that may be exploited for directional engineering and functionalization, structurally asymmetrical Janus nanoparticles have emerged as a unique, new member of the family of functional nanomaterials.[6-10] For instance, Janus nanoparticles have been prepared based on metal–metal oxide heterodimer composites such as Au–SiO_2, Au–TiO_2 and Au–Fe_3O_4 nanoparticles.[11-13] Of these, Au–TiO_2 snowman-like Janus nanoparticles have been fabricated by directional growth of TiO_2 nanoparticles on gold Janus nanoparticles where one hemisphere is capped with hydrophilic ligands and the other hydrophobic, and the resulting heterodimers show apparent photocatalytic activity towards methanol oxidation to formaldehyde, due to enhanced charge separation of TiO_2 under photoirradiation by the gold nanoparticles, as compared to TiO_2 colloids alone.[12] Bimetallic Janus nanoparticles have also been prepared by asymmetric deposition of a second metal onto the surface of the core materials, forming a dumb bell or acorn-like structure, or by asymmetrical etching of the shell metal, forming metal-tipped nanorods.[14-16] For instance, dumbbell-like Ag-tipped Au nanorods have been prepared by lateral etching of core–shell Au@Ag nanorods and have shown improved catalytic activity for the reduction of *p*-nitrophenol due to their specific structure and ligand effect, as compared to the original nanorods.[15] Another method is based on galvanic exchange reactions whereby partial replacement of the original core metal with a second metal is carried out under strict spatial control.[17,18] In another study, AgPd and AuPd dimer nanostructures are prepared by kinetically controlled nucleation and growth of Ag or Au on only one facet of cubic Pd nanocrystals by manipulation of various parameters such as injection rate and capping ligands.[19] Such bimetallic structures endow the nanoparticles with unique optical and electronic properties, as well as electrocatalytic activity towards, for instance, the oxygen reduction reaction (ORR), a critical reaction in fuel cell electrochemistry, as compared to their monometallic counterparts.[20,21] In fact, in a previous study,[18] we prepared bimetallic AgAu Janus nanoparticles by galvanic exchange reactions of silver nanoparticles with a gold(I)–thiolate complex at the air/water interface, and the obtained Janus nanoparticles exhibited higher ORR activity than the original Ag nanoparticles, due to polarized distributions of electrons within the nanoparticles as a result of partial charge transfer from Ag to Au, although the Au content was only 5 at%. In such bimetallic nanoparticles, additional contributions to enhanced ORR activity may arise from surface strain that facilitate oxygen adsorption onto the shell metal.[5,22] More complicated trimetallic Neapolitan nanoparticles have also been prepared by two sequential interfacial galvanic exchange reactions.[23]

In the present study, using Au@Ag core–shell nanoparticles as the starting materials, we prepared Au@Ag semishell Janus nanoparticles by selective chemical etching of part of the silver shell. The Au@Ag core–shell nanoparticles were produced by growing a silver shell onto gold seed nanoparticles and capping by 1-dodecanethiol. When a nanoparticle monolayer was formed on the water surface of a Langmuir–Blodgett trough, a mixture of

H_2O_2 and NH_3 was injected to the water subphase to selectively etch off the bottom half of the silver shells, leading to the formation of Au@Ag semishell Janus nanoparticles. The asymmetrical structure of the resulting nanoparticles was characterized by a variety of microscopy and spectroscopy measurements. Interestingly, the semishell Janus nanoparticles exhibited enhanced electrocatalytic activity in ORR, as compared with the original core–shell nanoparticles, suggesting that interfacial engineering provided an effective way to manipulate and optimize the nanoparticle electronic properties and hence catalytic performance.

7.2 Experimental Section

Chemicals

Hydrogen tetrachloroauric acid ($HAuCl_4 \cdot xH_2O$) was synthesized by dissolving ultrahigh-purity gold (99.999%, Johnson Matthey) in freshly prepared aqua regia followed by crystallization. Silver nitrate ($AgNO_3$, Fisher Scientific), sodium borohydride ($NaBH_4$, ≥98%, Acros), sodium citrate dihydrate ($Na_3C_6H_5O_7 \cdot 2H_2O$, Fisher Scientific), sodium hydroxide anhydrous (NaOH, Fisher Scientific), L-ascorbic acid (ACS grade, Amresco), hydrogen peroxide (H_2O_2, 30% solution, Fisher Scientific), strong ammonia solution (NH_3, Fisher Scientific), 1-dodecanethiol ($CH_3(CH_2)_{11}SH$, 96%, Acros), and acetic acid (HOAc, Glacial, Fisher Scientific) were all used as received without any further purification. Solvents were purchased at the highest purity available from typical commercial sources and also used as received. Water was supplied by a Barnstead Nanopure water system (18.3 MΩ cm).

Synthesis of Au@Ag core–shell nanoparticles

In a typical synthesis, citrate-stabilized gold colloids of *ca*. 5 nm in diameter were prepared and used as the seed nanoparticles.[24] Experimentally, 0.05 mmol of $HAuCl_4$ and 0.05 mmol of sodium citrate were dissolved into 100 mL of H_2O at room temperature under magnetic stirring, into which was added dropwise 5 mL of an ice-cold, freshly made solution of 100 mM $NaBH_4$. The appearance of a dark red color signified the formation of gold colloids in the solution. Into this seed solution was then added 5 mL of an aqueous solution containing 0.5 mmol of ascorbic acid and 0.625 mmol of NaOH, followed by the slow addition of 10 mL of a 10 mM $AgNO_3$ (0.1 mmol) solution over the course of 2 h.[25] The color of the solution was found to change from red to orange and finally to brown, due to the formation of Au@Ag core–shell nanoparticles. To cap the resulting nanoparticles with 1-dodecanethiol, in a typical experiment, 3 mL of the as-prepared core–shell nanoparticle solution was placed in a glass vial, into which was added 50 μL of HOAc. 1 mL of a $CHCl_3$ solution containing 50 μL of 1-dodecanethiol was then added to the vial and the vial was shaken for about 3 min, and the nanoparticles were found to transfer to the $CHCl_3$ phase.[26] The organic phase was collected and dried by rotary evaporation and the obtained solids were rinsed with a copious amount of methanol to remove excess thiol ligands, affording purified 1-dodecanethiol-capped Au@Ag core–shell nanoparticles.

1-Dodecanethiol-capped Ag@Au core–shell nanoparticles were prepared in a similar fashion except that silver colloids were first prepared and used as seed particles onto which a gold shell was grown from $HAuCl_4$. The presence of NaOH (solution pH > 10.8) inhibited the galvanic replacement of Ag colloids by Au(III) and facilitated the deposition of a gold shell onto the Ag surface, leading to the formation of Ag@Au core–shell nanoparticles.[27]

Preparation of Au@Ag semishell Janus nanoparticles

Au@Ag semishell Janus nanoparticles were prepared by etching off part of the silver shell from the Au@Ag core–shell nanoparticles using a H_2O_2 + NH_3 (1 : 1 mole ratio) water solution.[23,28] In brief, the monolayer of 1-dodecanethiol-capped Au@Ag core–shell nanoparticles prepared above was deposited onto the water surface of a Langmuir–Blodgett trough (NIMA Technology, model 611D). The particle monolayer was then compressed to a desired surface pressure where the interparticle edge-to-edge separation was maintained at a value smaller than twice the extended ligand chain length such that the interfacial mobility of the particles was impeded. At this point, a calculated amount of the H_2O_2 + NH_3 aqueous solution was injected into the water subphase by a Hamilton microliter syringe, where the silver shells in direct contact with water were etched away, leading to the formation of Au@Ag semi-shell Janus nanoparticles. The nanoparticles were then collected for further characterization.

Structural characterization

UV-vis absorption spectra were collected with a PerkinElmer Lambda 35 spectrometer using a 1 cm quartz cuvette. X-ray photoelectron spectra (XPS) were recorded with a PHI 5400/XPS instrument equipped with an Al K_α source operated at 350 W and 10^{-9} Torr. The morphology and sizes of the nanoparticles were characterized by transmission electron microscopy (TEM, Philips CM200 at 200 kV) studies. At least 100 nanoparticles were measured to obtain a size distribution. For inductively coupled plasma mass spectrometry (ICP-MS, PerkinElmer Optima 4300DV) measurements, about 25 μg of the nanoparticles prepared above were dissolved in 1 mL of freshly made aqua regia. The solution was then diluted by nanopure water to 15 mL. Standard solutions of metal ions were made at a concentration of 0.5 μg mL^{-1} Ag^+ and 1.0 μg mL^{-1} Au^{3+} with aqua regia of the same concentration.

Electrochemistry

Electrochemical studies were carried out in a standard three-electrode cell connected to a CHI-710 electrochemical workstation, with a Pt foil counter electrode and a reversible hydrogen electrode (RHE) at room temperature (25 °C). The working electrode was a rotating ring-disk electrode (RRDE, with a glassy carbon disk and a gold ring). In a typical measurement, 1 mg of the nanoparticles prepared above, 4 mg of carbon powders, and 10 μL of a Nafion solution were ultrasonically mixed in 1 mL of toluene. Then 10 μL of this solution was dropcast onto the glassy-carbon disk (5.61 mm diameter, from Pine Instruments) with a Hamilton microliter syringe. As soon as the electrode was dried, a dilute Nafion solution (0.1 wt%, 3 μL) was added onto it, and the electrode was immersed into electrolyte solutions for voltammetric measurements. The metal loadings on the electrode were all 10 μg.

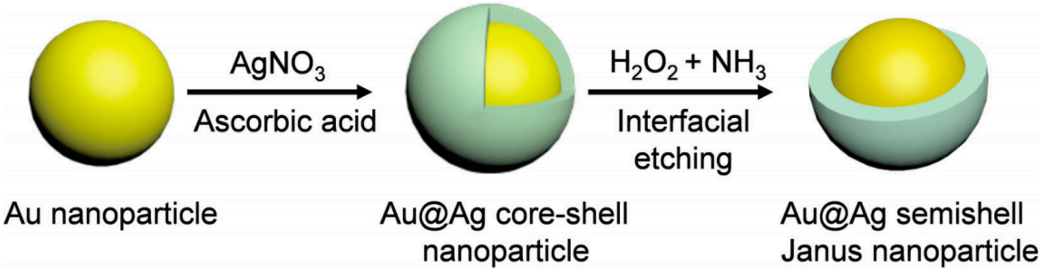

Scheme 7.1

7.3 Results and Discussion

As mentioned above, Au@Ag semishell Janus nanoparticles were prepared by taking advantage of the selective etching of silver by $H_2O_2 + NH_3$ using Au@Ag core–shell nanoparticles as the starting materials.[23,28] The structures of the nanoparticles were first examined by TEM measurements. From panels (A)–(C) in Figure 7.1, one can see that the Au@Ag core–shell nanoparticles were dispersed very well without apparent agglomeration, suggesting sufficient stabilization of the nanoparticles by the 1-dodecanethiol ligands. The formation of a core–shell structure in the metal cores can be clearly seen in the out-of-focus image in panel (A), as well as in the high-resolution image in panel (C) where the dark-contrast gold cores are encapsulated by a low-contrast Ag shell. From panel (C), one can also see that the nanoparticles exhibited well-defined lattice fringes with an interplanar spacing of 0.232 nm that was consistent with the (111) crystalline planes of both fcc Ag (PDF card #4-783) and gold (PDF card #4-784). After chemical etching at the air/water interface by $H_2O_2 + NH_3$, marked differences can be seen. From panel (D), it can be seen that whereas the majority of the nanoparticles remained well separated, a fraction of the nanoparticles aggregated into worm-like structures. This is likely due to destabilization of the nanoparticles caused by interfacial etching. In addition, the resulting nanoparticles became structurally asymmetrical with part of the Ag shells removed and part of the gold cores exposed, as manifested in panel (E), forming Au core@Ag semishell Janus nanoparticles (Scheme 7.1). Furthermore, statistical analysis based on more than 100 nanoparticles shows that the average size of the original Au@Ag core–shell nanoparticles is 7.3 ± 1.1 nm in diameter, with a Au core of *ca*. 5.0 nm diameter and a Ag shell of 1.1 nm in thickness (panel (C)). However, after interfacial etching by H_2O_2 + NH_3, the average diameter of the resulting semishell nanoparticles diminished to 6.4 ± 1.0 nm in diameter, as depicted in the core-size histograms in panel (F). Notably, the decrease of the nanoparticle core diameter (0.9 nm) is very close to the thickness of the Ag shell (1.1. nm). Furthermore, visual inspection showed that the majority (*ca*. 76%) of the as-produced Au@Ag core–shell nanoparticles exhibited a symmetrical contrast of the electron density (between Au and Ag), with an asymmetrical minority (24%). Yet after interfacial etching, the fraction of symmetrical nanoparticles diminished to 46% whereas the asymmetrical fraction increased markedly to 54%. These observations are in good agreement with the formation of Au core@Ag semishell Janus nanoparticles (Scheme 7.1).

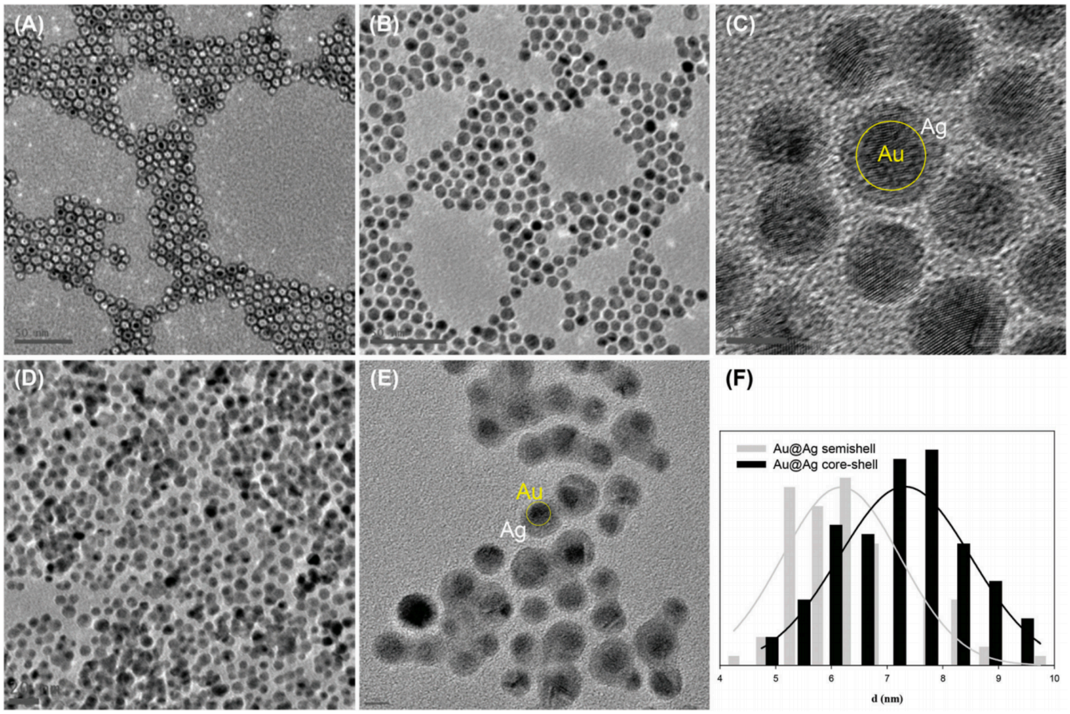

Figure 7.1 Representative TEM micrographs of (A)–(C) Au@Ag core–shell nanoparticles, and (D)–(E) Au@Ag semishell nanoparticles. Scale bars are 50 nm in (A) and (B), 5 nm in (C), 20 nm in (D) and 5 nm in (E). Panel (F) is the particle size histograms of the Au@Ag core–shell and semishell nanoparticles.

With such a structural evolution, the corresponding nanoparticles exhibit a clear variation of the optical properties. From Figure 7.2, one can see that the gold colloids (black curve) exhibit a prominent absorption peak at *ca*. 515 nm, due to the well-known surface plasmon resonance, in contrast to that of Ag nanoparticles (red curve) which appeared at around 394 nm.[29] For the Au@Ag core–shell nanoparticles (green curve), the absorption peak became broadened and centered at 440 nm, intermediate between those for Au and Ag nanoparticles;[25,30-33] After interfacial etching forming Au@Ag semishell Janus nanoparticles (blue curve), the center of the absorption peak red-shifted somewhat to 456 nm, most probably because of the exposure of part of the gold cores. In contrast, when the chemical etching was carried out with the Au@Ag core–shell nanoparticles mixed with the etchants ($H_2O_2 + NH_3$) in the same solvents (denoted as "bulk etching" in Figure 7.2, magenta curve), the resulting nanoparticles showed an absorption maximum at *ca*. 504 nm, very close to that of the Au nanoparticles, indicating almost complete removal of the silver shell from the original Au@Ag nanoparticles.

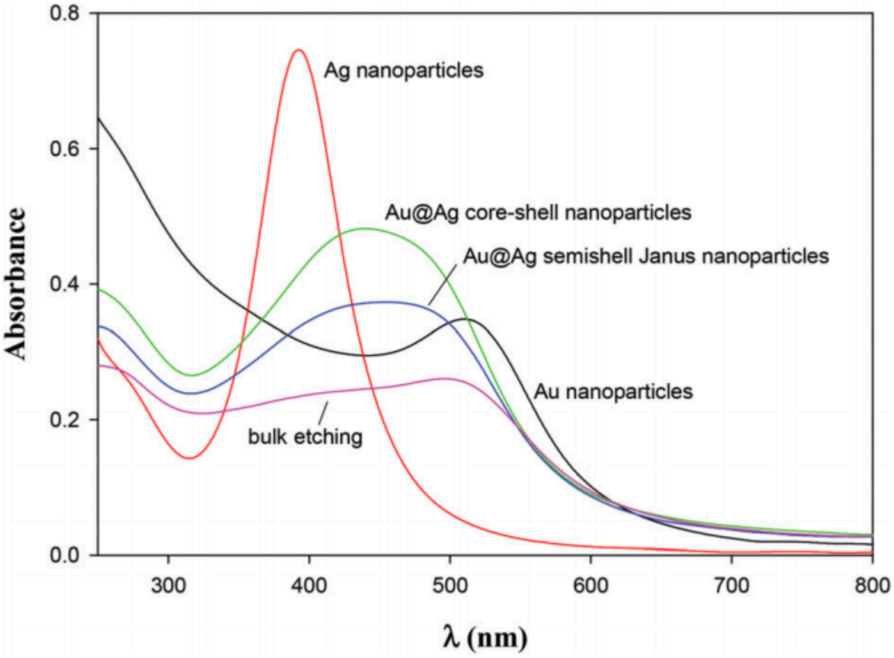

Figure 7.2 UV-vis spectra of Au (black curve), Ag (red curve), Au@Ag core–shell nanoparticles (green curve), and Au@Ag Janus nanoparticles (blue curve). The spectrum of Au@Ag core–shell nanoparticles undergoing bulk etching is also included (magenta curve).

Consistent results were obtained in XPS measurements where the elemental compositions of the nanoparticles were quantified. Figure 7.3 depicts the high-resolution scans of the (top panel) Ag 3d and (bottom panel) Au 4f electrons of the Au@Ag core–shell and semishell Janus nanoparticles. It can be seen that the original Au@Ag core–shell nanoparticles exhibited a doublet at 368.0 and 374.0 eV, corresponding to the $3d_{5/2}$ and $3d_{3/2}$ electrons of metallic silver,[34,35] whereas the doublet for the Au 4f electrons appears at 83.4 eV and 87.1 eV, consistent with those of metallic gold.[36] For the semishell Janus nanoparticles, the binding energies are somewhat higher, at 368.4 and 374.5 eV for Ag 3d and 83.9 and 87.4 eV for Au 4f. It has been known that the binding energy of the Ag 3d electrons decreases as the oxidation state increases. For instance, Hoflund and Hazos observed a decrement of about 0.3 eV from metallic Ag to Ag_2O and then to AgO.[37] Ibele *et al.* also observed a red-shift of *ca*. 0.4 eV of the Ag 3d binding energy when Au–Ag–Au trisegment nanorods were treated with H_2O_2, due to the formation of Ag_2O.[38] In the present study, the fact that semishell Janus nanoparticles exhibited higher binding energies (by *ca*. 0.4 eV) of the Ag 3d electrons than the original Au@Ag core–shell nanoparticles suggested enhanced charge compensation from Au to Ag,[39] as partial removal of the Ag shell (*i.e.*, higher Au : Ag atomic ratio) meant that silver oxide on the nanoparticle surface would be more likely to be reduced by electrons contributed from Au, and the reduced oxidation state led to a higher binding energy of the Ag 3d electrons. Such a charge compensation mechanism may also account for the increase of the binding energy of the Au 4f electrons, with additional contributions likely arising from direct adsorption of thiol ligands on the Au surface upon removal of part of the Ag shell.[40]

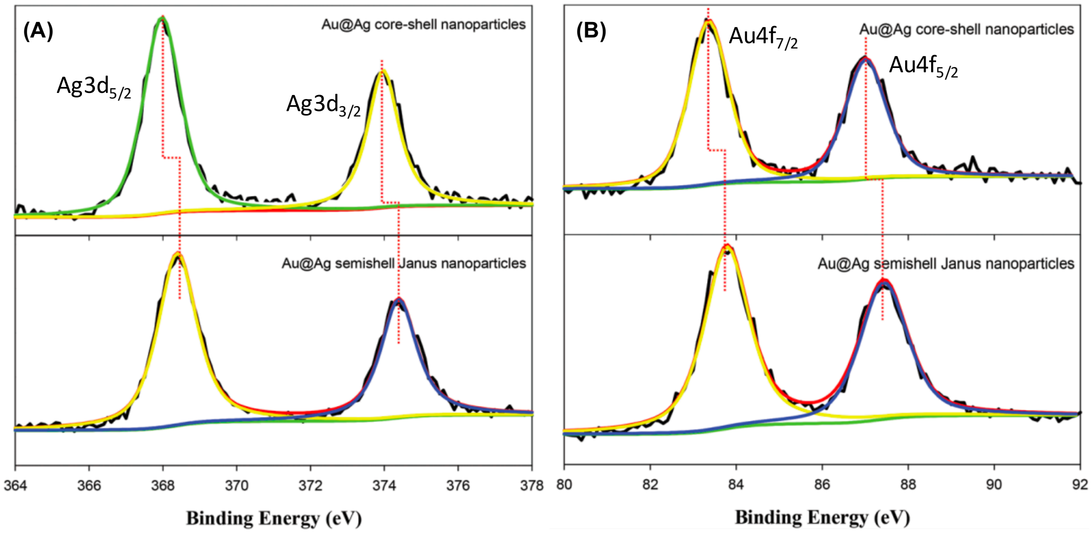

Figure 7.3 XPS spectra of (A) Ag 3d and (B) Au 4f electrons of Au@Ag core–shell and semishell Janus nanoparticles. Black curves are experimental data and colored curves are deconvolution fits.

Furthermore, based on the integrated peak areas of the Ag 3d and Au 4f electrons, the Ag : Au atomic ratio was estimated to be 2.36 : 1 for the Au@Ag core–shell nanoparticles, which is consistent with the nanoparticle structures that consisted of a gold core of *ca*. 5.0 nm in diameter and a Ag shell of 1.1 nm in thickness, as suggested in TEM measurements (Figure 7.1); and the Ag : Au atomic ratio decreased to only 1.25 : 1 for the Au@Ag semishell Janus nanoparticles. Consistent results were obtained in ICP-MS measurements, where the Ag : Au atomic ratio was estimated to be 2.53 : 1 for the Au@Ag core–shell nanoparticles, but only 1.41 : 1 for the semishell Janus nanoparticles. In both measurements, the fact that the nanoparticles lost about 50% of the Ag content suggests that indeed almost half of the Ag shell was removed by interfacial etching.

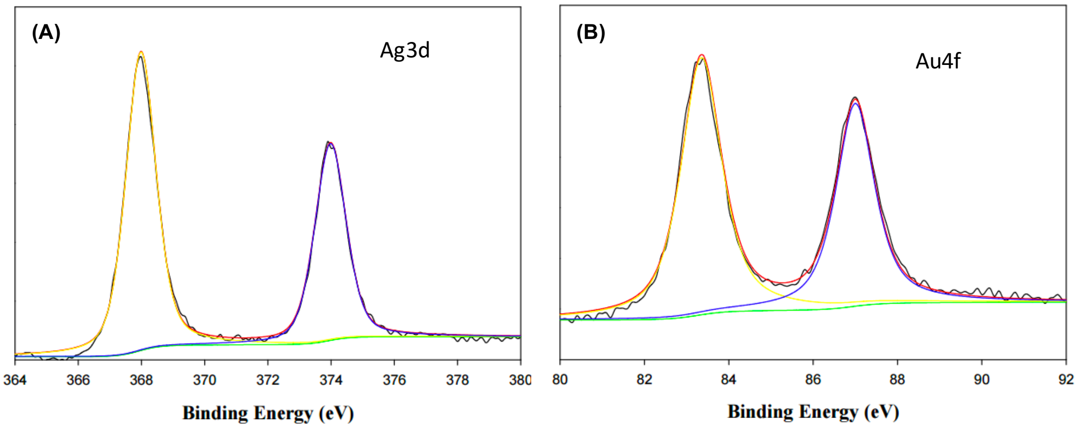

Figure 7.4 XPS spectra of (top) Ag3d and (bottom) Au4f electrons of Ag@Au core-shell nanoparticles. The Ag3d doublet is at 368.0 and 374.1 eV, whereas the Au4f at 83.4 and 87.0 eV. These are consistent with metallic Ag and Au, respectively. Based on the integrated peak areas, the Ag:Au atomic ratio was estimated to be 1.61:1.

Note that consistent results were also obtained of the binding energies of the Ag 3d and Au 4f electrons for the Ag@Au core–shell nanoparticles (Figure 7.4), where the Ag : Au atomic ratio was found to be very close at 1.61 : 1. This indicates that the Ag@Au core–shell nanoparticles and Au@Ag semishell Janus nanoparticles may be approximated as structural isomers. Yet, their electrocatalytic activity towards ORR was markedly different, as shown below.

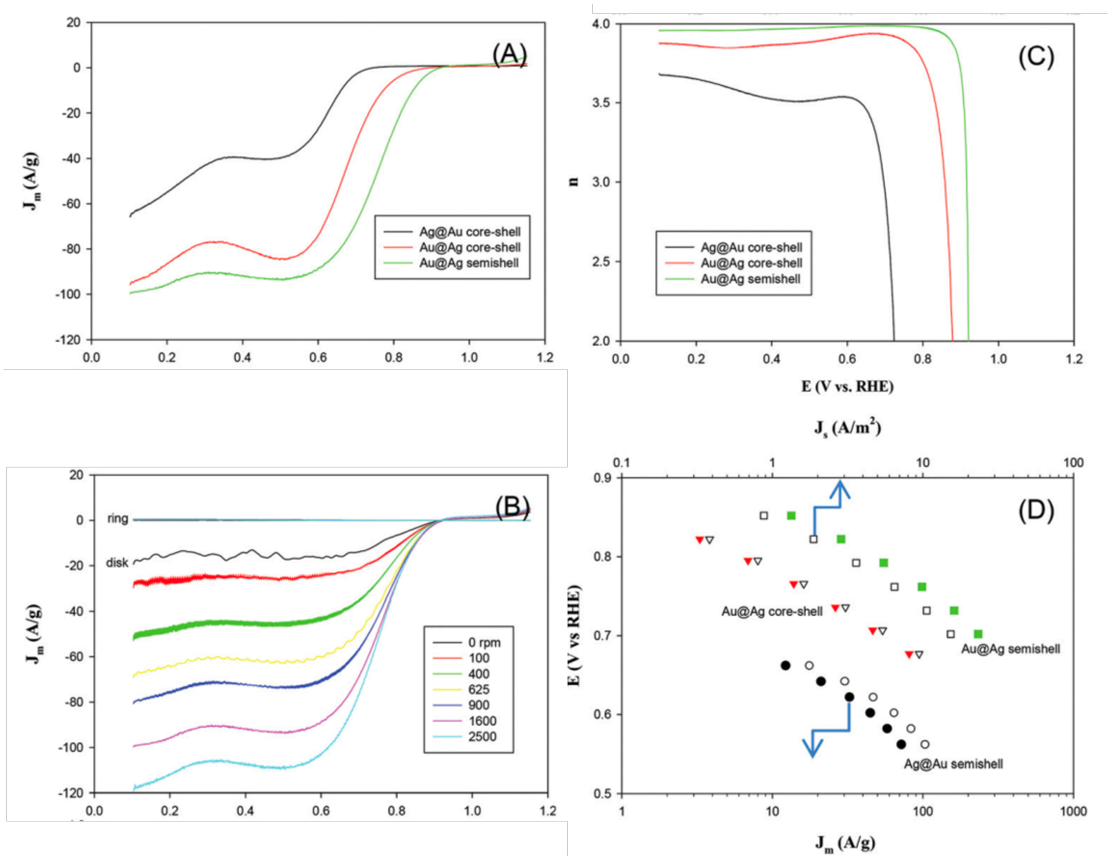

Figure 7.5 (A) ORR polarization curves at 1600 rpm for Ag@Au (black curve), Au@Ag (red curve) core–shell nanoparticles and Au@Ag Janus nanoparticles (green curve). (B) RRDE voltammograms of a glassy carbon electron modified with the Au@Ag Janus nanoparticles in oxygen-saturated 0.1 M NaOH at varied rotation rates (specified in figure legends). (C) Variation of the number of electron transfers (*n*) with electrode potentials for Ag@Au (black curve), Au@Ag (red curve) core–shell nanoparticles and Au@Ag Janus nanoparticles (green curve). Data were obtained by using the respective RRDE voltammograms at 1600 rpm. (D) Tafel plots derived from panel (B) where solid symbols are the mass activity (J_m) and empty symbols are specific activity (J_s). The loading of metal nanoparticle catalysts was all 10 µg. The disk potential ramp was 10 mV s^{-1} and the ring potential was set at +1.5 V.

Experimentally, the nanoparticles prepared above were first loaded onto the glassy carbon disk of a rotating ring-disk electrode and subject to repeated potential cycling within the range of +0.1 V to +1.1 V in a nitrogen saturated 0.1 M NaOH solution until a steady voltammogram appeared. The electrocatalytic activity tests were then carried out in the same solution but saturated with oxygen. Figure 7.5(A) depicts the RDE voltammograms of a glassy carbon electrode modified with Au@Ag core–shell and semishell Janus nanoparticles, as well as Ag@Au core–shell nanoparticles at the same loading of 10 μg. It can be seen that for the Au@Ag Janus nanoparticles, nonzero cathodic currents started to emerge at about +0.95 V (*vs*. RHE) and the currents reached a plateau at around +0.60 V. This performance is markedly better than that of the Au@Ag core–shell nanoparticles where the onset potential was 40 mV less positive at +0.91 V; whereas the Ag@Au core–shell nanoparticles displayed the least positive onset potential at +0.77 V. The diffusion-limited current also decreases in the same order. For instance, at +0.40 V, the current density was 92 A g^{-1} for Au@Ag semishell Janus nanoparticles, 80 A g^{-1} for Au@Ag core–shell nanoparticles, and only 40 A g^{-1} for Ag@Au core–shell nanoparticles. Altogether, these results indicate that a silver shell is more active in catalyzing ORR than a gold one, and the activity was even higher with a silver half-shell where both Ag and Au surfaces were accessible (note that Ag@Au semishell nanoparticles could not be produced as Au was chemically inert against H_2O_2 and NH_3, Figure 7.6).

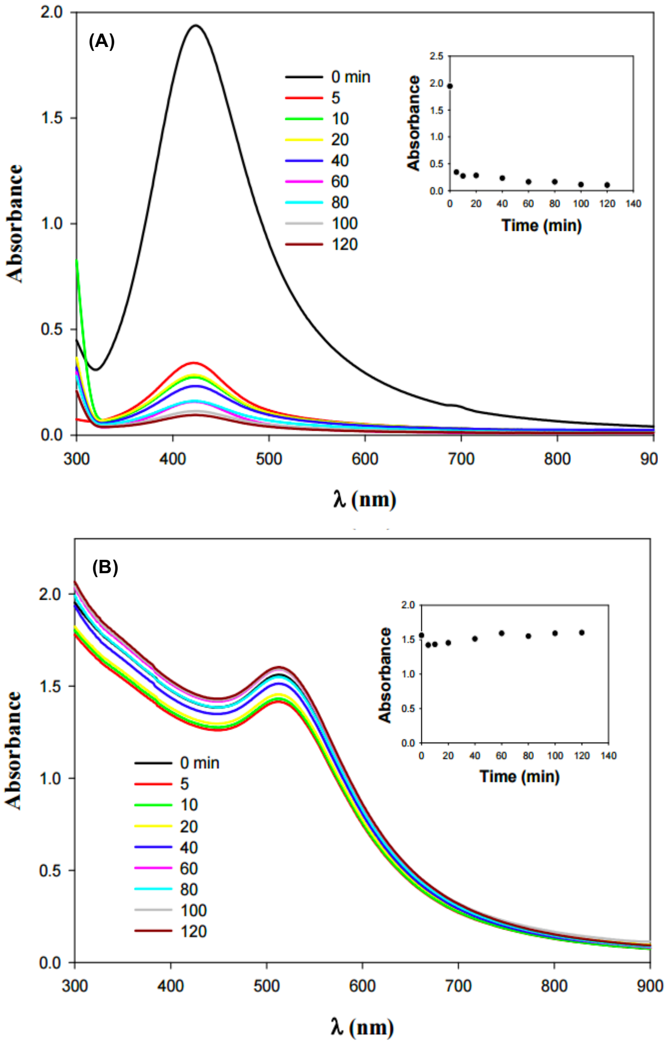

Figure 7.6 UV-vis spectra of (top) Ag and (bottom) Au nanoparticles at different time intervals after the addition of 20 mM H_2O_2 + NH_3. Insets show the variation of the respective surface plasmon resonance (SPR) intensity with reaction time. One can see that the SPR intensity of the Ag nanoparticles diminished rather quickly, due to effective etching of the Ag nanoparticles by H_2O_2 + NH_3, whereas the SPR intensity of the gold nanoparticles remained largely unchanged, because Au nanoparticles were chemically inert against the H_2O_2 + NH_3 etchants.

Panel (B) depicts the RRDE voltammograms of the Au@Ag semishell Janus nanoparticles at different electrode rotation rates (from 100 to 2500 rpm). One can see that the voltammetric currents increased with the increasing electrode rotation rate and the disk currents were at least two orders of magnitude higher than those at the ring electrode, suggesting that only a minimal amount of peroxide intermediates was produced during ORR. In fact, the number of electron transfers involved in the reduction of one O_2 molecule on the nanoparticles was determined by $n = 4I_D/(I_D + I_R/N)$, where I_D and I_R are disk and ring currents, respectively. By using the disk and ring currents collected at 1600 rpm as an example, one can see that within the wide potential range of +0.90 V to +0.10 V, the n values increased markedly in the order of Ag@Au core shell < Au@Ag core–shell < Au@Ag semishell nanoparticles, as evidenced in panel (C). For instance, at +0.60 V, the Au@Ag semishell Janus nanoparticles exhibited the highest n value of 3.98, somewhat higher than that (3.92) of Au@Ag core–shell nanoparticles, while Ag@Au core–shell nanoparticles showed the lowest n value of 3.53, corresponding to a peroxide yield of 1%, 4% and 23.5%, respectively. This means that oxygen mostly underwent four-electron reduction at Au@Ag semishell Janus and core–shell nanoparticles, $O_2 + 2H_2O + 4e \rightarrow 4OH^-$, whereas a rather significant number of peroxide species was generated during ORR on Ag@Au core–shell nanoparticles. Note that the results were highly reproducible and repeated measurements showed no more than 10% deviation.

The clear discrepancy of the ORR activity among these three nanoparticle catalysts may be understood within the context of surface accessibility for oxygen adsorption and reduction. Note that for bimetallic core–shell nanoparticles, the electrocatalytic activity is mainly determined by the shell materials. Prior studies have shown that a Ag surface displays better ORR catalytic activity than a gold one because of its stronger oxygen binding energy.[41-43] The ORR activity was further enhanced when both Ag and Au surfaces were exposed and accessible, likely due to synergistic interactions between the two metals (*vide infra*).

Similar behaviors can be observed with the mass-specific kinetic current density (J_m), as depicted in the Tafel plot of panel (D). It can be seen that the J_m increased with an increasingly negative electrode potential. In addition, the activity of the Janus nanoparticles is significantly higher than that of the core–shell nanoparticles. For instance, at +0.66 V, J_m for Au@Ag semishell Janus nanoparticles was estimated to be 633 A g^{-1}, about 4.8 times that (131 A g^{-1}) of Au@Ag core–shell nanoparticles and 45 times that (14 A g^{-1}) of Ag@Au core–shell nanoparticles. Consistent results can also be seen in the comparison of the corresponding specific activity (J_s, which was estimated by normalizing the kinetic currents against the electrochemical surface area quantified by Pb UPD, Figure 7.7).[44,45] For instance, at +0.66 V, J_s for Au@Ag semishell Janus nanoparticles was *ca.* 23.0 A m^{-2}, about 2.2 times that (10.5 A m^{-2}) of Au@Ag core–shell nanoparticles and 13 times that (1.78 A m^{-2}) of Ag@Au core–shell nanoparticles.

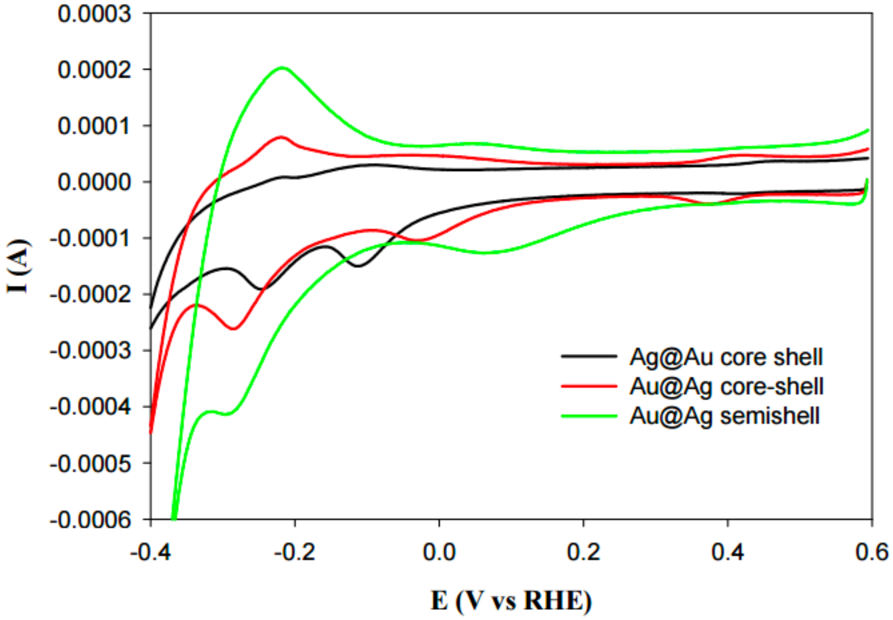

Figure 7.7 Cyclic voltammograms of a glassy carbon electrode modified with Ag@Au core-shell, Au@Ag core-shell and Au@Ag semishell nanoparticles in 0.05 mM $Pb(OAc)_2$ + 0.1 M $HClO_4$ at the sweep rate of 100 mV/s. Catalyst loadings were both 10 μg. The effective electrochemical surface areas as summarized below were determined by oxygen adsorption on Ag (210 $\mu C/cm^2$) and Au (390 $\mu C/cm^2$), in which the Ag oxidation peaks and gold oxide reduction peaks were used to obtain the amount of charge.

Note that for oxygen electroreduction at nanoparticle catalyst surfaces, the Tafel slopes are typically found at 60 or 120 mV dec^{-1}, where the former corresponds to a pseudo two-electron reaction as the rate determining step and in the latter, the rate determining step is the first-electron reduction of oxygen.[46] In the present study, linear regressions show that the slopes are 128 mV dec^{-1}, 104 mV dec^{-1} and 119 mV dec^{-1} for Ag@Au core–shell, Au@Ag core–shell nanoparticles and Au@Ag semishell Janus nanoparticles, respectively, suggesting that ORR on these three nanoparticle catalysts was all likely limited by the first electron reduction. Such behaviors have been observed on the Pt or Pt alloy surface, suggesting that the catalytic mechanism of ORR on AgAu resembles that on Pt, which involves O–O bond breaking and adsorption of oxygenate intermediates, but is distinctly different from that on pure Ag or Au catalysts, where the ORR rate is limited by the absorption of O_2 molecules on the metal surface and the first electron transfer.[47-49]

Notably, within the context of onset potential, *n* value, and mass/specific activity, the electrocatalytic performance of the Au@Ag semishell Janus nanoparticles prepared above is markedly better than those observed with monometallic Au or Ag nanoparticles of similar sizes,[43,50,51] and even comparable to that of commercial Pt/C catalysts (except with a lower mass activity).[52] In addition, in comparison with the AuAg alloy nanoparticles reported in recent literature, the ORR activity of the semishell Janus nanoparticles is also enhanced. For instance, the onset potential for ORR observed above for the Au@Ag semishell Janus nanoparticles was at least 30 mV more positive than those for the Au@Ag bimetallic Janus nanoparticles prepared by interfacial galvanic exchange reactions[18] as well as for AgAu (bulk) alloy nanoparticles.[53,54]

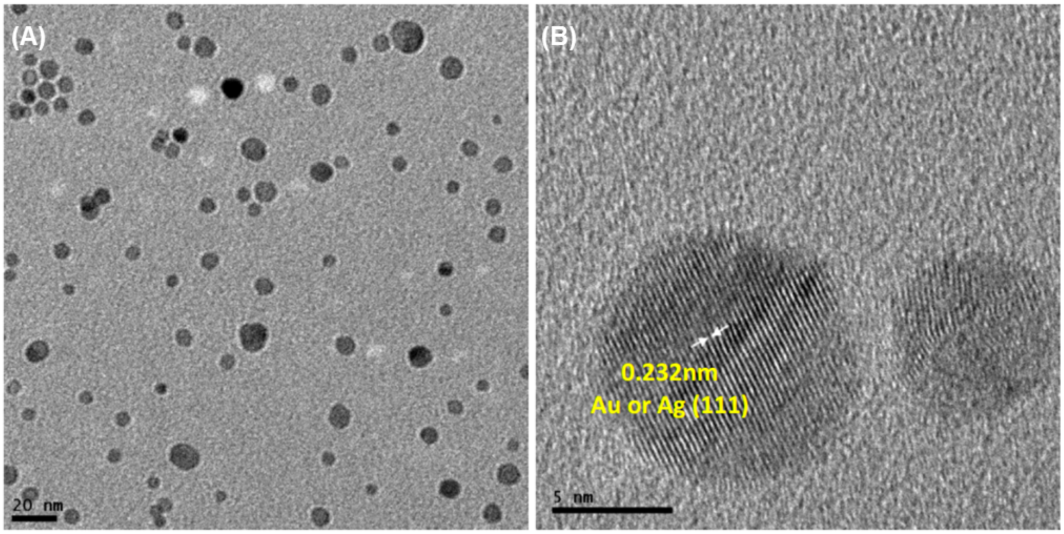

Figure 7.8 Representative TEM micrographs of Ag@Au core-shell nanoparticles. Scale bars are (A) 20 nm and (B) 5 nm.

It is most likely that the improved performance of the Au@Ag Janus nanoparticles over Au@Ag or Ag@Au core–shell nanoparticles is due to the partial exposure of the core metal surface to oxygen absorption. As mentioned earlier, for core–shell nanoparticles, the catalytic activity is mainly dictated by the shell materials, as the inner cores are inaccessible[21] but may impact the catalytic activity through surface strain, particle size and shape.[20] In the present study, these contributions are likely to be minimal as Ag and Au exhibit almost no lattice mismatch and the three nanoparticles were largely of the same size and shape (Figure 7.1 and Figure 7.8).[55]Instead, the remarkable ORR performance observed with the Au@Ag semishell nanoparticles may be ascribed to the enhanced charge transfer from Au to Ag,[39] as manifested in XPS measurements (Figure 7.3), which inhibited the formation of (inactive) silver oxide under ORR conditions in alkaline media. This resulted in a more reactive Ag surface for ORR than pure Ag,[56,57] as reflected by a positive shift of the equilibrium potential for the first electron transfer reaction and a reduced overpotential and positive shift of the onset potential.[53]

7.4 Conclusion

In the present study, gold core@Ag semishell Janus nanoparticles were prepared, for the first time ever, by interfacial etching of Au@Ag core–shell nanoparticles on the water surface based on the Langmuir method. The asymmetrical nanoparticle structures were confirmed by TEM, XPS and UV-vis absorption measurements. The resulting bimetallic Janus nanoparticles exhibited markedly enhanced electrocatalytic activity in oxygen reduction, as compared to their Au@Ag and Ag@Au core–shell counterparts, within the context of onset potential, number of electron transfers, and kinetic current density. This was likely due to partial charge transfer from Au to Ag that optimized oxygen adsorption on the metal surfaces. These results further demonstrate the significance of the interfacial engineering in nanoparticle modification and the impact on their electrocatalytic activity.

7.5 References

(1) Qin, X.; Xu, A.; Liu, L.; Deng, W.; Chen, C.; Tan, Y.; Fu, Y.; Xie, Q.; Yao, S. Ultrasensitive electrochemical immunoassay of proteins based on in situ duple amplification of gold nanoparticle biolabel signals. *Chem commun* **2015**, *51*, 8540-8543.

(2) Bodhisatwa, D.; Fernandez, F.; John, A.; Sharma, C. P. Synthesis, Characterization and Bio-Labeling Studies of Trypsin Stabilized Silver Quantum Clusters. *J Biomater Tiss Eng* **2012**, *2*, 299-306.

(3) Howes, P. D.; Chandrawati, R.; Stevens, M. M. Colloidal nanoparticles as advanced biological sensors. *Science* **2014**, *346*, 53-+.

(4) Guo, L. H.; Xu, Y.; Ferhan, A. R.; Chen, G. N.; Kim, D. H. Oriented Gold Nanoparticle Aggregation for Colorimetric Sensors with Surprisingly High Analytical Figures of Merit. *J Am Chem Soc* **2013**, *135*, 12338-12345.

(5) Guo, S. J.; Zhang, X.; Zhu, W. L.; He, K.; Su, D.; Mendoza-Garcia, A.; Ho, S. F.; Lu, G.; Sun, S. H. Nanocatalyst Superior to Pt for Oxygen Reduction

Reactions: The Case of Core/Shell Ag(Au)/CuPd Nanoparticles. *J Am Chem Soc* **2014**, *136*, 15026-15033.

(6) Walther, A.; Muller, A. H. Janus particles: synthesis, self-assembly, physical properties, and applications. *Chem rev* **2013**, *113*, 5194-5261.

(7) Perro, A.; Reculusa, S.; Ravaine, S.; Bourgeat-Lami, E. B.; Duguet, E. Design and synthesis of Janus micro- and nanoparticles. *J Mater Chem* **2005**, *15*, 3745-3760.

(8) Lattuada, M.; Hatton, T. A. Synthesis, properties and applications of Janus nanoparticles. *Nano Today* **2011**, *6*, 286-308.

(9) Song, Y.; Chen, S. W. Janus Nanoparticles as Versatile Phase-Transfer Reagents. *Langmuir* **2014**, *30*, 6389-6397.

(10) Lassiter, J. B.; Aizpurua, J.; Hernandez, L. I.; Brandl, D. W.; Romero, I.; Lal, S.; Hafner, J. H.; Nordlander, P.; Halas, N. J. Close encounters between two nanoshells. *Nano Lett* **2008**, *8*, 1212-1218.

(11) Yu, H.; Chen, M.; Rice, P. M.; Wang, S. X.; White, R. L.; Sun, S. H. Dumbbell-like bifunctional Au-Fe3O4 nanoparticles. *Nano Lett* **2005**, *5*, 379-382.

(12) Pradhan, S.; Ghosh, D.; Chen, S. W. Janus Nanostructures Based on Au-TiO2 Heterodimers and Their Photocatalytic Activity in the Oxidation of Methanol. *Acs Appl Mater Inter* **2009**, *1*, 2060-2065.

(13) Chen, T.; Chen, G.; Xing, S. X.; Wu, T.; Chen, H. Y. Scalable Routes to Janus Au-SiO2 and Ternary Ag-Au-SiO2 Nanoparticles. *Chem Mater* **2010**, *22*, 3826-3828.

(14) Zeng, J.; Zhu, C.; Tao, J.; Jin, M. S.; Zhang, H.; Li, Z. Y.; Zhu, Y. M.; Xia, Y. N. Controlling the Nucleation and Growth of Silver on Palladium Nanocubes by Manipulating the Reaction Kinetics. *Angew Chem Int Ed* **2012**, *51*, 2354-2358.

(15) Guo, X.; Zhang, Q.; Sun, Y. H.; Zhao, Q.; Yang, J. Lateral Etching of Core-Shell Au@Metal Nanorods to Metal-Tipped Au Nanorods with Improved Catalytic Activity. *ACS nano* **2012**, *6*, 1165-1175.

(16) Logsdail, A. J.; Johnston, R. L. Predicting the Optical Properties of Core-Shell and Janus Segregated Au-M Nanoparticles (M = Ag, Pd). *J Phys Chem C* **2012**, *116*, 23616-23628.

(17) Lu, X. M.; Tuan, H. Y.; Chen, J. Y.; Li, Z. Y.; Korgel, B. A.; Xia, Y. N. Mechanistic studies on the galvanic replacement reaction between multiply twinned particles of Ag and HAuCl4 in an organic medium. *J Am Chem Soc* **2007**, *129*, 1733-1742.

(18) Song, Y.; Liu, K.; Chen, S. W. AgAu Bimetallic Janus Nanoparticles and Their Electrocatalytic Activity for Oxygen Reduction in Alkaline Media. *Langmuir* **2012**, *28*, 17143-17152.

(19) Zhu, C.; Zeng, J.; Tao, J.; Johnson, M. C.; Schmidt-Krey, I.; Blubaugh, L.; Zhu, Y. M.; Gu, Z. Z.; Xia, Y. N. Kinetically Controlled Overgrowth of Ag or Au on Pd Nanocrystal Seeds: From Hybrid Dimers to Nonconcentric and Concentric Bimetallic Nanocrystals. *J Am Chem Soc* **2012**, *134*, 15822-15831.

(20) Zhang, X.; Lu, G. Computational Design of Core/Shell Nanoparticles for Oxygen Reduction Reactions. *J Phys Chem Lett* **2014**, *5*, 292-297.

(21) Liu, X. W.; Wang, D. S.; Li, Y. D. Synthesis and catalytic properties of bimetallic nanomaterials with various architectures. *Nano Today* **2012**, *7*, 448-466.

(22) Wang, G. X.; Wu, H. M.; Wexler, D.; Liu, H. K.; Savadogo, O. Ni@Pt core-shell nanoparticles with enhanced catalytic activity for oxygen reduction reaction. *J Alloy Compd* **2010**, *503*, L1-L4.

(23) Song, Y.; Chen, S. W. Trimetallic Ag@AuPt Neapolitan nanoparticles. *Nanoscale* **2013**, *5*, 7284-7289.

(24) Ieong, N. S.; Brebis, K.; Daniel, L. E.; O'Reilly, R. K.; Gibson, M. I. The critical importance of size on thermoresponsive nanoparticle transition temperatures: gold and micelle-based polymer nanoparticles. *Chem Commun* **2011**, *47*, 11627-11629.

(25) Samal, A. K.; Polavarapu, L.; Rodal-Cedeira, S.; Liz-Marzan, L. M.; Perez-Juste, J.; Pastoriza-Santos, I. Size tunable Au@Ag core-shell nanoparticles: synthesis and surface-enhanced Raman scattering properties. *Langmuir* **2013**, *29*, 15076-15082.

(26) Lista, M.; Liu, D. Z.; Mulvaney, P. Phase Transfer of Noble Metal Nanoparticles to Organic Solvents. *Langmuir* **2014**, *30*, 1932-1938.

(27) Yang, Y.; Liu, J. Y.; Fu, Z. W.; Qin, D. Galvanic Replacement-Free Deposition of Au on Ag for Core-Shell Nanocubes with Enhanced Chemical Stability and SERS Activity. *J Am Chem Soc* **2014**, *136*, 8153-8156.

(28) Shahjamali, M. M.; Bosman, M.; Cao, S. W.; Huang, X.; Cao, X. H.; Zhang, H.; Pramana, S. S.; Xue, C. Surfactant-Free Sub-2 nm Ultrathin Triangular Gold Nanoframes. *Small* **2013**, *9*, 2880-2886.

(29) Creighton, J. A.; Eadon, D. G. Ultraviolet Visible Absorption-Spectra of the Colloidal Metallic Elements. *J Chem Soc Faraday T* **1991**, *87*, 3881-3891.

(30) Rodriguez-Gonzalez, B.; Burrows, A.; Watanabe, M.; Kiely, C. J.; Liz-Marzan, L. M. Multishell bimetallic AuAg nanoparticles: synthesis, structure and optical properties. *J Mater Chem* **2005**, *15*, 1755-1759.

(31) Cha, S. K.; Mun, J. H.; Chang, T.; Kim, S. Y.; Kim, J. Y.; Jin, H. M.; Lee, J. Y.; Shin, J.; Kim, K. H.; Kim, S. O. Au-Ag core-shell nanoparticle array by block copolymer lithography for synergistic broadband plasmonic properties. *ACS nano* **2015**, *9*, 5536-5543.

(32) Ma, Y.; Li, W.; Cho, E. C.; Li, Z.; Yu, T.; Zeng, J.; Xie, Z.; Xia, Y. Au@Ag core-shell nanocubes with finely tuned and well-controlled sizes, shell thicknesses, and optical properties. *ACS nano* **2010**, *4*, 6725-6734.

(33) Underwood, S.; Mulvaney, P. Effect of the Solution Refractive-Index on the Color of Gold Colloids. *Langmuir* **1994**, *10*, 3427-3430.

(34) Wang, A. Q.; Chang, C. M.; Mou, C. Y. Evolution of catalytic activity of Au-Ag bimetallic nanoparticles on mesoporous support for CO oxidation. *J Phys Chem B* **2005**, *109*, 18860-18867.

(35) Han, S. W.; Kim, Y.; Kim, K. Dodecanethiol-derivatized Au/Ag bimetallic nanoparticles: TEM, UV/VIS, XPS, and FTIR analysis. *J Colloid Interf Sci* **1998**, *208*, 272-278.

(36) Yi, C. W.; Luo, K.; Wei, T.; Goodman, D. W. The composition and structure of Pd-Au surfaces. *J Phys Chem B* **2005**, *109*, 18535-18540.

(37) Hoflund, G. B.; Hazos, Z. F.; Salaita, G. N. Surface characterization study of Ag, AgO, and Ag2O using x-ray photoelectron spectroscopy and electron energy-loss spectroscopy. *Phys Rev B* **2000**, *62*, 11126-11133.

(38) Ibele, M. E.; Liu, R.; Beiswenger, K.; Sen, A. Synthesis and characterization of flexible, composite, nanorod nunchucks. *J Mater Chem* **2011**, *21*, 14410-14413.

(39) Mott, D. M.; Dao, T. N. A.; Singh, P.; Shankar, C.; Maenosono, S. Electronic transfer as a route to increase the chemical stability in gold and silver core-shell nanoparticles. *Adv Colloid Interfac* **2012**, *185*, 14-33.

(40) Hostetler, M. J.; Wingate, J. E.; Zhong, C. J.; Harris, J. E.; Vachet, R. W.; Clark, M. R.; Londono, J. D.; Green, S. J.; Stokes, J. J.; Wignall, G. D.; Glish, G. L.; Porter, M. D.; Evans, N. D.; Murray, R. W. Alkanethiolate gold cluster molecules with core diameters from 1.5 to 5.2 nm: Core and monolayer properties as a function of core size. *Langmuir* **1998**, *14*, 17-30.

(41) Norskov, J. K.; Rossmeisl, J.; Logadottir, A.; Lindqvist, L.; Kitchin, J. R.; Bligaard, T.; Jonsson, H. Origin of the overpotential for oxygen reduction at a fuel-cell cathode. *J Phys Chem B* **2004**, *108*, 17886-17892.

(42) Siahrostami, S.; Verdaguer-Casadevall, A.; Karamad, M.; Deiana, D.; Malacrida, P.; Wickman, B.; Escudero-Escribano, M.; Paoli, E. A.; Frydendal, R.; Hansen, T. W.; Chorkendorff, I.; Stephens, I. E. L.; Rossmeisl, J. Enabling direct H2O2 production through rational electrocatalyst design. *Nat Mater* **2013**, *12*, 1137-1143.

(43) Singh, P.; Buttry, D. A. Comparison of Oxygen Reduction Reaction at Silver Nanoparticles and Polycrystalline Silver Electrodes in Alkaline Solution. *J Phys Chem C* **2012**, *116*, 10656-10663.

(44) Trasatti, S.; Petrii, O. A. Real Surface-Area Measurements in Electrochemistry. *J Electroanal Chem* **1992**, *327*, 353-376.

(45) Motheo, A. J.; Machado, S. A. S.; Vankampen, M. H.; Santos, J. R. Electrochemical Determination of Roughness of Silver Electrode Surface. *J Brazil Chem Soc* **1993**, *4*, 122-127.

(46) Pasti, I. A.; Gavrilov, N. M.; Mentus, S. V. Potentiodynamic Investigation of Oxygen Reduction Reaction on Polycrystalline Platinum Surface in Acidic Solutions: the Effect of the Polarization Rate on the Kinetic Parameters. *Int J Electrochem Sc* **2012**, *7*, 11076-11090.

(47) Markovic, N. M.; Gasteiger, H. A.; Philip, N. Oxygen reduction on platinum low-index single-crystal surfaces in alkaline solution: Rotating ring disk(Pt(hkl)) studies. *J Phys Chem-Us* **1996**, *100*, 6715-6721.

(48) Stamenkovic, V. R.; Mun, B. S.; Arenz, M.; Mayrhofer, K. J.; Lucas, C. A.; Wang, G.; Ross, P. N.; Markovic, N. M. Trends in electrocatalysis on extended and nanoscale Pt-bimetallic alloy surfaces. *Nature materials* **2007**, *6*, 241-247.

(49) Mei, D.; He, Z. D.; Zheng, Y. L.; Jiang, D. C.; Chen, Y. X. Mechanistic and kinetic implications on the ORR on a Au(100) electrode: pH, temperature and H-D kinetic isotope effects. *Phys Chem Chem Phys* **2014**, *16*, 13762-13773.

(50) Mirkhalaf, F.; Schiffrin, D. J. Electrocatalytic Oxygen Reduction on Functionalized Gold Nanoparticles Incorporated in a Hydrophobic Environment. *Langmuir* **2010**, *26*, 14995-15001.

(51) Tammeveski, L.; Erikson, H.; Sarapuu, A.; Kozlova, J.; Ritslaid, P.; Sammelselg, V.; Tammeveski, K. Electrocatalytic oxygen reduction on silver nanoparticle/multi-walled carbon nanotube modified glassy carbon electrodes in alkaline solution. *Electrochem Commun* **2012**, *20*, 15-18.

(52) Genies, L.; Faure, R.; Durand, R. Electrochemical reduction of oxygen on platinum nanoparticles in alkaline media. *Electrochim Acta* **1998**, *44*, 1317-1327.

(53) Hu, P.; Song, Y.; Chen, L.; Chen, S. Electrocatalytic activity of alkyne-functionalized AgAu alloy nanoparticles for oxygen reduction in alkaline media. *Nanoscale* **2015**.

(54) Yang, C. X.; Huang, B.; Xiao, L.; Ren, Z. D.; Liu, Z. L.; Lu, J. T.; Zhuang, L. Activating Ag by even more inert Au: a peculiar effect on electrocatalysis toward oxygen reduction in alkaline media. *Chem Commun* **2013**, *49*, 11023-11025.

(55) Sanchez-Ramirez, J. F.; Pal, U.; Nolasco-Hernandez, L.; Mendoza-Alvarez, J.; Pescador-Rojas, J. A. Synthesis and Optical Properties of Au-Ag Alloy Nanoclusters with Controlled Composition. *J Nanomater* **2008**.

(56) Van Cleve, T.; Gibara, E.; Linic, S. Electrochemical Oxygen Reduction Reaction on Ag Nanoparticles of Different Shapes. *Chemcatchem* **2016**, *8*, 256-261.

(57) He, G. Q.; Song, Y.; Phebus, B.; Liu, K.; Deming, C. P.; Hu, P. G.; Chen, S. W. Electrocatalytic Activity of Organically Functionalized Silver Nanoparticles in Oxygen Reduction. *Sci Adv Mater* **2013**, *5*, 1727-1736.

Chapter 8

Silver-Copper Hollow Nanoshells as Phase-Transfer Reagents and Catalysts in the Reduction of 4-Nitroaniline

Reproduced with permission from (Limei Chen, Peiguang Hu, Yi Peng, Jia En Lu, Mauricio D. Rojas-Andrade and Shaowei Chen, "Silver-Copper Hollow Nanoshells as Phase-Transfer Reagents and Catalysts in the Reduction of 4-Nitroaniline", Part. Part. Syst. Char., 2017, 1600358).

8.1 Introduction

In recent decades, transition-metal nanostructures such as nanoparticles, nanocubes, nanoplates, and nanoshells have been attracting significant interest largely because of their unique optical and electronic properties and potential applications in diverse fields ranging from catalysis to drug delivery and chemical/biological sensing.[1-4] Among these, hollow nanoshells represent a unique group of functional nanomaterials, where the materials properties may be deliberately manipulated by the size, shape, shell thickness, and elemental compositions. Furthermore, with proper surface functionalization, the hollow nanoshells may be dispersible in a wide range of solvent media and used for the ready encapsulation and delivery of target molecules.[5] For instance, nanoshells of Pt, Ag, Au, and Au–Ag bimetallic alloys have been prepared, used for drug delivery, and exhibited apparent catalytic activity in a variety of reactions, as compared to their solid counterparts.[6-8] This is largely ascribed to the high surface area and porous structure of the metal shells that are presumed to facilitate the catalytic reactions and mass transport of reaction species.

Several methods have been reported for the synthesis of hollow metal nanostructures, such as galvanic replacement based on the Kirkendall effect, chemical etching, and rigid templating.[7,9-11] With a rigid template, a thin shell structure can be easily formed and tuned; however, final removal of the template is challenging.[12] In the Kirkendall method, a shell is formed via chemical reactions based on a self-template process, by which the template diminishes with the formation of a hollow structure.[13] For instance, Kado et al. reported a simple, one-pot synthesis of silver nanoshells based on nanoscale Kirkendall effect by the sequential addition of NaSCN and $NaBH_4$ into an $AgNO_3$solution.[10] The formation mechanism involved the reduction of hardly soluble AgSCN in the aqueous solution by $NaBH_4$. However, the resulting silver nanoshells lacked stability in solution because of ready oxidation when exposed to ambient. This represents a major challenge for further engineering and practical applications.

In the present study, by adopting the one-pot synthesis method mentioned above,[10] we prepared an Ag–Cu hollow nanoshell, which we believe is the first of its kind. The bimetallic nanoshells exhibited a rather uniform spherical structure, and were remarkably stable in solution for months at room temperature, in contrast to the monometallic Ag counterparts.[10] Interestingly, the nanoscale cavity might be exploited for the encapsulation of selected molecules such as rhodamine 6G (R6G)[14] and phase transfer from water to apolar organic media by deliberate surface functionalization. In addition, the Ag–Cu nanoshells exhibited enhanced catalytic activity in the reduction of 4-nitroaniline by $NaBH_4$, as compared to solid Ag–Cu nanoparticles, likely due to ready accessibility of both the internal and external surfaces in the nanoshells for the catalytic reactions.

8.2 Experimental Section

Chemicals

Silver nitrate ($AgNO_3$, Fisher Scientific), cupric nitrate ($Cu(NO_3)_2 \cdot 2.5H_2O$, Fisher Scientific), sodium thiocyanate (NaSCN, Fisher Science Education), sodium borohydride ($NaBH_4$, ≥98%, ACROS), sodium citrate dihydrate ($Na_3C_6H_5O_7 \cdot 2H_2O$, Fisher Scientific), R6G (99%, ACROS), 4-nitroaniline (98%, Alfar Aesar), L(+)-cysteine hydrochloride monohydrate (Cys, MCB), 1-dodecanethiol (C12SH, 96%, ACROS), and acetic acid (HOAc, Glacial, Fisher Scientific) were all used as received without any further purification. Solvents were purchased at the highest purity available from typical commercial sources and used as received. Water was supplied with a Barnstead Nanopure water system (18.3 MΩ cm).

Synthesis of Silver–Copper (Ag–Cu) Hollow Nanoshells

Silver–copper nanoshells were prepared by adopting a synthetic procedure reported in the literature for the preparation of monometallic Ag nanoshells.[10] In brief, 0.5 mL of an aqueous solution of NaSCN (15×10^{-3} M) was diluted by 20 mL of Nanopure water to make a homogeneous solution, and separately, 0.3 mL of a $AgNO_3$ aqueous solution (10×10^{-3}M) and 0.1 mL of a $Cu(NO_3)_2$ solution (10×10^{-3} M) (corresponding to an Ag:Cu molar feed ratio of 3:1) were added to 20 mL of Nanopure water. The NaSCN solution was then slowly added to the metal salt solution under magnetic stirring for 5 min to generate a blurry solution. Then 5 mL of a freshly prepared, cold $NaBH_4$ solution (1×10^{-3} M) was slowly added to the solution under constant stirring. Once the color of the solution started to turn bright blue (indicating the formation of Ag–Cu nanoshells), 0.1 mL of an aqueous solution of L(+)-cysteine (5×10^{-3} M) was immediately injected into the solution as protecting ligands. Excess ligands were removed by dialysis in Nanopure water for three days, affording purified cys-capped Ag–Cu hollow nanoshells.

As a control, monometallic silver nanoshells were prepared by using the same procedure[10] except that no $Cu(NO_3)_2$ was added into the metal salt solution.

A second control was carried out with silver–copper solid nanoparticles. Experimentally, 0.75 mL of an $AgNO_3$ aqueous solution (10×10^{-3} M), 0.25 mL of a $Cu(NO_3)_2$ solution (10×10^{-3} M), and 0.01 mmol of sodium citrate dehydrate were added into 100 mL of Nanopure water, corresponding to an Ag:Cu molar feed ratio of 3:1; the solution was bubbled with nitrogen for 20 min, into which was then slowly added 12.5 mL of a freshly prepared, cold $NaBH_4$ solution (1×10^{-3} M). The appearance of a faint yellow color signified the formation of silver-rich nanoparticles. The solution was under magnetic stirring for 10 min before 0.25 mL of an aqueous solution of L(+)-cysteine (5×10^{-3} M) was added to the solution to stabilize the nanoparticles. The resulting nanoparticles were then purified by dialysis in Nanopure water.

Encapsulation of R6G Dye in Ag–Cu Nanoshells

Encapsulation of R6G inside the Ag–Cu nanoshells was carried out as follows. In a typical experiment, 200 µL of 1×10^{-3} M R6G was added into 40 mL of the aqueous solution of the nanoshells. After mixing under magnetic stirring for 4 h, 20 mL of toluene with 200 µL of 1-dodecanethiol was added to the above nanoshell solution, and the mixture was under magnetic stirring for 2 h. Then, 200 µL of HOAc was added into the solution. After stirring for another 15 min, the solution was left standing for 30 min, and the blue nanoshells were found at the water/organic interface. The nanoshells were then collected and purified with ethanol until the supernatant was colorless, which indicated the complete removal of free R6G molecules (and excess C12SH). The resulting C12SH-capped nanoshells were referred to as Ag–CuC12 (note that a small number of cysteine ligands remained on the nanoshell surface, as manifested in FTIR measurements, not shown).

Catalytic Reduction of 4-Nitroaniline by Ag–Cu Nanoshells

The experiment was carried out at room temperature (20 °C). Typically, 0.16 mg of the as-prepared cysteine-capped Ag–Cu nanoshells was dispersed in 14 mL of Nanopure water, along with 0.01 mmol of 4-nitroaniline. The color of the solution was found to change from bright blue to green-blue. 0.1 mmol of $NaBH_4$ dissolved in 200 µL of ice-cold water was then added as a reducing agent to the solution at room temperature. The UV–vis spectra of the solution were recorded at selected time intervals. At the end of the reduction reaction, the green-blue solution became bright blue again, signifying the full conversion of yellow 4-nitroaniline to colorless 4-phenylenediamine. To test the recyclability of the Ag–Cu nanoshells, the samples were collected by centrifugation at 6000 rpm for 15 min at the end of the experiment and used for repeat measurements under the otherwise identical conditions for a total of four cycles. Control experiments were carried out with solid Ag–Cu nanoparticles (also 0.16 mg) by using the same experimental procedure.

Structural Characterizations

The morphology and size of the metal nanostructures were characterized by TEM (Philips CM200 at 200 kV) studies. At least 200 nanoshells were analyzed to obtain a size distribution. XRD patterns were acquired with a Rigaku Americas Miniflex Plus diffractometer using Cu Kα radiation ($\lambda = 1.5418$ Å) within the range of $2\theta = 10$ to 80° at a scan rate of 2° min^{-1} with a 0.01° step size. UV–vis absorption spectra were collected with a Perkin-Elmer Lambda 35 spectrometer using a 1 cm quartz cuvette. Photoluminescence spectra were acquired with a PTI fluorescence spectrophotometer with a 450 W Xe lamp (Fluorolog, Jovin Yvon) and a close-cycle He cryostat (HC-2, APD Cryogenics). XPS spectra were recorded with a PHI 5400/XPS instrument equipped with an Al Kα source operated at 350 W and 10^{-9} Torr.

8.3 Results and Discussion

Stable Ag–Cu nanoshells were readily prepared by $NaBH_4$ coreduction of $AgNO_3$ and $Cu(NO_3)_2$ at the Ag:Cu initial feed ratio of 3:1 in the presence of NaSCN, with cysteine being the capping ligands. The structures were first examined by transmission electron microscopic (TEM) measurements. From Figure 8.1(A)–(C), one can see that indeed hollow nanoshells were successfully produced, with a mostly spherical shape. From the high-resolution TEM image in panel (D), the shells can be seen to exhibit well-defined lattice fringes, where the interplanar spacing of 0.237 nm is consistent with that of fcc Ag(111) crystalline planes (PDF card 65-2871), whereas the 0.253 nm spacing is in agreement with that of CuO(002) (PDF card 44-0706).[15-17] Interestingly, no lattice fringes were identified for metallic copper, indicating ready oxidation of copper into CuO in ambient. In addition, one can see that Ag and CuO formed segregated nanocrystalline domains rather than a homogeneous alloy, most likely because of their large lattice mismatch.[18-20] Statistical analysis based on more than 200 nanoshells showed that the outer diameter was averaged to be 57.2 ± 11.9 nm, with a shell thickness of 7.9 ± 1.6 nm, as manifested in the size histograms in panels (E) and (F), respectively, from which the hollow volume ratio was estimated to be ≈62% (v/v%).

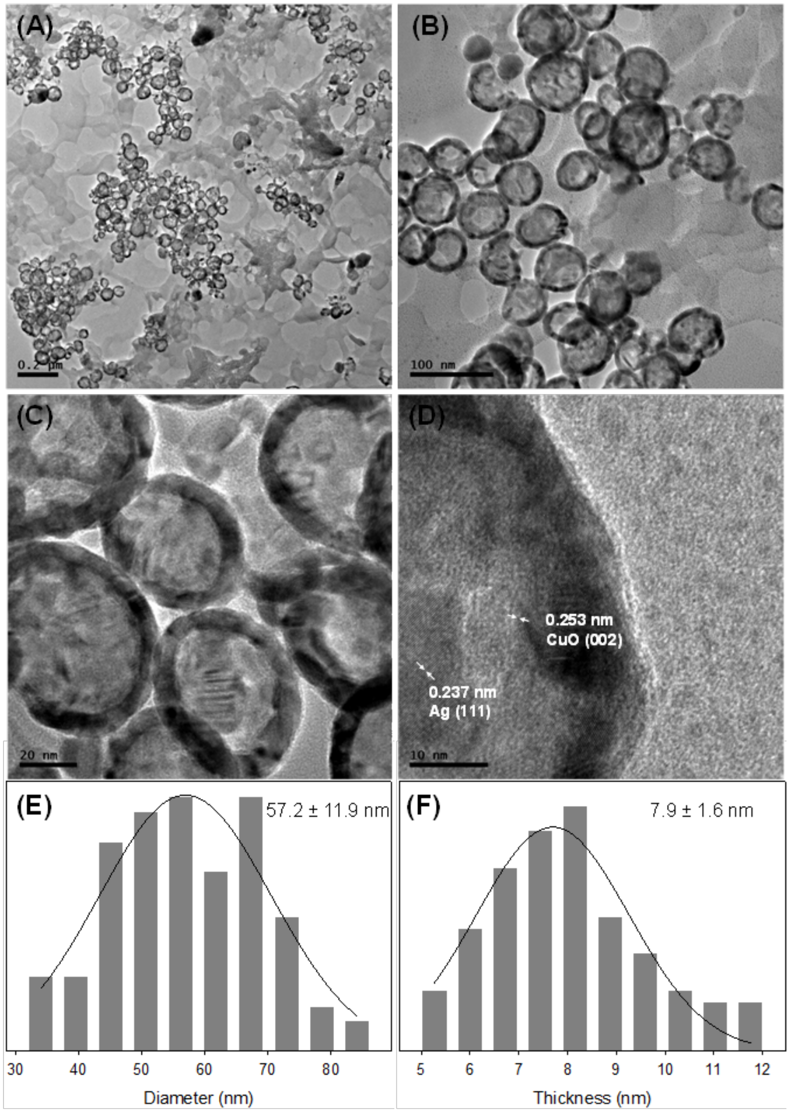

Figure 8.1 Representative TEM images of Ag–Cu nanoshells, where the scale bars are A) 200 nm, B) 100 nm, C) 20 nm, and D) 10 nm. The corresponding histograms of the nanoshell outer diameter and shell thickness are depicted in panels (E) and (F), respectively.

The structures of the nanocomposites were then examined by X-ray diffraction (XRD) measurements (Figure 8.2). Four major diffraction peaks can be identified at 2θ = 38.2°, 44.0°, 64.6°, and 77.2°, where the last three peaks might be ascribed to the diffraction of Ag (220), Ag (220), and Ag (311) crystalline planes, respectively, and the first peak likely arose from both Ag (111) and CuO (111). No other diffraction features were observed from CuO, possibly because of small crystallites or low crystallinity of CuO. Nonetheless, the XRD results suggest the formation of separate silver and copper phases, rather than an alloy structure, in the nanoshells. This is consistent with the results from TEM measurements (Figure 8.1(D)).

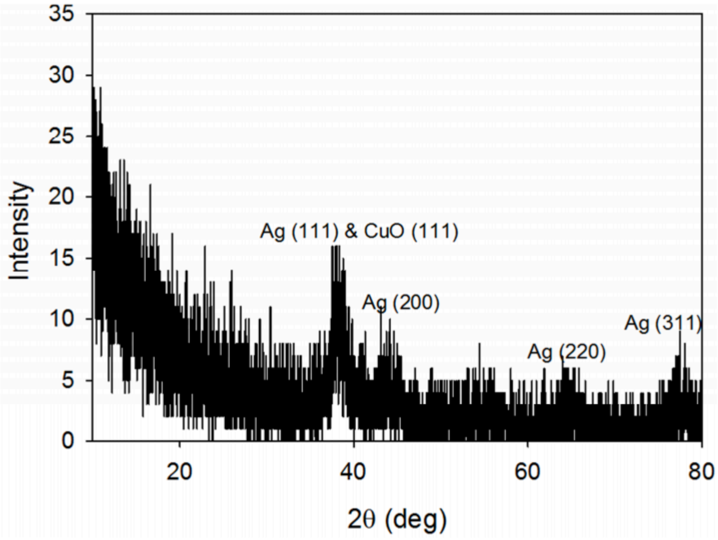

Figure 8.2 XRD patterns of Ag-Cu nanoshells.

Similar hollow structures were observed with monometallic Ag nanoshells that were prepared in the same manner (Figure 8.3), whereas without the addition of NaSCN, only solid Ag–Cu nanoparticles (Figure 8.4) were obtained, which were markedly smaller with an average diameter of 3.79 ± 2.31 nm. Notably, the Ag nanoshells were found to be rather defective, as compared to the almost continuous shell structures observed with Ag–Cu nanoshells (Figure 8.1). This disparity may be accounted for by the formation mechanism of hollow nanostructures based on nanoscale Kirkendall effect, where the outward diffusion of inner ions and inward diffusion of reducing agent or the electrons injected by the reducing agent are known to play a significant role in determining the eventual structure.[21] In the synthesis of monometallic Ag nanoshells, the diffusion and nucleation of silver ions are too fast to form a complete shell.[22] However, with the addition of copper ions, the formation of continuous shells might be facilitated by the slower reduction and nucleation kinetics of copper, because of the more negative reduction potential. Consequently, reduction and subsequent nucleation of Cu likely occurred within the gaps between the silver crystalline domains. In such a reaction mechanism, formation of an Ag structural scaffold is a critical first step. Experimentally, it was found that when the Ag:Cu feed ratio was changed to 1:1, the structures of the eventual nanoshells were actually very close to the one prepared above at 3:1; whereas at a lower feed ratio of 1:3, no nanoshells were formed. This suggests that the Ag:Cu feed ratio of 3:1 was optimal in the formation of stable nanoshell structures.

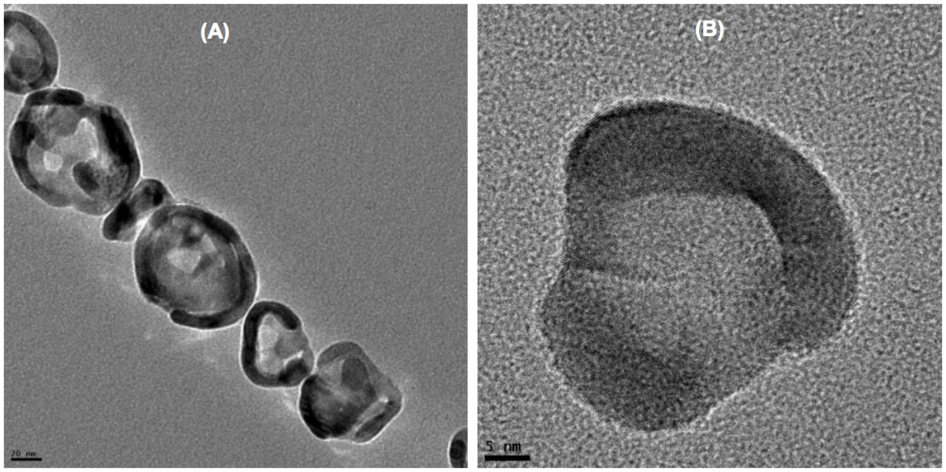

Figure 8.3 Representative TEM images of silver nanoshells. Scale bars are 20 nm in (A) and 5 nm in (B).

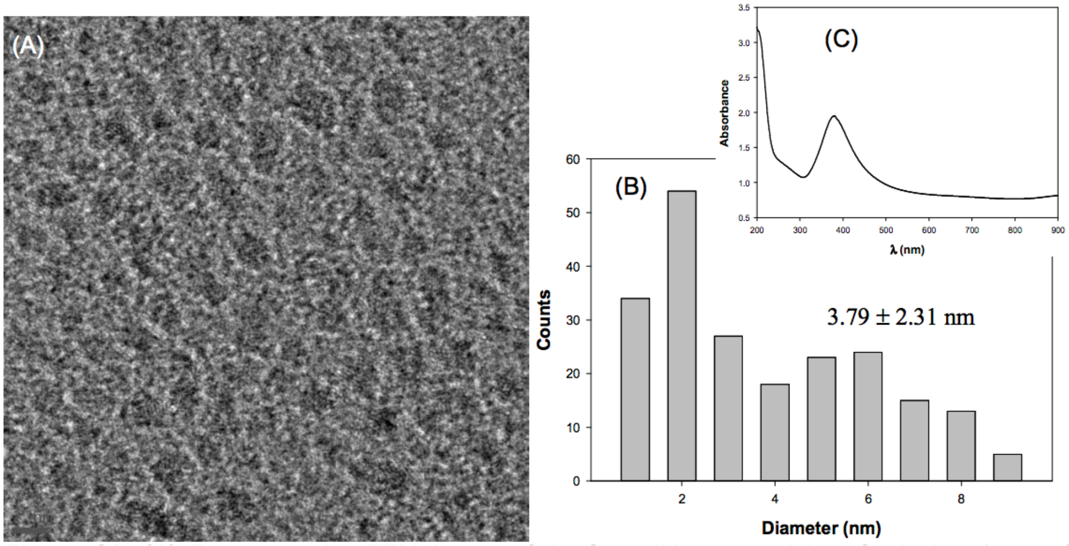

Figure 8.4 (A) Representative TEM image of Ag-Cu solid nanoparticles. Scale bar 2 nm. (B) The corresponding core size histogram, and (C) the UV-vis absorption spectrum in water.

Further structural insights were obtained in X-ray photoelectron spectroscopic (XPS) measurements where the elemental compositions of the nanoshells were quantified. From the survey spectrum of the Ag–Cu nanoshells (Figure 8.5(A)), the Ag 3d and Cu 2p electrons can be readily identified at around 370 and 940 eV, respectively (along with S 2p at 163 eV and C 1s at 283 eV). The high-resolution scans of the Ag 3d and Cu 2p electrons are depicted in Figure 8.5 (B, C). In panel (B), a doublet can be identified at 368.2 and 374.2 eV, consistent with the binding energies of the $3d_{5/2}$ and $3d_{3/2}$ electrons of metallic silver (identical to those of monometallic Ag nanoshells, Figure 8.6),[23,24] whereas the doublet at 934.2 and 954.2 eV in panel (C) may be assigned to the $2p_{3/2}$ and $2p_{1/2}$ electrons of Cu(II),[25,26] and the two satellite peaks at higher binding energies (943.2 and 963.4 eV) suggest the formation of CuO.[27] This is in good agreement with the results from TEM measurements (Figure 8.1). In addition, based on the integrated peak areas, the Ag:Cu atomic ratio was calculated to be 3.02:1, almost identical to the molar feed ratio of the starting materials.

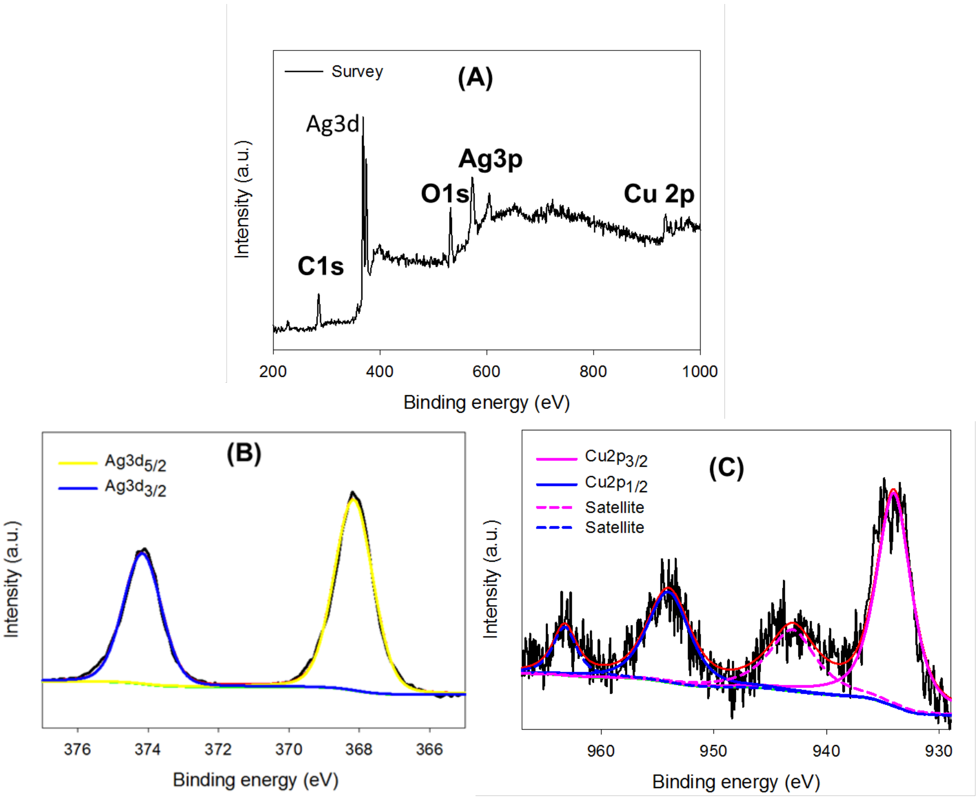

Figure 8.5 XPS survey (A) and high-resolution XPS spectra of the (B) Ag 3d and (C) Cu 2p electrons in Ag–CuC12 nanoshells. Black curves are experimental data and colored curves are deconvolution fits.

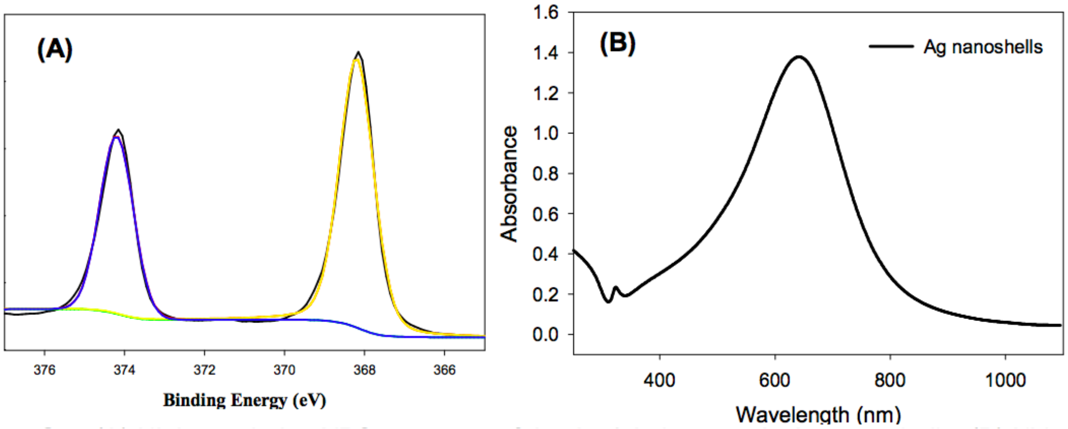

Figure 8.6 (A) High-resolution XPS spectrum of the Ag 3d electrons in Ag nanoshells. (B) UV-vis absorption spectrum of the Ag nanoshells in water.

The optical properties of the Au–Cu nanoshells were then studied. From Figure 8.7(A), it can be seen that the as-prepared Ag–Cu nanoshells exhibited a bright-blue color, with a well-defined absorption peak at 660 nm (red curve, Figure 8.7(B)). This can be assigned to the dipolar plasmon resonance of the Ag–Cu nanoshells, [28] in contrast to that of solid Ag–Cu nanoparticles (380 nm, Figure 8.4(C) or monometallic Ag nanoshells (635 nm, Figure 8.6(B)).[15] Moreover, a small sharp peak (marked by an asterisk) at 325 nm can be observed, which is corresponding to the antisymmetric plasmon mode of the nanostructures. Overall, the UV–vis absorption characteristics are in agreement with those of hollow metal nanostructures.[10]

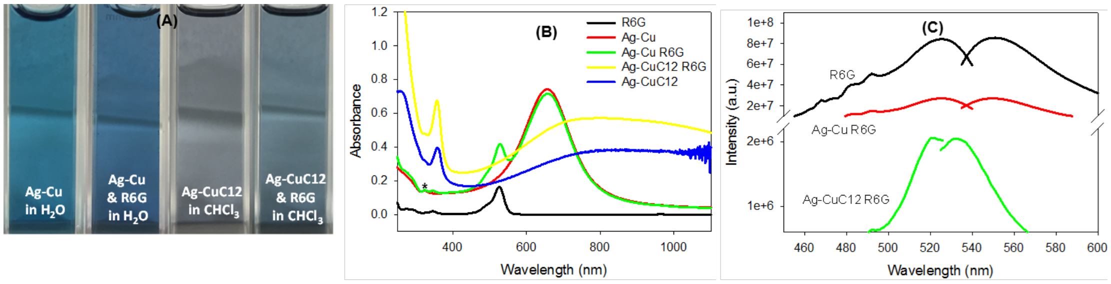

Figure 8.7 (A) Photographs of Ag–Cu nanoshells in water, mixture of Ag–Cu nanoshells and R6G in water, Ag–CuC12 nanoshells in chloroform, and R6G encapsulated in Ag–CuC12 nanoshells in chloroform. (B) UV–vis spectra of R6G in water (black curve), Ag–Cu nanoshells in water (red curve), mixture of R6G and Ag–Cu nanoshells in water (green curve), R6G encapsulated in Ag–CuC12 nanoshells in chloroform (yellow curve), and Ag–CuC12 in chloroform (blue curve). (C) Photoluminescence spectra of R6G in water (black curve), Ag–Cu and R6G mixture in water (red curve), and R6G encapsulated in Ag–CuC12 nanoshells in chloroform (green curve).

To demonstrate the feasibility of the nanoshells as effective phase-transfer reagents, R6G dye was used as the illustrating probe (Figure 8.7). When a calculated amount of R6G was added into the aqueous solution of Ag–Cu nanoshells, in addition to the peak at 660 nm, a new prominent absorption band emerged at 525 nm, along with a shoulder at 499 nm (green curve, Figure 8.7 (B)), which arose from the monomerization and dimerization of R6G molecules in aqueous solution, respectively.[29] Due to the combined contributions of R6G (pink) and Ag–Cu nanoshells (blue), the solution color became somewhat darker in blue (Figure 8.7(A)). The addition of a toluene solution containing 1-dodecanethiol (C12SH) into the above water solution led to surface functionalization of the nanoshells by the hydrophobic C12SH ligands (Ag–CuC12) through ligand-exchange reactions, and the nanoshells now became dispersible in $CHCl_3$ with a greenish blue color, bringing along R6G molecules trapped within the nanoshells to the organic phase (Figure 8.7(A)). The corresponding UV–vis absorption profile (yellow curve, Figure 8.7 (B)) showed significant broadening of the dipolar surface plasmon resonance peak which red-shifted substantially to 700–900 nm (a red-shift to 360 nm was also observed with the antisymmetric plasmon resonance peak). This may be due to the higher refractive index of $CHCl_3$ (1.446) than that of water (1.333).[14,30,31] Note that without the loading of R6G, the Ag–CuC12 nanoshells in $CHCl_3$ showed a much lighter (bluish gray) color (Figure 8.7(A), although the UV–vis absorption spectrum (blue cure, Figure 8.7(B)) looked similar.

The encapsulation of R6G into the Ag–Cu nanoshells was manifested in photoluminescence measurements. Figure 8.7(C) depicts the excitation and emission spectra of R6G in water, R6G mixed with Ag–Cu nanoshells in water, and R6G encapsulated in Ag–CuC12 nanoshells in $CHCl_3$. For the R6G solution in water (black curves), the excitation and emission peaks can be identified at 525 and 549 nm, respectively (R6G was also marginally soluble in $CHCl_3$ and exhibited almost identical peak positions).[14] Consistent photoluminescence characteristics were observed when R6G was added into the Ag–Cu nanoshells solution in water (red curves). Interestingly, when the Ag–Cu nanoshells were functionalized with C12SH and dispersed in $CHCl_3$, an apparent, though weaker, emission peak appeared at 532 nm at the excitation of 520 nm (green curves), suggesting that indeed R6G was entrapped within the Ag–Cu nanoshells, despite the absence of the characteristic absorption peaks of R6G at 525 and 499 nm in the UV–vis measurements (yellow curve, Figure 8.7(B)), most probably because of the low concentration of the nanoshells which contained only a small amount of R6G. The apparent disparity of the excitation and emission peak positions, as compared to those of free R6G and R6G mixed with Ag–Cu nanoshells in water, might be ascribed to the different chemical environments surrounding the R6G molecules.[32]

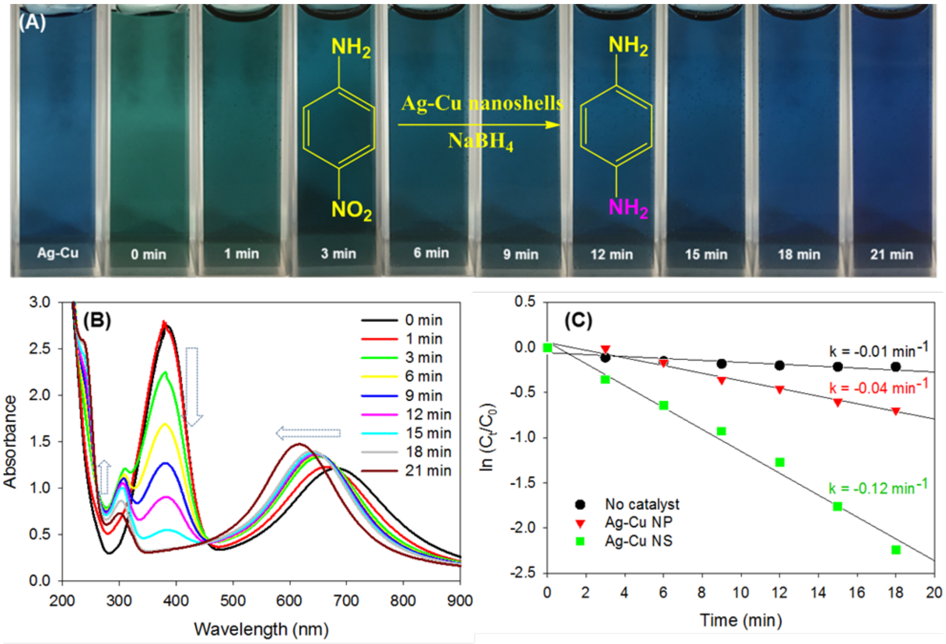

Figure 8.8 (A) Photographs at different time intervals during the reduction of 4-nitroaniline by $NaBH_4$ using Ag–Cu nanoshells as the catalyst. (B) UV–vis spectra of 4-nitroaniline reduced by $NaBH_4$ with Ag–Cu nanoshells as the catalyst at different reaction times (specified in figure legends), and (C) the corresponding plots of $\ln(C_t/C_0)$ versus time, with no catalyst (black circles), Ag–Cu solid nanoparticles (red triangles), and Ag–Cu hollow nanoshells (green squares).

Table 8.1 Catalytic activity of metal-based catalysts for reduction of 4-nitroaniline (4-NA) by borohydride.

Catalysts	4-NA: BH_4^- (mole ratio)	Catalyst (mg/mol 4-NA)	Activity (Sec^{-1})	Reaction time	References
Au−Cu nanocubes on glass slides	1:75	N/A		27min	33
$Fe_3O_4/SiO_2/Ag$	1:10	1.08e5		200s	34
AuNPs	1:10	650	2.5e-3		35
AuCu@G-rGO	1:50	392 (Au)		15min (90%)	36
AgCu@G-rGO	1:50	540 (Ag)		15 min (89%)	36
Ag-Cu nanoshells	1:10	14	2.0e-3	21min	This study

Furthermore, the cysteine-capped Ag–Cu nanoshells prepared above exhibited apparent catalytic activity toward the reduction of (yellow) 4-nitroaniline to (colorless) 4-phenylenediamine by $NaBH_4$ in water. 4-Phenylenediamine is an important component in engineering polymers, composites, hair dyes, and rubber antioxidant; and reduction of 4-nitroaniline to produce 4-phenylenediamine is a commonly used route.[33] Because of the marked color difference between the reactant and the product, the dynamics of this reduction reaction may be readily monitored by UV–vis absorption measurements. From Figure 8.8(A), one can see that prior to chemical reduction (t = 0 min), the solution containing 4-nitroaniline and Ag–Cu nanoshells exhibited a dark green color, due to the combination of blue Ag–Cu nanoshells and yellow 4-nitroaniline, and with prolonging reaction time, the solution color gradually changed to blue and eventually resembled that of the Ag–Cu nanoshell solution alone, due to the reduction of 4-nitroaniline into colorless 4-phenylenediamine. Such an apparent colorimetric evolution can also be manifested in UV–vis measurements. From Figure 8.8(B), one can see that at t = 0 min, the solution exhibited a well-defined absorption band at 380 nm due to the intermolecular charge transfer of 4-nitroaniline.[9] At prolonging reaction times, the peak absorbance gradually decreased, and vanished altogether after 21 min; concurrently, two new absorption bands emerged at 235 and 300 nm, which exhibited a continuous increase of the peak intensities with reaction time, consistent with the effective reduction of 4-nitroaniline to 4-phenylenediamine.[9,33-36] By contrast, with only $NaBH_4$ or with $NaBH_4$ and Ag–Cu solid nanoparticles, the reaction efficiency was markedly lower. For instance, after 21 min of reaction, only 10% of 4-nitroaniline was reduced with $NaBH_4$ alone, and 55% with $NaBH_4$ and Ag–Cu solid nanoparticles (Figure 8.9), but for Ag–Cu nanoshells, 100% reduction of 4-nitroaniline was achieved. In fact, in comparison with results reported in recent literature with metal-based catalysts for 4-nitroaniline reduction (Table 8.1), the performance of the Ag–Cu nanoshells is highly comparable, and in some cases even better, despite the use of a less amount of catalysts and a lower mole ratio of BH^{-}_{4} to 4-nitroaniline in the present study.

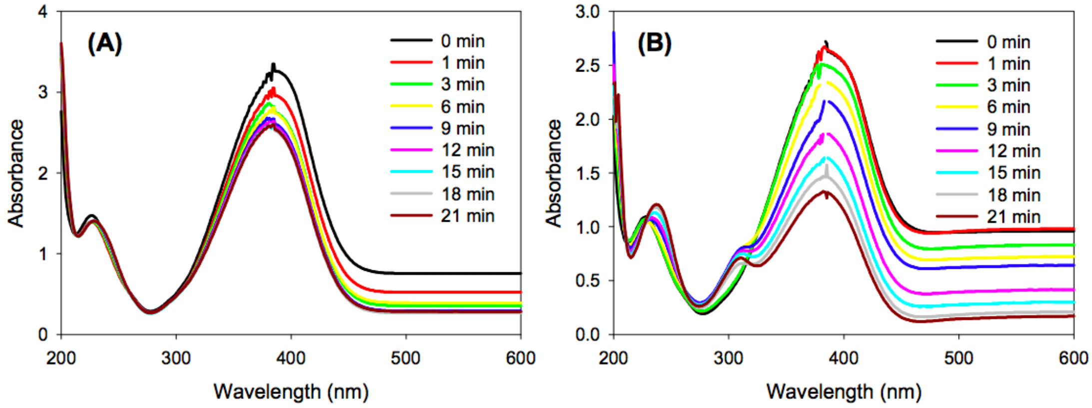

Figure 8.9 UV-vis spectra of the reduction of 4-nitroaniline by (A) $NaBH_4$ alone and (B) $NaBH_4$ + Ag-Cu solid nanoparticles. Experimental conditions are the same as those in Figure 8.8. The peak at 230 nm most likely arose from the π−π* transition of the phenyl ring electrons. Because of the low catalytic activity of Ag-Cu nanoparticles, this peak only exhibited a small variation with time. However this peak was not observed in Figure 8.8(B), likely because of being overshadowed by the steep absorption profile of the Ag-Cu nanoshells in the UV region (note that Ag-Cu nanoshells are much larger than the solid nanoparticles).

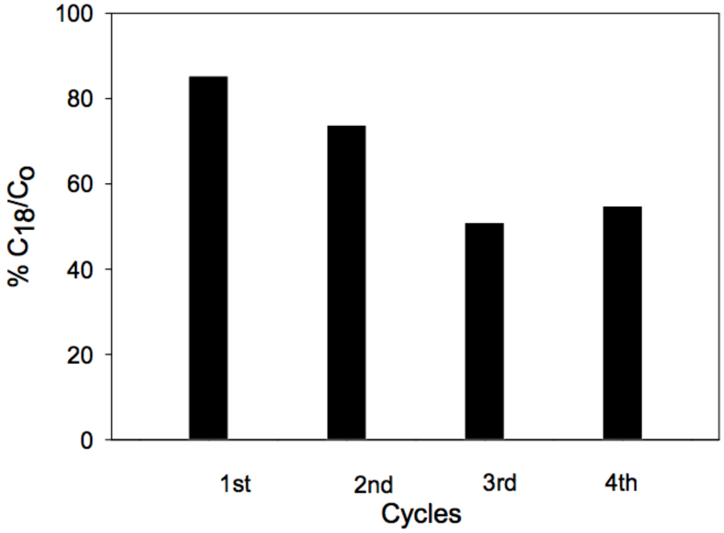

Figure 8.10 Conversion of 4-nitroanaline to 4-phenylenediamine after 18 min reduction (C_{18}/C_0) in the first, second, third and fourth cycle catalyzed by the same Ag-Cu nanoshells.

Furthermore, one may notice a drastic blue-shift of the dipolar plasmon resonance of the Ag–Cu nanoshells during the reaction process (from 665 nm at $t = 0$ min to 615 nm at $t = 21$ min), along with an apparent increase of the peak absorbance and narrowing of the absorption band, most likely due to the injection of electrons by the reducing borohydride radicals in the solution.[37,38] Such electron accumulation on the nanoshell surface is critical for the catalytic reduction of 4-nitroaniline in the solution. This was manifested in the reaction kinetics which was analyzed by the variation of the peak absorbance at 380 nm with time. Figure 8.8 (C) depicts the $\ln(C_t/C_0)$ versus time plot (green squares), where C_0 and C_t refer to the concentration (peak absorbance at 380 nm) of 4-nitroaniline at $t = 0$ and different reaction times, respectively. The good linearity suggests first-order reaction kinetics, and from the slope, the rate constant (k^{-1}) was estimated to 0.12 min^{-1}, about three times greater than that of Ag–Cu solid nanoparticles (0.04 min^{-1}, red triangles) and 12 times that of the reaction without any catalyst (0.01 min^{-1}, black circles).

The recycling of the Ag–Cu nanoshells for the catalytic reduction of 4-nitroaniline was also tested by collecting the nanoshells by centrifugation at 6000 rpm for 15 min at the end of the experiment and using the nanoshells for repeat measurements. The catalytic activity was evaluated and compared for three more times. From Figure 8.11, it can be seen that the reductive conversion of 4-nitroaniline to 4-phenylenediamine after 18 min of reaction was 85.4%, 73.9%, 51.0%, and 54.9% for the first, second, third, and fourth cycle, respectively. This indicates that the Ag–Cu nanoshells can be easily recycled and reused with a high catalytic activity.

From the results presented above, one can clearly see that the morphologies of metal nanocrystals played a critical role in the catalytic reduction of 4-nitroaniline, which entails three major steps:[34,39] (a) borohydride ions (BH_4^-) and nitro moieties chemically adsorb onto the metal surfaces; (b) hydrolysis of BH_4^- leads to effective electron transfer to the metal surface and further to the nitro groups;[40] such an electronic relay mechanism helps overcome the kinetic barrier, and significantly improve the reaction kinetics;[36] and (c) the reduction product 4-phenylenediamine desorbs from the metal surfaces. In the present study, the markedly higher reaction rate afforded by Ag–Cu nanoshells was likely due to the ready accessibility of both internal and external surfaces that facilitated the adsorption of reactant molecules and the accumulation of electrons injected from reducing reagents for the reduction of the nitro groups.

8.4 Conclusion

Stable Ag–Cu hollow nanoshells were prepared in aqueous solution by a facile one-pot process. The nanoscale cavity might be exploited for the encapsulation and phase transfer of target molecules, as illustrated by organic dye R6G as the molecular probe. The Ag–Cu nanoshells also exhibited enhanced catalytic activity toward the $NaBH_4$reduction of 4-nitroaniline, as compared to Ag–Cu solid nanoparticles, most likely due to ready accessibility of both inner and outer surfaces of the nanoshells that facilitated adsorption and mass transport of the reactant and product molecules and interfacial electron-transfer dynamics.

8.5 References

(1) Cui, C. H.; Yu, S. H. Engineering Interface and Surface of Noble Metal Nanoparticle Nanotubes toward Enhanced Catalytic Activity for Fuel Cell Applications. *Accounts Chem Res* **2013**, *46*, 1427-1437.

(2) Tan, X. H.; Jin, R. C. Ultrasmall metal nanoclusters for bio-related applications. *Wires Nanomed Nanobi* **2013**, *5*, 569-581.

(3) Sung, H. K.; Oh, S. Y.; Park, C.; Kim, Y. Colorimetric Detection of Co2+ Ion Using Silver Nanoparticles with Spherical, Plate, and Rod Shapes. *Langmuir* **2013**, *29*, 8978-8982.

(4) Li, C. H.; Jamison, A. C.; Rittikulsittichai, S.; Lee, T. C.; Lee, T. R. In Situ Growth of Hollow Gold-Silver Nanoshells within Porous Silica Offers Tunable Plasmonic Extinctions and Enhanced Colloidal Stability. *Acs Appl Mater Inter* **2014**, *6*, 19943-19950.

(5) Mudshinge, S. R.; Deore, A. B.; Patil, S.; Bhalgat, C. M. Nanoparticles: Emerging carriers for drug delivery. *Saudi Pharm J* **2011**, *19*, 129-141.

(6) Kim, M. R.; Kim, J. Y.; Kim, S. J.; Jang, D. J. Laser-induced fabrication of platinum nanoshells having enhanced catalytic and Raman properties. *Appl Catal a-Gen* **2011**, *393*, 317-322.

(7) Wu, H. X.; Wang, P.; He, H. L.; Jin, Y. D. Controlled synthesis of porous Ag/Au bimetallic hollow nanoshells with tunable plasmonic and catalytic properties. *Nano Res* **2012**, *5*, 135-144.

(8) Zeng, J.; Zhang, Q.; Chen, J.; Xia, Y. A comparison study of the catalytic properties of Au-based nanocages, nanoboxes, and nanoparticles. *Nano letters* **2010**, *10*, 30-35.

(9) Wu, W. M.; Liang, S. J.; Chen, Y.; Shen, L. J.; Zheng, H. R.; Wu, L. High efficient photocatalytic reduction of 4-nitroaniline to p-phenylenediamine over microcrystalline SrBi2Nb2O9. *Catal Commun* **2012**, *17*, 39-42.

(10) Kado, S.; Yokomine, S.; Kimura, K. One-pot synthesis of silver nanoshells with near-infrared extinction by a thiocyanate-assisted approach. *Rsc Adv* **2014**, *4*, 10830-10833.

(11) Xie, S. F.; Jin, M. S.; Tao, J.; Wang, Y. C.; Xie, Z. X.; Zhu, Y. M.; Xia, Y. N. Synthesis and Characterization of Pd@MxCu1-x (M=Au, Pd, and Pt) Nanocages with Porous Walls and a Yolk-Shell Structure through Galvanic Replacement Reactions. *Chem-Eur J* **2012**, *18*, 14974-14980.

(12) Dong, F.; Guo, W.; Park, S. K.; Ha, C. S. Controlled synthesis of novel cyanopropyl polysilsesquioxane hollow spheres loaded with highly dispersed Au nanoparticles for catalytic applications. *Chem Commun* **2012**, *48*, 1108-1110.

(13) Choi, Y.; Hong, S.; Liu, L.; Kim, S. K.; Park, S. Galvanically Replaced Hollow Au-Ag Nanospheres: Study of Their Surface Plasmon Resonance. *Langmuir* **2012**, *28*, 6670-6676.

(14) Zehentbauer, F. M.; Moretto, C.; Stephen, R.; Thevar, T.; Gilchrist, J. R.; Pokrajac, D.; Richard, K. L.; Kiefer, J. Fluorescence spectroscopy of Rhodamine 6G: Concentration and solvent effects. *Spectrochim Acta A* **2014**, *121*, 147-151.

(15) Jiang, H. J.; Moon, K. S.; Wong, C. P. Synthesis of Ag-Cu alloy nanoparticles for lead-free interconnect materials. *2005 10th International Symposium on Advanced Packaging Materials: Processes, Properties and Interfaces* **2005**, 173-177.

(16) Hu, P. G.; Song, Y.; Chen, L. M.; Chen, S. W. Electrocatalytic activity of alkyne-functionalized AgAu alloy nanoparticles for oxygen reduction in alkaline media. *Nanoscale* **2015**, *7*, 9627-9636.

(17) Gao, D. Q.; Zhang, J.; Zhu, J. Y.; Qi, J.; Zhang, Z. H.; Sui, W. B.; Shi, H. G.; Xue, D. S. Vacancy-Mediated Magnetism in Pure Copper Oxide Nanoparticles. *Nanoscale Res Lett* **2010**, *5*, 769-772.

(18) Huttunen, P. A.; Makinen, J.; Vehanen, A. Defects in Heteroepitaxial Structures Studied with Monoenergetic Positrons - Large-Lattice-Mismatch Systems Cu/Ag(111) and Ag/Cu(111). *Phys Rev B* **1990**, *41*, 8062-8074.

(19) Tsuji, M.; Hikino, S.; Tanabe, R.; Matsunaga, M.; Sano, Y. Syntheses of Ag/Cu alloy and Ag/Cu alloy core Cu shell nanoparticles using a polyol method. *Crystengcomm* **2010**, *12*, 3900-3908.

(20) Tan, K. S.; Cheong, K. Y. Advances of Ag, Cu, and Ag-Cu alloy nanoparticles synthesized via chemical reduction route. *J Nanopart Res* **2013**, *15*.

(21) Ben Moshe, A.; Markovich, G. Synthesis of Single Crystal Hollow Silver Nanoparticles in a Fast Reaction-Diffusion Process. *Chem Mater* **2011**, *23*, 1239-1245.

(22) Wang, W. S.; Dahl, M.; Yin, Y. D. Hollow Nanocrystals through the Nanoscale Kirkendall Effect. *Chem Mater* **2013**, *25*, 1179-1189.

(23) Dai, S. X.; Zhang, X. T.; Li, T. F.; Du, Z. L.; Dang, H. X. Preparation of silver nanopatterns on DNA templates. *Appl Surf Sci* **2005**, *249*, 346-353.

(24) Mansikkamaki, K.; Haapanen, U.; Johans, C.; Kontturi, K.; Valden, M. Adsorption of benzotriazole on the surface of copper alloys studied by SECM and XPS. *J Electrochem Soc* **2006**, *153*, B311-B318.

(25) Lee, S. W.; Lee, Y. S.; Heo, J.; Siah, S. C.; Chua, D.; Brandt, R. E.; Kim, S. B.; Mailoa, J. P.; Buonassisi, T.; Gordon, R. G. Improved Cu2O-Based Solar Cells Using Atomic Layer Deposition to Control the Cu Oxidation State at the p-n Junction. *Adv Energy Mater* **2014**, *4*.

(26) Knight, J. M.; Wells, R. K.; Badyal, J. P. S. Plasma Oxidation of Copper Silver Alloy Surfaces. *Chem Mater* **1992**, *4*, 640-641.

(27) Hsu, Y. K.; Yu, C. H.; Chen, Y. C.; Lin, Y. G. Hierarchical Cu_2O photocathodes with nano/microspheres for solar hydrogen generation. *Rsc Adv* **2012**, *2*, 12455-12459.

(28) Tuersun, P.; Han, X. E. Optical absorption analysis and optimization of gold nanoshells. *Appl Optics* **2013**, *52*, 1325-1329.

(29) Rao, A. P.; Rao, A. V. Luminiscent dye Rhodamine 6G doped monolithic and transparent TEOS silica xerogels and spectral properties. *Sci Technol Adv Mat* **2003**, *4*, 121-129.

(30) Hu, Y.; Fleming, R. C.; Drezek, R. A. Optical properties of gold-silica-gold multilayer nanoshells. *Opt Express* **2008**, *16*, 19579-19591.

(31) Rasch, M. R.; Sokolov, K. V.; Korgel, B. A. Limitations on the Optical Tunability of Small Diameter Gold Nanoshells. *Langmuir* **2009**, *25*, 11777-11785.

(32) Trenkmann, I.; Bok, S.; Korampally, V. R.; Gangopadhyay, S.; Graaf, H.; von Borczyskowski, C. Counting single Rhodamine 6G dye molecules in organosilicate nanoparticles. *Chem Phys* **2012**, *406*, 41-46.

(33) Abbas, M.; Torati, S. R.; Kim, C. A novel approach for the synthesis of ultrathin silica-coated iron oxide nanocubes decorated with silver nanodots (Fe3O4/SiO2/Ag) and their superior catalytic reduction of 4-nitroaniline. *Nanoscale* **2015**, *7*, 12192-12204.

(34) Zhou, Q.; Qian, G. Z.; Li, Y.; Zhao, G.; Chao, Y. W.; Zheng, J. W. Two-dimensional assembly of silver nanoparticles for catalytic reduction of 4-nitroaniline. *Thin Solid Films* **2008**, *516*, 953-956.

(35) Sharma, K.; Bhalla, V.; Kumar, M. Facile synthesis of gold nanoparticles using aggregates of pentacenequinone derivative and their catalytic activity for oxidative polymerization, homocoupling and reduction. *Rsc Adv* **2014**, *4*, 53795-53800.

(36) Rathore, P. S.; Patidar, R.; Shripathi, T.; Thakore, S. Magnetically separable core-shell iron oxide@nickel nanoparticles as high-performance recyclable catalysts for chemoselective reduction of nitroaromatics. *Catal Sci Technol* **2015**, *5*, 286-295.

(37) Ung, T.; Giersig, M.; Dunstan, D.; Mulvaney, P. Spectroelectrochemistry of colloidal silver. *Langmuir* **1997**, *13*, 1773-1782.

(38) Henglein, A.; Mulvaney, P.; Linnert, T. Chemistry of Agn Aggregates in Aqueous-Solution - Nonmetallic Oligomeric Clusters (N-Less-Than-10) and Metallic Particles (N-Greater-Than-10). *Abstr Pap Am Chem S* **1991**, *201*, 412-Inor.

(39) Herves, P.; Perez-Lorenzo, M.; Liz-Marzan, L. M.; Dzubiella, J.; Lu, Y.; Ballauff, M. Catalysis by metallic nanoparticles in aqueous solution: model reactions. *Chem Soc rev* **2012**, *41*, 5577-5587.

(40) Hsia, C. F.; Madasu, M.; Huang, M. H. Aqueous Phase Synthesis of Au-Cu Core-Shell Nanocubes and Octahedra with Tunable Sizes and Noncentrally Located Cores. *Chem Mater* **2016**, *28*, 3073-3079.